Politecnico di Torino

Master Degree in Aerospace Engineering
Department of Mechanical and Aerospace Engineering

Lifing assessment of Gas Turbine blade root affected by Out-of-Tolerances

Focus on the impact of machining out-of-tolerances by means of 2D finite element analyses

Supervisor:
Prof. Daniele BOTTO
External supervisor:
Ing. Andrea BESSONE

Candidate:
Federico MANZINI

March 2024

Ai miei nonni Ugo e Cisa,
le mie due stelle in cielo

Abstract

Climate changes of recent decades forced engineers and scientists to challenge themselves with new solutions and improving existing ones. In this scenario heavy-duty gas-turbines (GTs) development was focused on improving performances, e.g., augmenting power-output and efficiency, and employing them as a support to renewable energy sources (RES). Consequently, GTs components have to withstand always higher thermomechanical loads. Moreover, nowadays GTs are operated in cyclic conditions much more frequently than in the past. Turbine blades are surely one of the most critical components due to the harsh operating conditions. Hence, the production process of these components is a critical aspect to be considered in design and qualification phase. Nevertheless, machining process limitations must be considered and implemented to ensure a feasible compromise on production tolerances. Supplier qualification process has to be well implemented to guarantee high quality level products.

This work deals with out-of-tolerances recorded after machining process of a turbine blade fir-tree attachment during a new supplier qualification. The goal of this study is better handling the impact of out-of-tolerances and tolerance limits on components lifing by means of 2D finite element analyses (FEA). The selected gas turbine component for this work is a third stage rotor blade, designed for a F-class engine operation with a long-proven manufacturing experience. This situation permits the use of mean material properties during the component lifing

evaluation. The study workflow of this activity is reported as follows. First, a statistical analysis was carried out to choose the most representative parameters affected by out-of-tolerances. Then, a FE model of a nominal geometry was set, and a mesh refinement process has been carried out to achieve mesh-independent results. Secondly, the same FE mesh setting has been applied to geometries modified with out-of-tolerance parameters by a 2D parametric CAD model. The component life assessment has been performed by means of AEN LCF in-house tools, and then it was applied a stress-gradient approach to obtained results to keep into account notch effects.

A results comparison between LCF in-house tools and stress-gradient approach has been performed and reported for the blade. For sake of completeness, also the disc lifing has been evaluated by means of a dedicated LCF in-house tool, more specific for the disc material.

In conclusion, a detailed comparison between different out-of-tolerances parameters is reported and discussed.

Results showed that out-of-tolerances impact on component life can be considerable in some cases. These analyses have permitted to better understand the impact of these out-of-tolerances on components lifing and a final assessment on their employment is efficiently allowed. Moreover, future insights such as a 3D analysis con be performed starting from this work, to consider those effects that in a 2D study can’t be evaluated like planarity of the active planes.

Acknowledgments

Innanzitutto, ci tengo a ringraziare l’ing. Andrea Bessone e l’ing. Francesco Bagnera di Ansaldo Energia per tutto il supporto e la dedizione con cui mi hanno seguito nella stesura di questa tesi e più in generale tutto il team T&T per avermi messo a mio agio fin da subito. Inoltre, ringrazio il prof. Daniele Botto per l’interesse e la disponibilità nel seguirmi in questo lavoro di tesi. Grazie per avermi trasmesso la passione che avete per il vostro lavoro e per avermi aiutato ad inserirmi in una realtà, quella aziendale, per me nuova. Inoltre, vi ringrazio particolarmente per il trattamento che ho ricevuto come persona.

Un ringraziamento speciale va a mio papà, Bruno, e a mia mamma, Cinzia, per essermi sempre stati vicini e soprattutto avermi dato una famiglia unita e piena di affetto. Vi ringrazio per avermi messo nelle condizioni di poter dare il massimo sempre, facendo in modo che l’unica mia preoccupazione fosse lo studio. Quello che sono oggi come persona lo devo a voi, ai valori che mi avete insegnato e agli esempi che mi avete dato. Poi ci tengo a ringraziare mio fratello, Leonardo, con cui sono cresciuto e con cui ho condiviso tutto. Ci sei sempre stato per me, sono orgoglioso e fortunato ad avere un fratello così. Infine un grande grazie va ai miei nonni, Angela, Italo, Ugo e Cisa, per avermi cresciuto con tutto l’amore che solo i nonni sanno dare. I ricordi che ho di voi da bambino sono la cosa che costudisco più gelosamente. C’è tanto di ognuno di voi nel mio percorso e in questo traguardo.

Un ringraziamento va poi agli amici di sempre e a quelli che ho incontrato in questo percorso universitario, per aver reso le giornate e le sessioni un po’ più leggere con le risate e la compagnia.

Table of contents

Introduction.......1

Background and motivations.......1

Objective.......4

1. General gas turbines description.......8

1.1. Joule-Brayton thermodynamic cycle.......9

1.2. Gas turbines architecture.......10

1.3. Gas turbine stage description.......10

1.3.1. Vanes.......11

1.3.2. Blades.......12

1.4. Turbine cooling system.......13

1.5. Turbine vane and blade coating.......18

1.6. Turbine blade design workflow.......19

1.7. Turbine blades machining processes.......21

1.7.1. Creep feed grinding.......21

1.7.2. Electrical Discharge Machining.......25

2. Overview on materials fatigue.......30

2.1. Historical background.......31

2.2. Design approaches to fatigue.......36

2.2.1. Safe-life approach.......36

2.2.2. Fail-safe approach.......37

2.2.3. Damage tolerant approach.......38

2.3. Fatigue estimation approaches.......38

2.3.1. Stress-based approach.......39

2.3.2. Strain based approach.......41

3. Component description and CAD model.......45

4. Statistical analysis on out of tolerance (machining process).......49

5. Fatigue life assessment tools.......51

5.1. In-house tool for blade fir-tree attachment LCF assessment.......51

5.2. In-house tool for rotor disc LCF assessment.......52

5.3. Stress gradient approach 53

6. Tests matrix definition 56

7. Parameters modification 60
  7.1. Angles modification 60
  7.2. Offsets modifications 61
  7.3. Angles and offsets modification 61

8. FE model preparation 63
  8.1. Boundary conditions 65
    8.1.1. Lower cut section 65
    8.1.2. Upper cut section 65
    8.1.3. Lateral boundary conditions 66
  8.2. Contact setting 67

9. Mesh refinement process 72
  9.1. Stress comparison 75
    9.1.1. Blade fir-tree attachment results 75
    9.1.2. Disc groove results 76
  9.2. Contact pressure comparison 78
  9.3. LCF comparison 78
  9.4. Final mesh selection 82

10. Results 85
  10.1. Nominal geometry 85
    10.1.1. Displacements 85
    10.1.2. Radial stress and von Mises stress distribution 86
    10.1.3. Contact results 87
    10.1.4. LCF evaluation 88
  10.2. Out-of-tolerance on the active plane angle of the third lobe 89
    10.2.1. Radial and von Mises stress distribution 89
    10.2.2. Contact status and pressure 90
    10.2.3. LCF evaluation 91
  10.3. Out-of-tolerance on the active plane offset of the second lobe 92

10.3.1. Radial and von Mises stress distribution 92
10.3.2. Contact status and pressure 93
10.3.3. LCF evaluation 94
10.4. All parameters on maximum out-of-tolerance values 95
10.4.1. Radial and von Mises stress distribution 95
10.4.2. Contact status and pressure 96
10.4.3. LCF evaluation 97

11. Comparison with nominal geometry results 100

12. Conclusions 111

Appendix 114
A. Neuber's rule 114
B. Ramberg-Osgood model 117
C. Strain-based approaches to fatigue life 118
C.1. Material's cyclic curve 118
C.2. Coffin-Manson equation 119
C.3. Morrow approach to mean stress – mathematical steps 120
D. Shot peening 122
E. Case studies results comparisons 125

Bibliography 129

List of figures

Figure 0.1. Procedure workflow. 5

Figure 1.1. GT36, class H gas turbine produced by AEN [12]. 8

Figure 1.2. (**a**) Ideal Joule-Brayton cycle [13]; (**b**) Real Joule-Brayton cycle [13]. 9

Figure 1.3. Gas turbine scheme [14]....... 10

Figure 1.4. Example of Turbine vane illustration [15]. 11

Figure 1.5. Example of Turbine blade illustration [16]....... 12

Figure 1.6. Turbine cooling system [18]. 13

Figure 1.7. Example of TIT increasing thanks to new cooling technologies [19]. . 14

Figure 1.8. Film cooling [19]....... 15

Figure 1.9. Example of Jet impingement cooling [19]. 16

Figure 1.10. Example of Rib-turbulated cooling [19]....... 16

Figure 1.11. Example of Pin-Fin cooling [19]. 17

Figure 1.12. TIT evolution though the decades [20]. 18

Figure 1.13. Coatings scheme [22]. 19

Figure 1.14. Blades design process [5]. 20

Figure 1.15. Creep feed grinding [23]....... 22

Figure 1.16. Creep feed grinding of a blade root [24]....... 25

Figure 1.17. EDM scheme [25]....... 26

Figure 1.18. EDM discharge phases. [25]. 27

Figure 1.19. Example of Die-Sink EDM machining [27]. 28

Figure 2.1. S-N diagram divided into fatigue life regions. The graph is in the log-log scale [37]. 39

Figure 2.2. Comparison of S-N curves for 1045 steel alloy and 2024 aluminium alloy [38]. 40

Figure 2.3. Haigh diagram. The x-axis reports the mean stress, the y-axis reports the stress amplitude [37]....... 41

Figure 2.4. Coffin-Manson curve [31]....... 42

Figure 2.5. (**a**) illustration of cycle dependent relaxation [39]; (**b**) effect of mean stress in strain-number of cycle diagram [31]. 43

Figure 3.1. (**a**) 3D CAD model with the entire blade and its disc sector; (**b**) fir-tree and disc groove 3D sub-model; (**c**) details of the cutting plane; (**d**) cutted 3D portion; (**e**) 2D final CAD model. 46

Figure 3.2. (**a**) Blade fir-tree attachment definitions; (**b**) parameters considered in the analysis; (**c**) Disc groove definition; (**d**) Coupling between blade's attachment and disc groove. 47

Figure 4.1. (**a**) α2 measurements statistical distribution; (**b**) α3 measurements statistical distribution; (**c**) L1 measurements statistical distribution; (**d**) L2 measurements statistical distribution. 50

Figure 5.1. Example of a possible procedure for a generic blade fir-tree attachment LCF evaluation [31]. 52

Figure 5.2. Stabilized load cycle. 52

Figure 5.3. Tool for disc groove LCF assessment workflow. 53

Figure 5.4. Typical S-N curve obtained from experimental tests. 54

Figure 5.5. (**a**) LCF contours and stress gradient direction (black arrow); (**b**) stress gradient trend with respect to distance. 54

Figure 7.1. (**a**) Rotation of active planes for angles upper tolerance limit cases; (**b**) rotation of active planes for angles lower tolerance limit cases; (**c**) Rotation of active planes for angles out-of-tolerance cases. 60

Figure 7.2. (**a**) Translation of active planes for offsets upper tolerance and out-of-tolerance cases; (**b**) Translation of active planes for offsets lower tolerance limit cases. 61

Figure 7.3. (**a**) angles and offsets upper tolerance limit cases; (**b**) angles and offsets lower tolerance limit cases; (**c**) angles and offsets out-of-tolerance cases. 61

Figure 8.1. FE model from *ANSYS Workbench 19.2*. 63

Figure 8.2. Mesh elements [43]. (**a**) PLANE183; (**b**) CONTA172; (**c**) TARGE169. . 64

Figure 8.3. (**a**) Global cartesian coordinate system; (**b**) cyclindrical coordinate system. 65

Figure 8.4. Radial displacement at lower cut section from 3D FEA results. Contour values are normalized by maximum radial displacement. 65

Figure 8.5. Radial stress at upper cut section from 3D FEA results. Contour values are normalized by a reference value. (**a**) mechanical analysis; (**b**) thermomechanical analysis. 66

Figure 8.6. (**a**) mechanical boundary conditions; (**b**) body temperatures normalized by maximum temperature.......... 67

Figure 8.7. Effect of normal penalty stiffness factor on maximum contact pressure obtained with elastic calculation. Pressures are normalized by a reference value. 68

Figure 8.8. Effect of friction coefficient on von Mises maximum stress obtained with elastic-plastic calculation. Values of stress are normalized with material's yield stress. 69

Figure 8.9. *ANSYS Pair Based Contact Manager.* Image is taken from *ANSYS Mechanical APDL 19.2*.......... 69

Figure 8.10. *CONTA172* key-options. Image is taken from *ANSYS Mechanical APDL 19.2*. 70

Figure 9.1. Mesh size comparison. Contact size is (**a**) 0,5 mm; (**b**) 0,25 mm; (**c**) 0,2 mm; (**d**) 0,1 mm; (**e**) 0,06 mm; (**f**) 0,03 mm; (**g**) 0,02 mm; (**h**) 0,01 mm; (**i**) 0,005 mm. 73

Figure 9.2. (**a**) Radial stress contours; (**b**) von Mises stress contours; (**c**) contact pressure on lobe 1; (**d**) contact pressure on lobe 2; (**e**) contact pressure on lobe 3; (**f**) blade LCF contours; (**g**) disc LCF contours.......... 74

Figure 9.3. (**a**) maximum radial stress trend with respect to contact element size; (**b**) minimum radial stress trend with respect to contact element size; (**c**) maximum von Mises stress trend with respect to contact element size.......... 76

Figure 9.4. (**a**) maximum radial stress trend with respect to contact element size; (**b**) minimum radial stress trend with respect to contact element size; (**c**) maximum von Mises stress trend with respect to contact element size.......... 77

Figure 9.5. Contact pressure trend with respect to contact element size.......... 78

Figure 9.6. Blade root LCF critical region comparison. (**a**) 70k mesh; (**b**) 270k mesh; (**c**) 43k mesh;(**d**) 79k mesh; (**e**) 125k mesh; (**f**) 240k mesh; (**g**) 355k mesh; (**h**) 693k mesh; (**i**) 1350k mesh.......... 79

Figure 9.7. Disc groove LCF critical region comparison. (**a**) 70k mesh; (**b**) 270k mesh; (**c**) 43k mesh;(**d**) 79k mesh; (**e**) 125k mesh; (**f**) 240k mesh; (**g**) 355k mesh; (**h**) 693k mesh; (**i**) 1350k mesh. 80

Figure 9.8. (**a**) Effect of contact mesh size on blade attachment number of cycles; (**b**) effect of contact mesh size on disc groove number of cycles. 81

Figure 9.9. Comparison between maximum radial stress (green SMX) and maximum radial stress predicted by *ANSYS* (red SMXB). 82

Figure 9.10. Chosen mesh for the analysis. 83

Figure 10.1. (**a**) Radial displacements contours; (**b**) circumferential displacement contours. Values are normalized by a reference one. 85

Figure 10.2. (**a**) blade root radial stress contours; (**b**) blade root von Mises stress contours; (**c**) disc groove radial stress contours; (**d**) disc groove von Mises stress contours. 86

Figure 10.3. (**a**) contact status; (**b**) contact pressure on lobe 1; (**c**) contact pressure on lobe 2; (**d**) contact pressure on lobe 3. 87

Figure 10.4. (**a**) blade fir-tree attachment – number of cycles distribution and critical zone; (**b**) disc groove – number of cycles distribution and critical zone. 88

Figure 10.5. (**a**) blade root radial stress contours; (**b**) blade root von Mises stress contours; (**c**) disc groove radial stress contours; (**d**) disc groove von Mises stress contours. 89

Figure 10.6. (**a**) contact status; (**b**) contact pressure on lobe 1; (**c**) contact pressure on lobe 2; (**d**) contact pressure on lobe 3. 90

Figure 10.7. (**a**) blade fir-tree attachment – number of cycles distribution and critical zone; (**b**) disc groove – number of cycles distribution and critical zone. 91

Figure 10.8. (**a**) blade root radial stress contours; (**b**) blade root von Mises stress contours; (**c**) disc groove radial stress contours; (**d**) disc groove von Mises stress contours. 92

Figure 10.9. (**a**) contact status; (**b**) contact pressure on lobe 1; (**c**) contact pressure on lobe 2; (**d**) contact pressure on lobe 3. 93

Figure 10.10. (**a**) blade fir-tree attachment – number of cycles distribution and critical zone; (**b**) disc groove – number of cycles distribution and critical zone. 94

Figure 10.11. (**a**) blade root radial stress contours; (**b**) blade root von Mises stress contours; (**c**) disc groove radial stress contours; (**d**) disc groove von Mises stress contours. 95

Figure 10.12. (**a**) contact status; (**b**) contact pressure on lobe 1; (**c**) contact pressure on lobe 2; (**d**) contact pressure on lobe 3. 97

Figure 10.13. (**a**) blade fir-tree attachment – number of cycles distribution and critical zone; (**b**) disc groove – number of cycles distribution and critical zone. .. 97

Figure 11.1. Comparison of maximum radial stress on the blade root. 100

Figure 11.2. (**a**) radial stress distribution in $L1,2$ *max* case; (**b**) Comparison of radial stress for the first lobe of the blade root. 101

Figure 11.3. (**a**) Comparison of radial stress for the second lobe of the blade root; (**b**) Comparison of radial stress for the third lobe of the blade root. 103

Figure 11.4. Comparison of maximum radial stress on the disc groove. 103

Figure 11.5. (**a**) Comparison of maximum von Mises stress on the blade root; (**b**) Comparison of maximum von Mises stress on the disc groove. 104

Figure 11.6. (**a**) contact pressure on lobe 1 comparison; (**b**) contact pressure on lobe 2 comparison; (**c**) contact pressure on lobe 3 comparison. 106

Figure 11.7. LCF estimations of the blade attachment. (**a**) Comparison of number of cycles percentage variations respect to nominal results; (**b**) comparison of number of cycles for each case. 107

Figure 11.8. LCF estimations of the disc groove. (**a**) comparison of number of cycles percentage variations respect to nominal results; (**b**) comparison of number of cycles for each case 108

Figure A.1. On the left, a sample with a notch; on the right, the representation of the elastic (grey triangle) and elastic-plastic (dashed triangle) energies. 115

Figure A.2. kσ and $k\varepsilon$ trend respect to notch strain [31]. 116

Figure B.1. Ramberg-Osgood curve [31]. 117

Figure C.1. Cyclic hardening and softening [39]. 118

Figure C.2. (**a**) stabilized hysteresis loop; (**b**) cyclic stress-strain curve [31]. 119

Figure C.3. Example of monotonic and cyclic curves for different metals and alloys [31]. 119

Figure D.1. Typical residual stress profile obtained with shot peening [45]....... 122

Figure D.2. Effect of shot peening on fretting [45]. 123

Figure D.3. (**a**) stress profile generated by the external load; (**b**) stress profile generated by shot peening; (**c**) the effective stress profile is the combination of the two [45]. 123

Figure D.4. Comparison of corrosion fatigue resistance of a peened and of an unpeened specimen operating in industrial atmosphere (top) and in a 5% NaCl solution (bottom) [45]. 124

List of tables

Table 6.1. Considered values for each parameter. 56

Table 6.2. Case studies. 57

Table 9.1. Mesh refinement tests. 72

Table 9.2. Blade attachment stresses. Values are normalized by a reference one.75

Table 9.3. Disc groove stresses. Values are normalized by a reference one..........76

Table 9.4. Peak contact pressures comparison. Values are normalized by a reference one. 78

Table 9.5. Blade root and disc groove LCF results...81

Table E.1. Radial stress comparison. 125

Table E.2. von Mises stress comparison...126

Table E.3. Contact pressure comparison...127

Acronyms

AEN	Ansaldo Energia
BC	Bond Coat
BL	Base Load
CAD	Computer Aided Drafting
CTQ	Critical to Quality
DOE	Design of Experiments
EDM	Electrical Discharge Machining
CMM	Coordinate Measuring Machine
FE	Finite Element
FEA	Finite Element Analysis
GA	Genetic Algorithm
GT	Gas Turbine
HCF	High Cycle Fatigue
LCF	Low Cycle Fatigue
LTE	Life-Time Extension
NDT	Non-Destructive Testing
OA	Optimization Algorithm
OEM	Original Equipment Manufacturer
RES	Renewable Energy Sources
TBC	Thermal Barrier Coating
TGO	Thermal Grown Oxide
TIT	Turbine Inlet Temperature
TVC	Turbine Vane Carrier

Introduction

Background and motivations

In the last decades, the demand of more powerful and efficient gas turbines for energy production has been always grown. This fact pushed the OEM (original equipment manufacturer) company to continuously improve their products or design new ones, able to satisfice the market needs.

Another aspect to be considered is the ever-increasing employment of renewable energy sources (RES) in power generation. RES employment has led to a new operational concept of GTs. In the past they were switched off only when foreseen by maintenance plan and worked for most of the time in design conditions (Base Load, BL). Instead, today GTs have to deal with numerous start-ups and shutdowns to offer support to RES when necessary, and often face up with off-design conditions. Therefore, from a maintenance point of view, endurance limits are reached in a shorter time.

Generally, the gas turbine performance can be improved by increasing the mass flow inside the engine or increasing turbine temperatures both for current design and new one. Usually, new solutions push existing turbine blade always to the limits in terms of stresses or material resistance. Turbine blades are the most stressed components for the centrifugal forces, high operating temperatures, corrosive and erosive conditions.

Considering the current production process of these components, one of the most important phases is the turbine blade fir-tree attachment machining. Usually, turbine blades are casted in nickel super-alloy materials and the process tolerances are reasonable for the airfoil and other surfaces, whereas interfaces with other components of the engine (for example disc groove, dampers, etc.) need a more accurate precision. Hence, the turbine blades are casted with stock material on the fir-tree attachment surfaces and machined in a second phase. Furthermore, tolerances request for the coupling with other components must be very tight and the surface roughness very low. All these requirements are mandatory to guarantee the component lifing and foreseen maintenance plan.

All this information is reported into the machining drawings of the fir-tree attachments. Each supplier of the machining phase must respect all requirements and provide critical-to-quality measurements to be able to guarantee the required tolerances.

Machining tolerance ranges are based on OEM experience on turbine blade manufacturing and knowledge of the material limits. Nevertheless, a correct balance between the design target and the manufacturing cost has to be considered.

According to [1], fatigue failure of a blade fir-tree attachment can be related to four causes: localized stress concentrations generating high cycle fatigue (HCF); repeated switch-on and shutdown causing low cycle fatigue (LCF); relative micro slips in blade-disc contact surfaces under high loads leading to fretting fatigue, and finally creep-fatigue interaction. Creep-fatigue interaction occurs because of high operating temperatures and loads.

The work presented in [2] focuses on the effect of design tolerances on load distribution and fatigue life in a blade fir-tree attachment. Modified geometries were obtained through Monte-Carlo simulations. FEA analysis showed that load distribution on teeth wasn't uniform, leading to plastic regions and LCF reduction. They concluded that load would be better distributed on teeth and grooves and fatigue life increased by optimizing geometry tolerance ranges and better balancing the airfoil.

In his work [3] in his thesis work analysed new blade fir-tree attachments with barrel active planes. This design solution was expected to reduce stresses especially on blades attachment contacts. Results showed that curved contacts extend attachment life decreasing peak pressures on contacts. In the same work, it was taken into consideration the effect of manufactory tolerances on blade attachment. Results showed a 60% increment in peak von Mises stress.

In [4] authors worked on minimization of stress distribution in terms of von Mises stress, principal stresses, shear stress and contact pressures depending on the combination of a set of geometrical parameters, i.e., bottom flank angle, skew angle, and number of teeth. They aimed to minimize the impact of fretting fatigue on a blade fir-tree attachment. They obtained two optimum geometries: the first one was obtained by searching the minimum of stresses all together simultaneously, the second one instead was obtained by minimizing the stresses one by one.

Other researchers tried to obtain an optimum blade attachment geometry using optimization algorithms (OA). Single-objective [1],[4]-[8] and multiple-objective [9] functions in genetic algorithms (GA) were tested to find an optimum attachment geometry, where the output to be optimized (i.e. minimized) were stresses [1],[5],[7],[9], contact pressures [9],[10], mass [6] or plastic strain [8]. Each trial performed by the algorithm is a FEA, by consequence the main issue of OA is their high computational cost. For this reason, different solutions were implemented to reduce it. An adopted way is embedding metamodels (or surrogated models) in the algorithm: they essentially are simplified models of the model. They are used to reduce the number of call-backs of the high-fidelity FE model [6]. Metamodels are built using Design of Experiments (DOE) points: DOE relate input variables to key output variables through experimental tests. Another adopted solution is using a penalty method. They apply penalty factors to non-feasible solutions before running the OA. Examples of these methods are adaptive penalty method and death penalty method [5]. To further speed up the convergence, in the work presented in [5] it was also developed an in-house analytical tool to be used in the 1D conceptual design phase. It excludes non-feasible 1D solutions from the searching domain before applying penalty methods and the OA. All the just cited papers [1],[4]-[10] searched for the attachment optimum geometry, they don’t investigate the effect of manufactory tolerances.

Objective

The goal of this study is to deeply investigate the stress status of the fir-tree attachment of a turbine blade by means of FEA, detailed analyses of the contacts and the following lifing.

Then, tolerance ranges of different fir-tree attachment parameters will be analysed, correlating them with the nominal geometries. It is important to carry out a statistical analysis on the out-of-tolerance to understand which parameters are more relevant or affected.

Finally, some FE analyses of the tolerance limits and out-of-tolerance values will be performed to better evaluate their impact on components lifing and to be able to better judge non-conformities. The component life assessment has been performed by means of Ansaldo Energia LCF in-house tools. Furthermore, also a stress gradient approach has been applied to better evaluate the stress intensification due to notches in the contact areas and to obtain more reliable fatigue damage results.

A results comparison between LCF in-house tools and stress-gradient approach has been performed and reported for the blade. For sake of completeness, also the disc lifing has been evaluated by means of a dedicated LCF in-house tool, more specific for the disc material.

In conclusion, a detailed comparison between different out-of-tolerances parameters is reported and discussed.

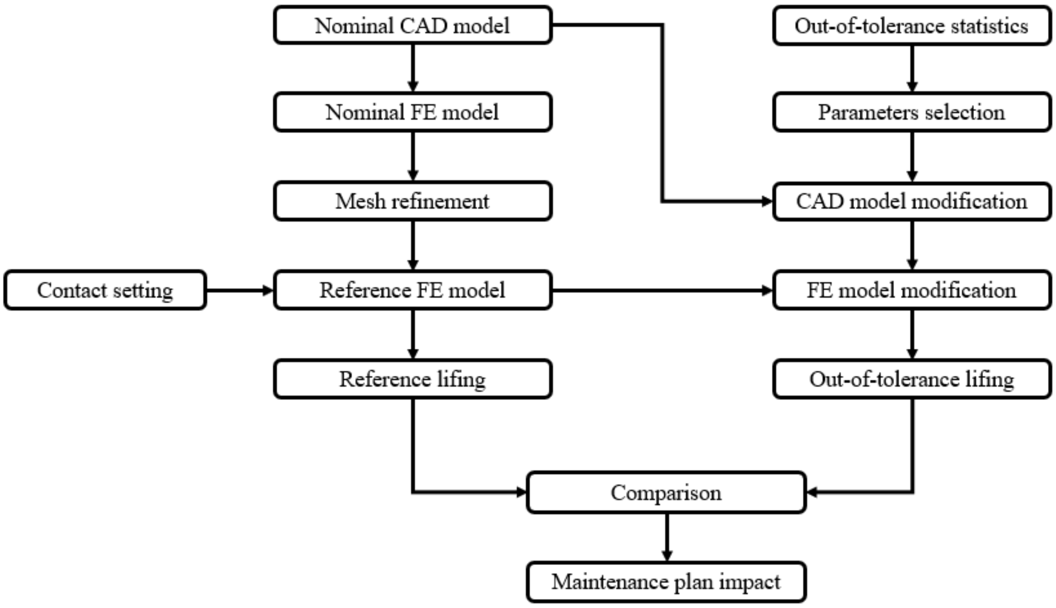
Nominal CAD model
Nominal FE model
Mesh refinement
Contact setting
Reference FE model
Reference lifing
Out-of-tolerance statistics
Parameters selection
CAD model modification
FE model modification
Out-of-tolerance lifing
Comparison
Maintenance plan impact

Figure 0.1. Procedure workflow.

The flowchart reported above shows the steps we need to take to get to the prefixed goal.

The work started from the preparation of a nominal 2D CAD model form the 3D one (section 0) by cutting the 3D CAD with a plane. The 2D CAD was imported in *ANSYS* to set the nominal FE model in terms of boundary conditions (section 8.1), material's properties, mesh (section 9) and contact surfaces (section 8.2).

In order to achieve mesh-independent results, a mesh refinement process was performed, decreasing each time the element size near the contact surfaces (section 9). For each mesh size, a FEA was performed and results were compared with the other mesh sizes results to find an asymptotic trend. At the same time, different contact options were modified to best set the contact to guarantee reliable results (section 8.2). After these phases, the reference FE model was set in terms of contact options and mesh size (section 9.4).

The reference FE model has been used to all the out-of-tolerance cases, changing only the CAD model each time and maintaining all the other settings (section 1). Reference parameters were chosen starting from a statistical analysis on out-of-tolerances (section 4).

Elastic and elastic-plastic FEA results has been used to estimate the nominal geometry lifing (reference lifing, section 10.1), tolerance limits and out-of-tolerance geometries lifing (sections 10.2, 10.3, 10.4) using two Ansaldo Energia in-house tools and a stress gradient approach.

Finally, a comparison (section 11) between tolerance limits, out-of-tolerances and nominal geometry results was discussed, to better understand out-of-tolerance impact on component's lifing.

1. General gas turbines description

A gas turbine (GT) is a machine which takes air from the environment, makes it perform a thermodynamic cycle and finally discharges exhaust gas in the environment with the aim to extract work that can be used in different ways, depending on the application business. For example, in aeronautical and nautical businesses work is used to produce thrust, while in the energy business work is employed for produce electric energy. Each business has its own finalities, requirements and final costumer, and this determinate the way gas turbines are realized. In general, the technology is very similar in every application, but there are some aspects that distinguish the design in different business. In energy business gas turbines are called "heavy duty" GT. **Figure 1.1** shows an example of a gas turbine [11].

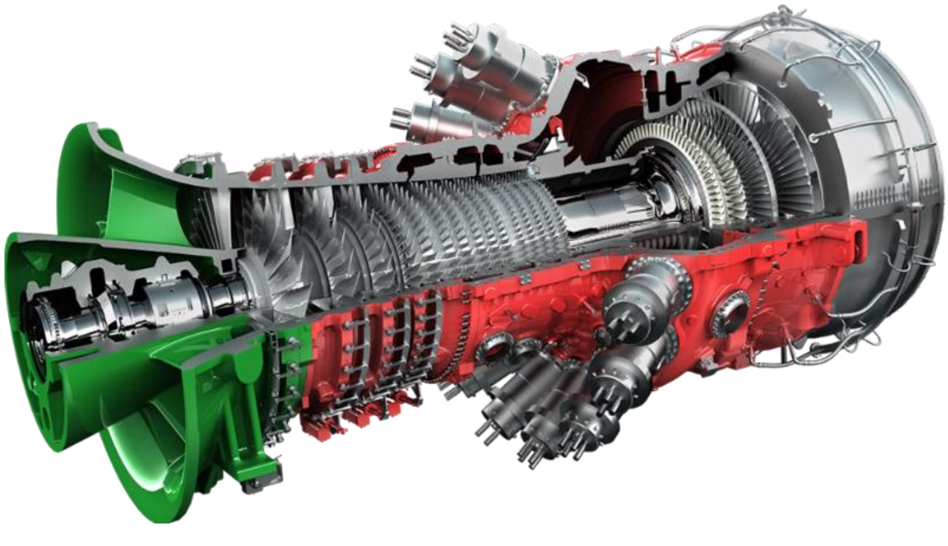

Figure 1.1. GT36, class H gas turbine produced by AEN [12].

1.1. Joule-Brayton thermodynamic cycle

Gas turbines are based on Joule-Brayton cycle, that is represented in **Figure 1.2**a (ideal) and **Figure 1.2**b (real).

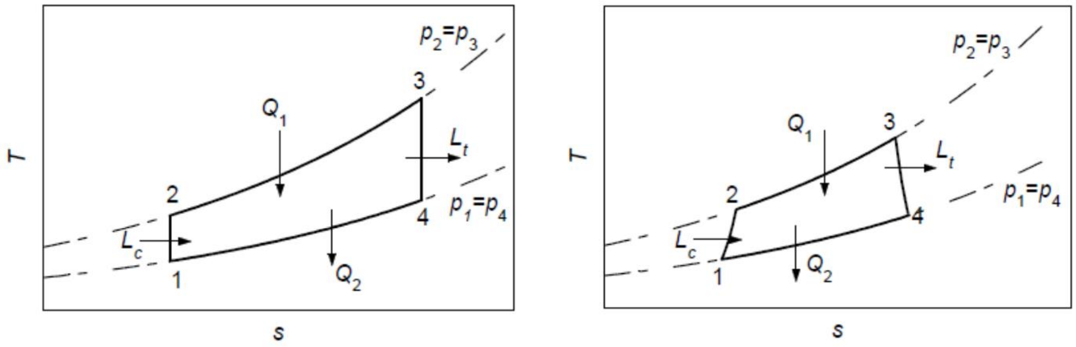

(**a**) (**b**)

Figure 1.2. (**a**) Ideal Joule-Brayton cycle [13]; (**b**) Real Joule-Brayton cycle [13].

Ideal cycle	Real cycle:
Phase 1→2: isentropic compression	Phase 1→2′: polytropic compression
Phase 2→3: isobaric combustion	Phase 2′→3′: combustion with pressure drops
Phase 3→4: isentropic expansion	Phase 3′→4′: polytropic expansion
Phase 4→1: exhaust discharge	Phase 4′→1: exhaust discharge

Ideal Joule-Bryton cycle is composed of two isentropic (1→2 and 3→4) and two isobaric (2→3 and 4→1) transformations. Instead, real Joule-Bryton cycle is composed of two adiabatic (1→2′ and 3′→4′) and two isobaric (2′→3′ and 4′→1) transformations [13].

L_c is the work consumed by the compressor i.e., work done on the system (air) by the environment (compressor), L_t is the work extracted by the turbine, i.e., work is done by the system (hot gas) on the environment (turbine). Q_1 is the heat provided to the system during the combustion phase, Q_2 is the heat lost by the system during the discharge phase [13].

The thermodynamic efficiency of the Joule-Bryton cycle is defined as [13]:

$$\eta = \frac{L_t - L_c}{Q_1} \tag{1.1}$$

1.2. Gas turbines architecture

Gas turbines are always composed by an intake, a multistage (usually axial) compressor, a combustor, a multistage axial turbine, and a nozzle. Scheme is reported in **Figure 1.3**. Air enters from the intake, gets compressed by the compressor, then goes in combustion chamber to react with the fuel, pass through the turbine where it expands and finally is discharged outside by the nozzle. All these parts undergo a different design process, everyone with its characteristics and challenges [11].

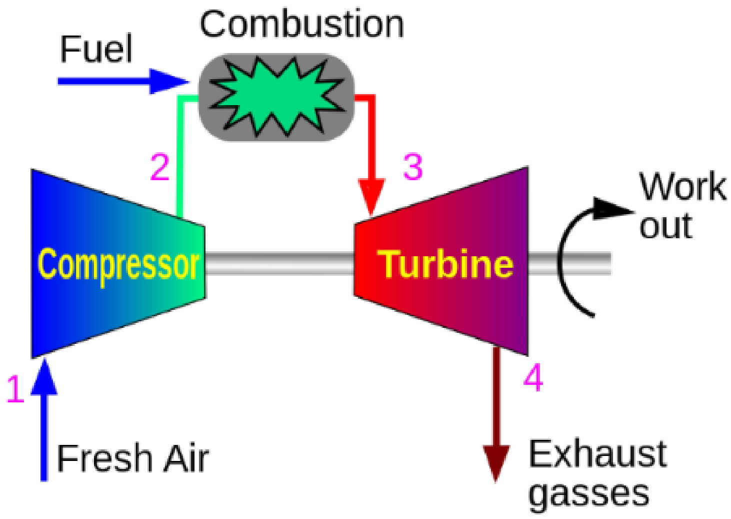

Figure 1.3. Gas turbine scheme [14].

1.3. Gas turbine stage description

A compressor stage is composed of a blade and a vane, while a turbine stage is composed of a vane and a blade, in this order. In general compressors have from ten to fifteen stages while turbines have three or four stages. The difference has a fluid-dynamic reason: too high adverse pressure gradient in compressor stages can lead to stall and therefore it is necessary to compress smoothly. On the other hand, expanding air generates favourable pressure gradient, therefore there is no risk of stall and by consequence it is possible to expand very rapidly and less stages are needed in turbine [15].

Compressor blades and vanes are in steel alloy and obtained by milling, while turbine ones, due to their complexity, are realized by micro-fusion and are generally in Nickel superalloy [16].

1.3.1. Vanes

Vanes are the stationary parts of gas turbine; their job is to deflect flux and to increase (in turbine) or decrease (in compressor) fluid kinetic energy. Increasing fluid kinetic energy means expanding it, while decreasing kinetic energy means compressing it. They do not exchange work with the fluid, they only redirect the flux to be optimal for blades [17].

Vanes are kept into position by the Turbine Vane Carrier (TVC). The TVC interfaces the vane with the outer casing of gas turbines. In the hub section, vanes can be connected to the U-ring, a component which ensures that hot gas does not enter internally into the rotor or directly interfaced to rotating components.

Generally, TVC is used by all producers, U-ring is a technical solution adopted by some OEM like AEN. The example figure below illustrates a typical vane [15].

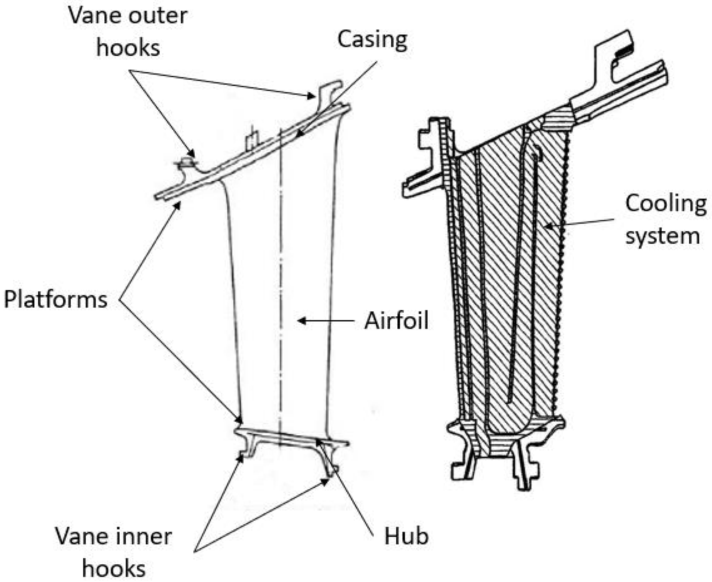

Figure 1.4. Example of Turbine vane illustration [15].

Hooks serves to ensure connection between vane and TVC (outer hooks) and between vane and U-ring (inner hooks). The inner radius zone is called hub, while the outer radius zone is called casing. Platform's role is to ensure the correct fluid flow-path by confining it between hub and tip. Finally, only in turbine vanes there is a cooling system composed of internal channels and holes [16].

1.3.2. Blades

Blades are the rotating parts of the gas turbine, their main task is to exchange work with the fluid, but they also deflect the flux and increase (in turbine) or decrease (in compressor) its kinetic energy (this last one can be done or not depending on speed triangles) [17].

Work is taken by the fluid and a part is used to drive the compressor through a shaft and the remaining part is used to drive a generator thus producing electricity [17].

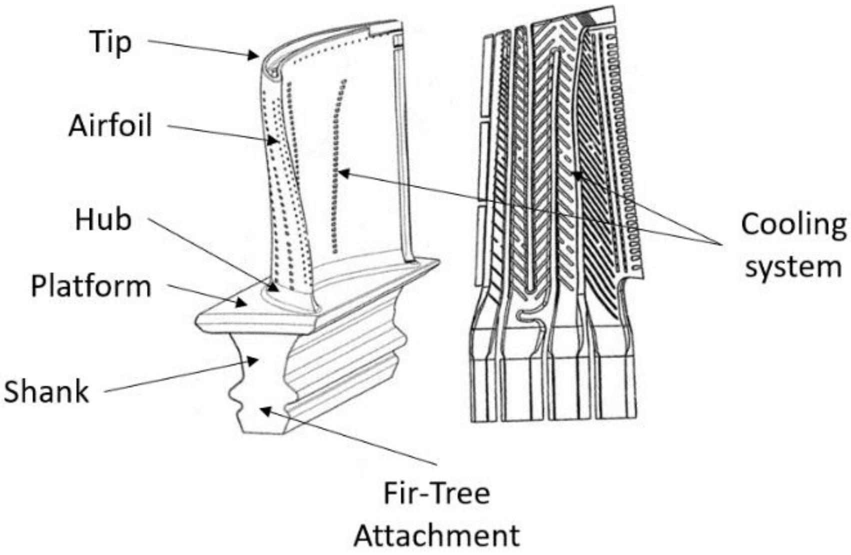

Figure 1.5. Example of Turbine blade illustration [16].

The upper zone of blade is called tip, and it has a squealer part on it whose task is to avoid as much as possible fluid tip leakage. The lower zone of the blades instead is called hub. As **Figure 1.5** shows, blades have an airfoil that is twisted of a certain angle from the hub to the tip to guarantee the best angle of attach at each section. Platform, as for vanes, ensures that hot gas remains in the desired flow path. Blades are mounted on the turbine disks through the attachment, which in most cases is a fir-tree attachment. This part is the most critical of the blade since huge centrifugal forces are sustained only by the attachment. Between the platform and the fir-tree attachment, there is the shank which has to ensure a smooth stress transition from the previous parts cited. Finally, only for turbines, film cooling holes on blade surface and internal channels are present that enable cooling [16]. Focus now will be put on turbine and on blades.

1.4. Turbine cooling system

Both blades and vanes, especially in the first stages, needs a cooling system to withstand high temperature gas from combustor outlet. Figure below shows an example of how blades and vanes are cooled.

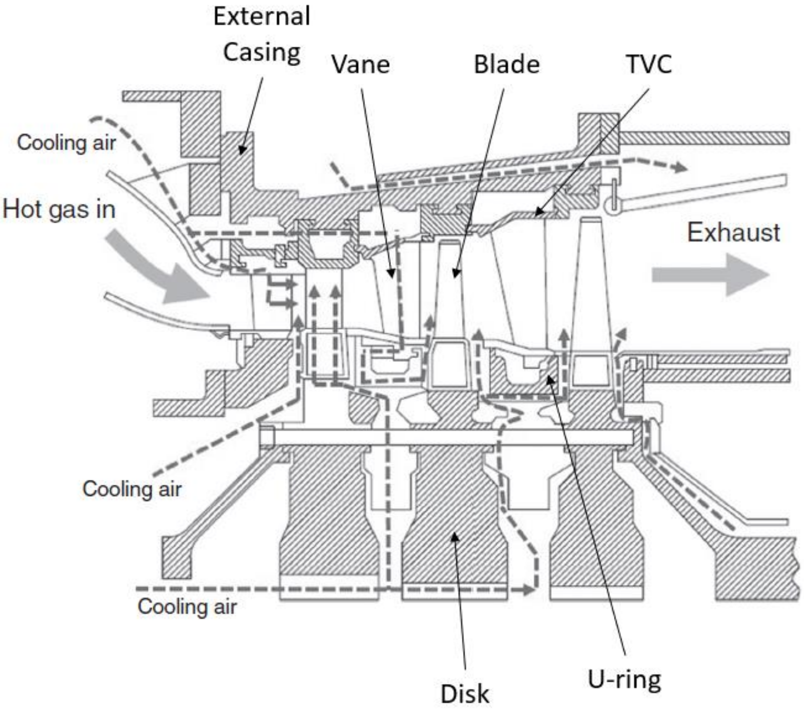

Figure 1.6. Turbine cooling system [18].

Cooling air is taken from different bleeds in compressor stages (usually both low pressure and high-pressure bleed) and gets to blades and vanes through secondary fluxes channels. There are several cooling technologies at the current state-of-art, developed throughout years. This development allowed to increase turbine inlet temperature (TIT) and therefore improve performances.

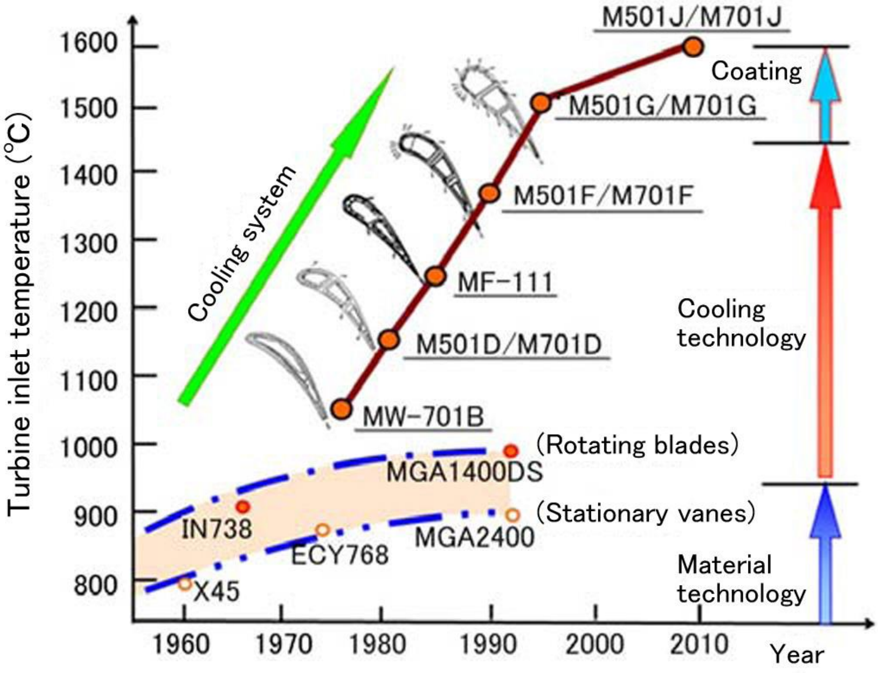

Figure 1.7. Example of TIT increasing thanks to new cooling technologies [19].

As reported in **Figure 1.7**, TIT is sensibly higher than metal melting temperature, so that it is necessary to perform blades cooling to allow them to operate without failure [19].

In the following paragraphs we now discuss some cooling technologies:

- *Film cooling*: coolant is injected inside the blade and passes through different holes located on blade surface. In this way coolant forms a thin layer on blade surface and protects walls from hot gas. For this reason, film cooling is an external cooling. More efficient technologies make coolant pass through a serpentine thus taking out more heat. It has to be taken into consideration that from one hand we want to exploit in the best way possible coolant, but on the other hand we are limited by structural and technological boundaries [19].

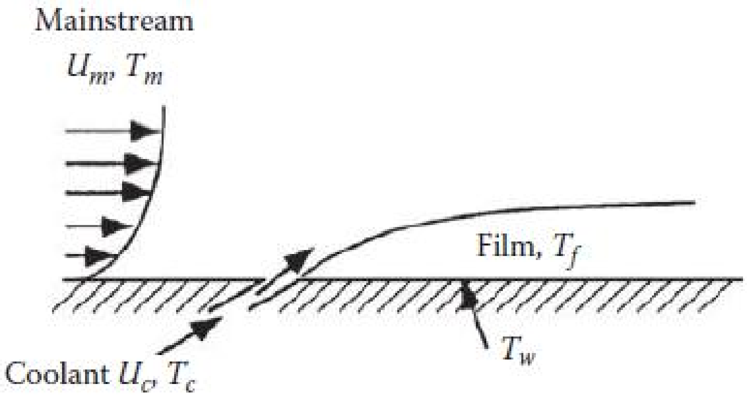

Figure 1.8. Film cooling [19].

Figure 1.8 shows how film cooling works, where U_m is hot gas speed, U_c is coolant speed, T_m is hot gas temperature, T_c is coolant temperature, T_w is blade wall temperature, T_f is coolant film temperature [19].

- *Jet impingement cooling*: it is a type of internal cooling. Coolant enters the impingement baffle, a sort of tube with an airfoil shape, and passes through the holes that are on its surface creating several jets. There is a space intentionally left void between impingement baffle and blade internal wall; jets enter this region and locally impinge on blade wall and cools it. Finally, coolant exits from the holes located on blade surface and performs an additional film cooling externally. Impingement cooling exploits turbulent boundary layer to enhance heat-transfer coefficients. The drawback of this technique is that weakens blade structural integrity because requires thinner blade walls. Hence, impingement is suitable for regions with high thermal loads, such as blades leading edge, or vanes where acceptance criteria are less severe [19].

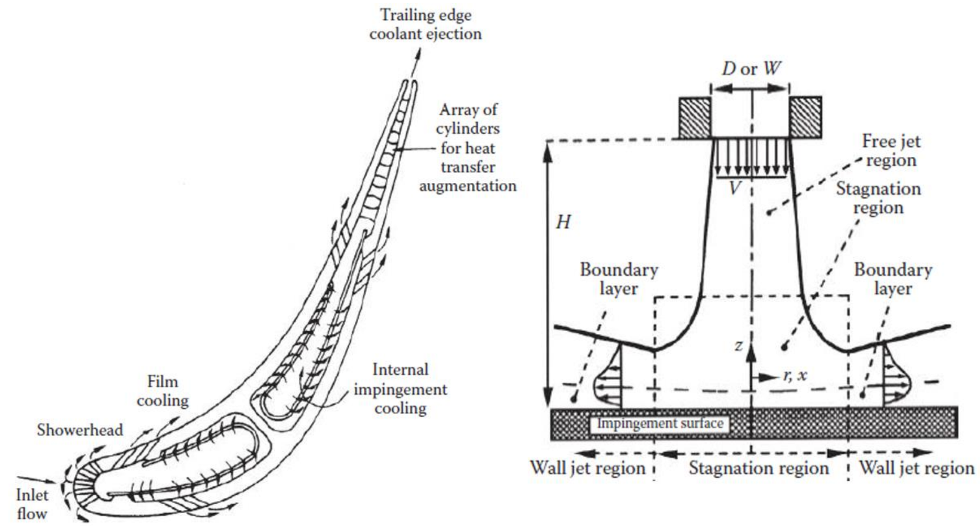
Trailing edge coolant ejection
Array of cylinders for heat transfer augmentation
Internal impingement cooling
Film cooling
Showerhead
Inlet flow
D or W
Free jet region
V
Stagnation region
H
Boundary layer
Boundary layer
z
r, x
Impingement surface
Wall jet region
Stagnation region
Wall jet region

Figure 1.9. Example of Jet impingement cooling [19].

- *Rib-Turbulated cooling*: this technique consists of inserting different ribs all over the blade internal channels and use them like a fluid dynamic obstacle: they cause boundary layer separation and reattach many times to promote transition to turbulent flow. In this way heat-transfer is enhanced. Performance depends on ribs shape and angle (respect to flow direction), channels aspect ratio and Reynolds number. More efficient cooling is obtained by inserting serpentines instead simple straight channels inside the blade. Rib-turbulated cooling is mostly used in blade middle section [19].

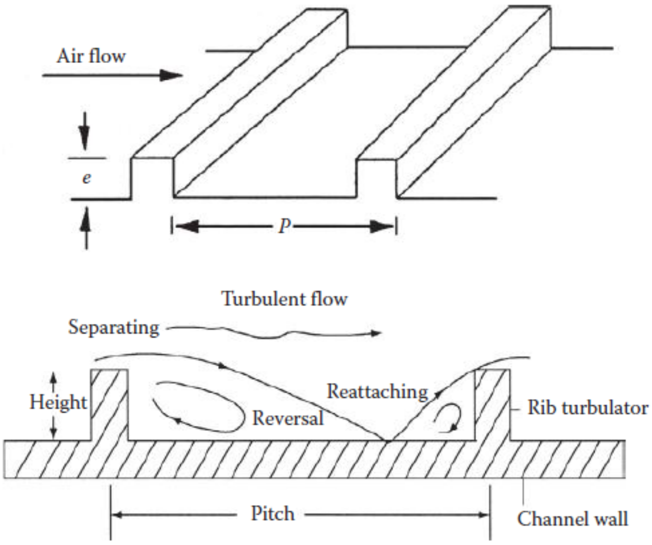
Air flow
e
P
Turbulent flow
Separating
Height
Reattaching
Reversal
Rib turbulator
Pitch
Channel wall

Figure 1.10. Example of Rib-turbulated cooling [19].

- *Pin-fin cooling*: cooling technique that consists of inserting several cylinders called pins perpendicularly to flux direction and forcing coolant to pass through them. Flux becomes turbulent thus increasing heat-transfer efficiency. Performances depend on pins array arrangement (linear or staggered), pins shape, Reynolds and Nusselt number. Mostly used for blades trailing edge where rib-turbulated and impingement cooling are not feasible cause of manufacturing constraints. Limitation comes from pressure drop between upstream and downstream the pins: increasing pins number causes a decrease in downstream pressure thus conducing to possible hot gas ingestion by cooling channels [19].

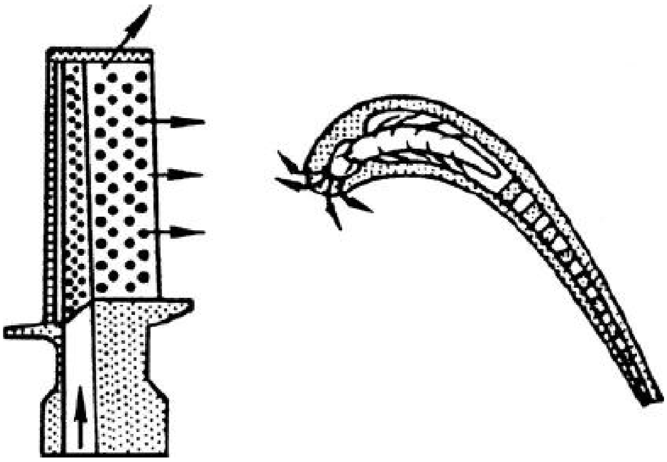

Figure 1.11. Example of Pin-Fin cooling [19].

Cooling air is compressed air taken form the compressor's bleeds. This has two main consequences: first, a part of the working fluid doesn't take part to combustion, and it is not possible to extract work form it; second, cooling air has consumed a part of the available work to be compressed. Hence, GT overall performances are affected.

In conclusion, a compromise choice has to be between the advantage of increasing working temperatures and disadvantage of bleeding air from the compressor (and increase system complexity).

1.5. Turbine vane and blade coating

Together with always more efficient cooling technologies, with the aim of increasing working temperatures, it has been necessary to introduce heat shields that covers blades and vanes and protect them from hot gas.

The figure below shows the TIT increasing over the years highlining coatings contribution.

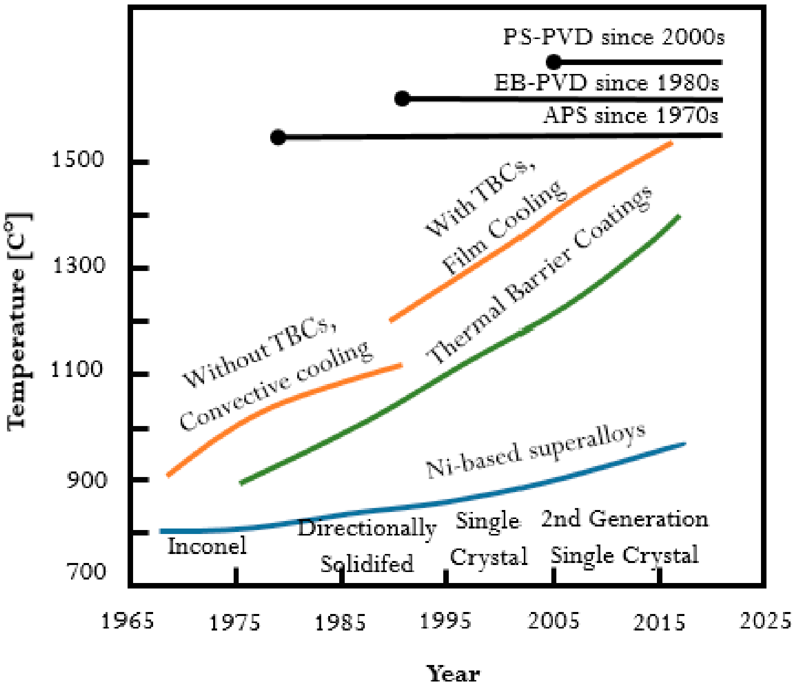

Figure 1.12. TIT evolution though the decades [20].

There are two types of coatings that are realized on turbines blades and vanes. The first one is called Thermal Barrier Coating (TBC) and the second one is called Bond Coat (BC).

- *Thermal Barrier Coating*: it consists of covering blades and vanes surfaces with a ceramic layer characterized by low heat conductivity so that base metal is protected. However, oxygen can pass through this layer and can oxidase base material (Nickel superalloy) [20].
- *Bond coat*: it is a metallic coating put between base material and TBC. Its function is to ensure good TBC bonding on the blade/vane and to protect base material from oxidation. Oxygen reacts with bond coat metal forming an oxide

called Thermal Grown Oxide (TGO) which thickness grows up during gas turbine functioning until it causes TBC rupture. Usually, bond coat is realized with aluminium and therefore TGO is Alumina (Al_2O_3) [21].

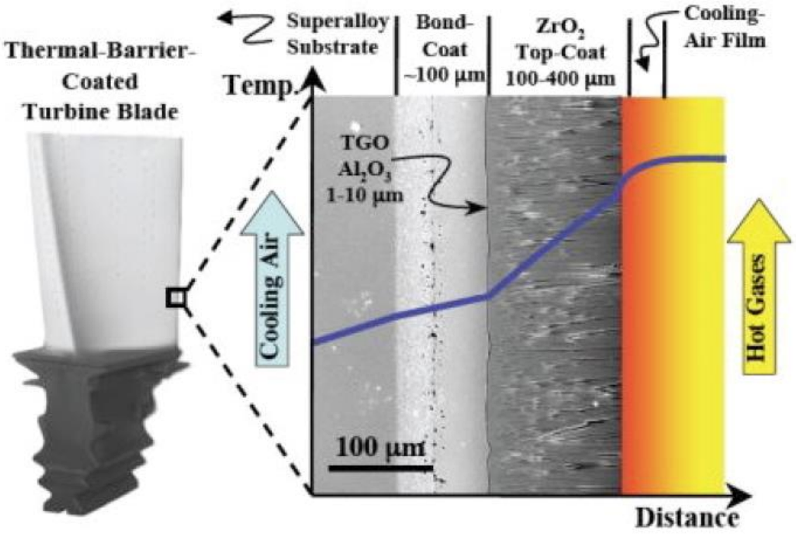
Thermal-Barrier-Coated Turbine Blade
Superalloy Substrate
Bond-Coat ~100 µm
ZrO_2 Top-Coat 100-400 µm
Cooling-Air Film
Temp.
TGO Al_2O_3 1-10 µm
Cooling Air
Hot Gases
100 µm
Distance

Figure 1.13. Coatings scheme [22].

As said in section 1.4, coolant is air taken from the compressor at relative high temperature therefore internal surfaces can be oxidized. To protect blades and vanes from oxidation an internal coating in aluminium is also realized [16].

1.6. Turbine blade design workflow

Blades are the most critical components in gas turbines for several reasons. They have to deal with centrifugal force, high temperature gas and at the same time they exchange forces with the gas to compress/expand it. Although also vanes are in contact with hot gas, their design is a little bit easier given that they are not subjected to centrifugal force (they do not rotate).

Blades design is an interdisciplinary process, in this process are involved aerodynamics, heat transfer, mechanical design and mechanical integrity. All these disciplines cooperate to achieve the best compromise in terms of performance, reliability, and durability. The design process consists of different loops, where all the study fields are strictly dependent one to the others, the results obtained from one field changes depending on another field's results [16].

Design process consists of different phases, as shown in Fig. 2.15.

In conceptual design input are rough parameters, such as mean values at middle span and at the end of this phase you decide if the realizing such blade is feasible or not [16].

It is important to remark that conceptual design has to be much reliable as possible, given that basic design depends on it and this last one takes a lot of time to be carried out. New technologies, for example new turbine cooling, new materials, new combustion chambers, new machining processes, etc. that you want to employ for developing a new product has to be chosen in conceptual design phase and you cannot change them in the following phases. Hence, it is important to say that in parallel with designer team, there must be one or more teams that have to work on these new technologies. This is true not only for blades, but also for all components of gas turbines and, more in general, for every technological product [16].

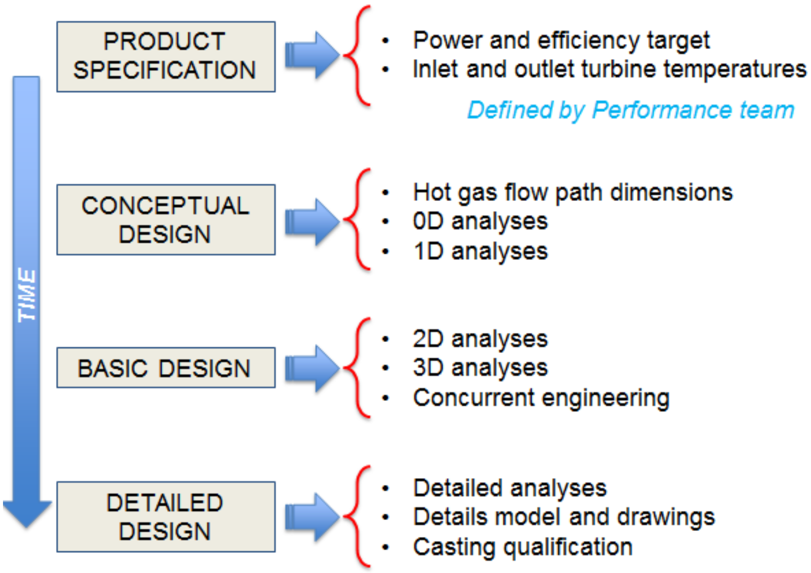
PRODUCT SPECIFICATION
Power and efficiency target
Inlet and outlet turbine temperatures
Defined by Performance team
CONCEPTUAL DESIGN
Hot gas flow path dimensions
0D analyses
1D analyses
TIME
BASIC DESIGN
2D analyses
3D analyses
Concurrent engineering
DETAILED DESIGN
Detailed analyses
Details model and drawings
Casting qualification

Figure 1.14. Blades design process [5].

Basic design gives you much more information, such as temperatures, pressures and stresses all over the surfaces, but also data about secondary fluxes, in steady and unsteady state. Moreover, you can have modal and creep analysis results, and you can estimate blade’s fatigue life [16].

Finally, detailed design provides you even more specific information, such as thermo-mechanical fatigue, 3D detailed CAD, the effect of start-up and shut down transients on lifing, the effect of oxidation [16].

After the design process there is the prototyping phase where the casting process, machining process and special processes are chosen. In the end, there is the validation process where the prototype goes under dimensional checks, airflow measurements, non-destructive testing and several other tests to ensure its compliance [16].

1.7. Turbine blades machining processes

As said in section 1.3, blades and vanes are casted. It should be said a lot of things about casting process, but for the aim of this study we focus on machining processes. Although casting technologies have reached high precisions, blades attachment geometry requires a level of precision that cannot be satisfied by casting process. Therefore, after casting it is necessary to execute a machining phase on attachments to achieve required precision [16].

Due to their enhanced mechanical properties, Nickel superalloys are difficult to machine thus special machining processes are required [16].

1.7.1. Creep feed grinding

Creep feed grinding is a particular type of grinding in which highly abrasive materials are used. In this way, it is possible to remove material at greater depths with each tool passage compared to traditional grinding thus reducing processing times. These characteristics, considering Nickel superalloy hardness, make creep feed grinding the only one process that allows to achieve blades attachment required precision in an acceptable amount of time [16].

Through grinding process, we want to achieve certain characteristics on attachment profile, such as:

- Dimensional precision required for a mechanical coupling.
- Very low roughness.
- Absence of working imperfections (cracks for example).
- Base material micro structural required quality [16].

All these requirements have to be satisfied to:

- Ensure correct blade mounting on the disk (blade attachment is the male part of the coupling between blade and disk).
- Ensure uniform stress distribution on the working planes.
- Avoid excessive clearance that can lead to vibrations or mechanical stresses on the attachment during operation [16].

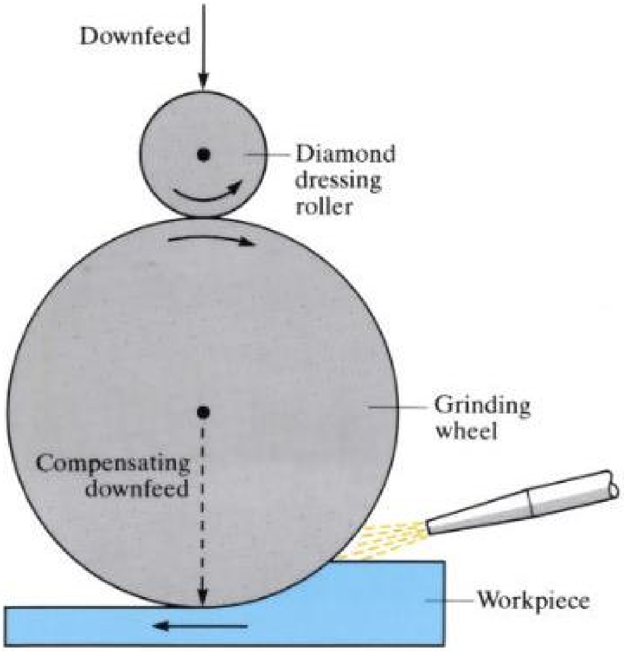

Figure 1.15. Creep feed grinding [23].

There are two main tools that are used in creep feed grinding [16].

The first one is the diamond dressing roller: it is a steel cylinder covered with a diamond layer. Its geometry depends on the piece you have to work, and in particular it has the same profile as the piece. In the case of turbine blade attachment, the diamond dressing roller copies attachment profile with very high precision. Its functions are creating the negative of the piece profile on the grinding wheel and keeping grading wheel correct shape and sharpness. Due to the materials employed, diamond miller costs are relevant. Diamond is the only material that can be employed in such tools because of grinding wheel hardness [16].

The second one is the already cited grinding wheel: it is composed of different abrasive grains kept together by a binder. There are different types of grinding wheels, depending on:

- Abrasive grain material (aluminium oxides, silicon carbides, diamond) and its hardness and mechanical properties.
- Abrasive grain dimensions.
- Type of binder.
- The force that keeps together abrasive grains which is called grinding wheel hardness.
- Binder porosity: cavities get filled with lubricant-coolant fluid hence a greater number of cavities allow better cooling and lubrication [16].

Grinding wheels for Nickel superalloy employs aluminium oxide abrasives and a quite porous binder in resin [16].

A fluid which has to work both as lubricant and coolant, called lubricant-coolant fluid, is required to manage with the great friction loads generated. An important role is covered by this fluid, and its main functions are:

- Lubricating surfaces that are in contact to reduce friction.
- Cooling tools and piece taking away heat produced by friction.
- Keeping grinding wheel on correct working temperature.
- Taking away processing debris [16].

A non-optimal lubrication and cooling can lead to superficial cracks due to overheating, geometry non-compliances or low-quality roughness [16].

There are two main working method, they are called Continuous Dressing and Non-Continuous Dressing. In Continuous Dressing the grinding wheel is kept in contact with the diamond cutter thus preventing grinding wheel consumption. Usually, this method is applied in the first working phases allowing to remove a lot of material with each tool passage. Instead, in the last phases, where you want to achieve low roughness and high dimensional precision, contact is removed, and Non-Continuous Dressing is applied. Therefore, the first working phases are characterized by high mechanical and thermal loads, while the last phases are characterized by lower loads [16].

Creep feed grinding advantages are working time reduction, repeatability of the process and creation of complex surfaces with high dimensional precision. While drawbacks are the employment of complex tools and their costs and long setup times [16].

To speed up the process both pressure side and suction side of the attachment are grinded simultaneously thanks to double spindle tools. Another advantage of using such tools is avoiding the so-called bow effect that is a phenomenon that consists of the creation, on the opposite side you are working on, of residual stresses. Moreover, a further advantage is that the processing precision is the same as the tool's one without other possible errors (no intermediate steps or positioning) [16].

Given that involved loads are considerable, the piece has to be firmly fixed to the clamp [16].

Machining blade drawings establishes some references called datum that are used to verify the process. This ensures positioning repeatability for each piece processed [16].

After grinding it is necessary to do dimensional checks and, considering the required tolerances, it has to be carried out with Coordinate Measuring Machines (CMM). They have an element called touch probe which explores piece surfaces. The CMMs have internal references that the touch probe uses to start measuring. After measuring, CMMs register the measure just obtained and compare it to the theoretical one. Finally, CMMs report the measures on a file that is available to the checking personal [16].

Turbine blades costs are relevant, so it is fundamental to try to have less non-compliance related to grinding as possible. For this aim, a first test is done on a blade having stock material and before the refinement it goes under measure controls. Other tests are performed to ensure correct blade positioning on the tool [16].

In the end, to be sure that the processing has not create defects on the surfaces (usually related to overheating), a check using fluorescent penetrant liquids is done. This check has a great importance in blades validation because presence of cracks of cavities can lead to blade failure during operation [16].

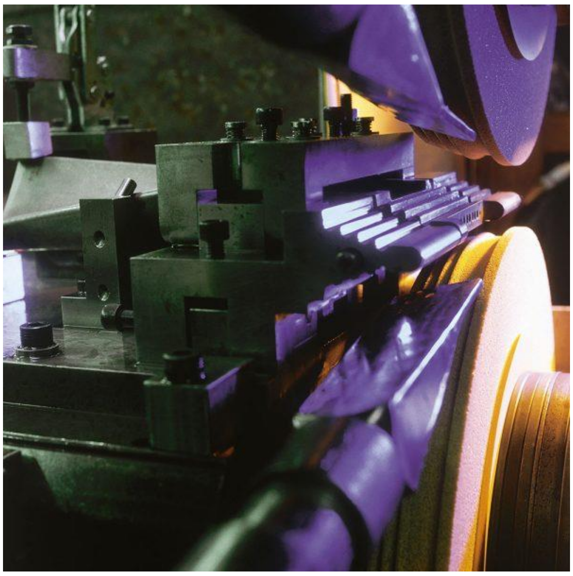

Figure 1.16. Creep feed grinding of a blade root [24].

1.7.2. Electrical Discharge Machining

Electrical Discharge Machine or EDM, is a machining process that removes material from the piece exploiting a series of controlled electrical discharges (hence the name of this technology) between the tool (electrode) and the processing piece at high frequency. The result is localized micro-fusions and consequent removal of material. The principle is that a conductive material can be eroded by electrical discharges. Each discharge creates a crater on piece surface. This technology is called unconventional machining and the reason is that the tool and the workpiece never get in contact with each other [25].

The space between tool and piece, called gap, is filled with a dielectric fluid [25]. An EDM scheme is reported in the following picture.

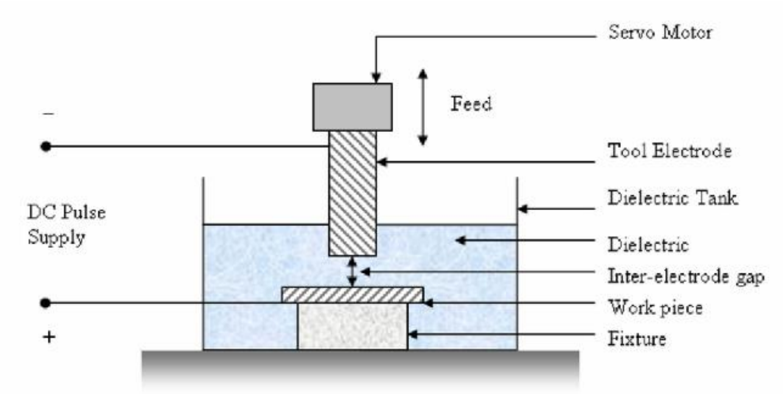

Figure 1.17. EDM scheme [25].

Dielectric employed depends on the specific technology, and its main functions are:

- Acting as electric insulant during the formation of the discharge channel.
- Stabilizing electrical discharges.
- Precisely defining the discharge area.
- Cooling the tool and the piece.
- Cleaning the gap from the debris produced: debris could reduce dielectric insulating effectiveness thus leading to uncontrolled discharges [25].

Electrical discharge phenomenon can be divided in nine different phases:

1) The electrode (positive pole) gets near the workpiece (negative pole) and the voltage increases.
2) The discharge channel gets formed. Dielectric is now partially ionized. In this phase voltage is constant and current is zero.
3) The insulant effect of the dielectric is now null. Voltage decreases while current increases. This is the first stage of the discharge.
4) Protons go towards the piece while neutron go towards the electrode. Voltage further decreases and current further increases. Electrode and dielectric vapours generate a pocket around the discharge.
5) Discharge channel grows, voltage and current stabilize. The just created magnetic field generates a plasma channel.
6) Discharge reaches maximum intensity. Temperatures locally can reach even ten thousand Celsius degrees and causes piece fusion or evaporation.

7) In this phase circuit gets opened. Local temperatures quickly decrease leading to metal re-solidification forming micro-particles.
8) The pocket around the discharge channel implodes and throws away eroded material.
9) Process restart [25].

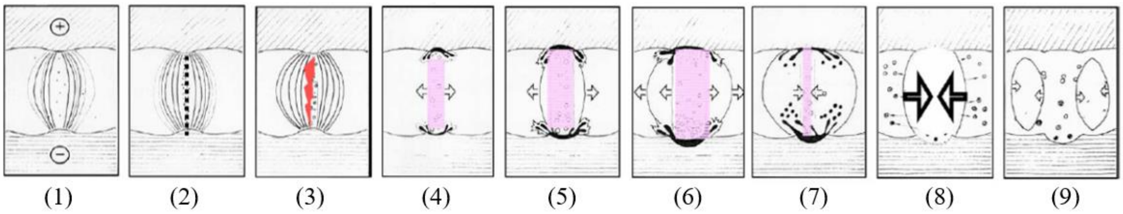

Figure 1.18. EDM discharge phases. [25].

There are different types of EDM depending on the electrode employed. In die-sink EDM the electrode has a three-dimensional shape which is the negative of the piece you have to work on. Another EDM technology utilizes metal wires, called Wire-cut EDM. Finally, there is EDM drilling which uses hollow rods with circular section. In this case, the discharge is confined inside of the rod [25].

Electrodes can be realized in different materials, such as Copper, Aluminium, Copper-Tungsten, brass and graphite [26].

In Die-sink EDM dielectric used is a hydrocarbon fluid characterized by very low viscosity, while for the other two cited types of EDM it is distilled water [16].

EDM advantages are repeatability, extreme precision, possibility to realize complex surfaces. Disadvantages are long time required for the machining, electrodes costs and their complex production [25].

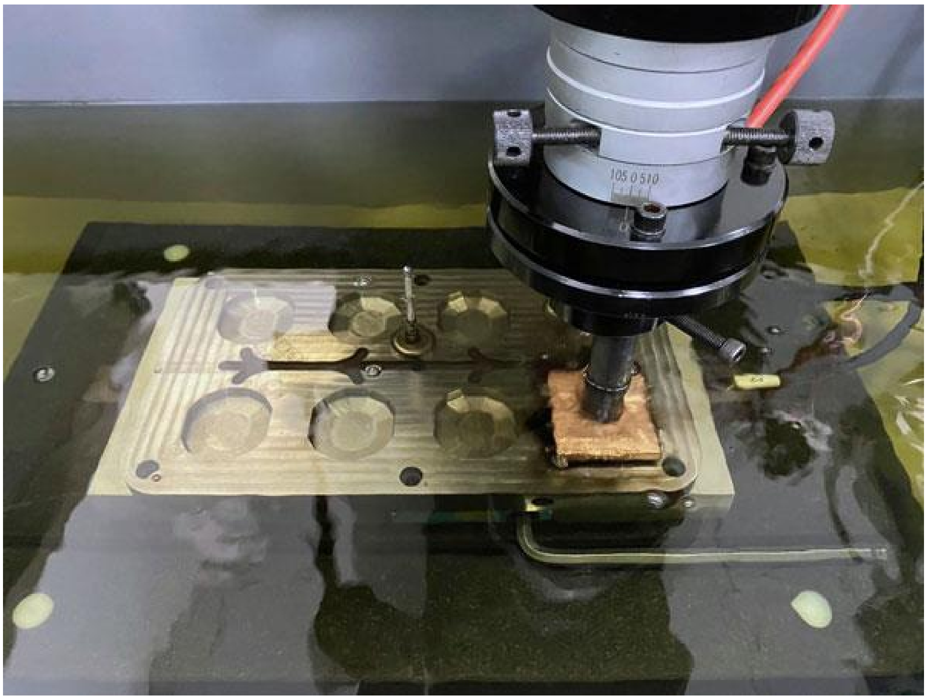

Figure 1.19. Example of Die-Sink EDM machining [27].

2. Overview on materials fatigue

In material's science, fatigue is the phenomenon which leads to components failure due to cyclic loads under material's static strength. Failure occurs when a crack, which may be pre-existing in the piece or forms later, propagates reducing piece's resistant section. Hence, a load that was not critical for the undamaged component now generates a stress in the remaining resistant section that causes failure.

The ASTM[1] (American Society for Testing and Materials International) definition of fatigue is:

"The process of progressive, localized, permanent structural change occurring in a material, subjected to conditions that produce fluctuating stresses and strains at some point or points and that may culminate in cracks or complete fracture after a sufficient number of fluctuations."

Fatigue rupture can be caused by phenomena of different nature depending on the external load that causes it:

- *Mechanical fatigue*: fatigue failure is caused by the repetitive application of mechanical loads, e.g., centrifugal force on gas turbines blades.
- *Thermomechanical fatigue*: fatigue that occurs when a component's operating temperatures are time or space-variable in concomitance with mechanical loads, e.g., blades and discs in gas turbines.

---

[1] ASTM (2000), Standard Terminology Relating to Fatigue and Fracture, vol. 03. 01 edition Testing ASTM designation E1823

- *Creep fatigue*: creep is phenomenon which arises when operating temperatures are high, e.g., turbine blades and vanes.
- *Corrosion fatigue*: fatigue caused by components oxidation due to their exposure to corrosive environment or substances, e.g., hot gas expanding in turbine.
- *Wear fatigue*: fatigue that occurs in both sliding or rolling contacts, e.g., gears.
- *Fretting fatigue*: phenomenon that arises from small sliding between bodies in contact under cyclic loads, e.g., blade-disc attachments in gas turbines [28].

2.1. Historical background

For sake of shortness, below is reported only a summary of the most important achievements in material's fatigue field even though many other researchers and achievements would deserve to be mentioned.

Fatigue is a well-known phenomenon in scientific world since the first half of 19th century. It was due to the *"Versailles Accident"* on May 5th, 1842, that fatigue became a concerning problem for the engineers of the time. Accident was caused by the locomotive front-axle failure when the train was passing near Versailles, resulting in loss of human lives. The British railway engineer W.J.M. Rankine studied several broken axles and recognized that failure was caused by initiation and growth of cracks, especially near shoulders or stress concentration zones. However, at the time the most believed theory was the so-called *"re-crystallization theory"* which related the fatigue failure to the material microstructure re-crystallization under cyclic stress. Moreover, researchers of time were more concerned in putting the fatigue phenomenon under control than understating its physical basis, so Rankine work was not considered [28],[29].

In the 1860's, German engineer A. Wöhler proposed an empirical approach for prevent fatigue failure and predict a life which would guarantee no in-service failure. He studied several railway axles in steel considering axial, torsion, and bending stresses. In his tests, Wöhler included notched and unnotched samples. The test machine designed by Wöhler for his experiments is quite like the one used today. He analysed operating conditions and measured, through a dynamometer, in-service maximum deflections which allowed him to assess in-service forces. At the end of his work, Wöhler proposed a finite life design approach also considering the scatter (probability of failure). Besides, he stated that two different safety factors were needed, one to relate the in-service maximum stress to material's static strength and one for the allowable stress amplitude. Wöhler highlighted the fact that these safety factors were reliable only for unnotched components, and that further experiments on notched components were necessary to assess their relative safety factors. In his work, he also preliminarily investigated cracks propagation, stating that radial and not-superficial cracks are the most critical. Moreover, he found that allowable stress is higher for thinner axles than thicker ones. Eventually, in his work Wöhler concluded that: materials fail under cyclic loads under its static strength; stress amplitude is the critical parameter for the failure but also the mean component of stress has an impact on life. From Wöhler's work today we have the so-called *Wöhler curves* or *S-N curves* [28],[29].

H. Gerber (1874) and J. Goodman (1899) studied the effect of mean stress in components fatigue design, their contribution then merged in *Haigh diagram* for infinite life design [28],[29].

In 1886 German engineer J. Bauschinger studied what happens to a sample when gets loaded beyond the yield strength and then re-loaded in the opposite direction (e.g., traction beyond yield strength and then compression or vice versa). He found that the new yield strength in the opposite direction is lower. This effect is called the *Bauschinger effect*, and will be used in the 1950s by Coffin and Manson for their hypothesis in low cycles fatigue estimations [28],[29].

In 1910 American O.H. Basquin proposed a linear equation for finite life region of *Wöhler curves* in log-log scale. In the same year, English aeronautical engineer L. Bairstow introduced the problem of cyclic hardening and softening of materials under cyclic loads and their hysteresis cycle [28],[29].

In the 1920's and 1930's material's fatigue became a research major field. Engineers like Scottish B.P. Haigh (1917), American D.J. McAdam (1926) and British H.J. Gough (1933) investigated the effect of corrosion on fatigue; in 1924 was introduced the first damage accumulation model by Swede engineer A.

Palmgren, then further developed by M.A. Miner in 1945 make it a useful analytical tool and establishing practical restrictions to its use. Today it is known as *Palmgren-Miner rule*. In 1924 Gough published the first book on fatigue. Here he investigated the effect of surface roughness and V-shaped notches on fatigue limit. In 1920 A.A. Griffith introduced the fracture mechanics in fatigue field [28],[29].

In 1930s Gough and Pollard first studied multiaxial fatigue, even though the first attempts were done by Tresca and von Mises between the end of 19th and the beginning of 20th century [30].

Years between 1920 and 1950 elevated Germany as the reference country in fatigue research thanks to the work of Thum, Föppl, Graf and Gassner. Graf was involved in studies relating welded and riveted joints, while Föppl worked on mechanical methods to improve fatigue characteristics (e.g., shot peening). Gassner was a pioneer in variable stress amplitude fatigue tests based on Lufthansa's and combat aircraft load spectra and gave a method to design in these conditions introducing the *8-step blocked-program*; he was also the first to understand that a higher static strength leads to a lower fatigue limit due to higher allowable (operating) stresses. Thum, with his 524 publications between 1922 and 1956, gave undoubtedly a great contribute in fatigue studies. This latter one introduced the *Gestaltfestigkeit theory*, where he established that fatigue strength is more dependent on component's shape than on material's properties. Another Thum's important finding was that the stress-concentration factor was neither a component's or material's characteristic value but had to be assessed with a specific experimental test case-by-case. Besides, Thum also worked on the effect of residual stresses, machining marks, surface hardening and prestressing on fatigue limit, corrosion fatigue, fretting, allowable stresses in the finite life region and considered several types of components (e.g. axles, shafts, bolts, gears, joints) [28],[29].

In 1927 Tomlinson coined the term *fretting corrosion* to explain the oxidation of two rotating surfaces in contact, and performed the first tests on fretting fatigue [28],[29].

In 1937 German engineer H. Neuber published a book that collected his works on the evaluation of stress concentration factor and fatigue stress concentration factor [28],[29].

American engineers L.F. Coffin and S.S. Manson (1954) laid the foundations of low cycles fatigue (LCF) field. In their work, based on Bauschinger's studies, they considered the component's fatigue behaviour when it has to withstand plastic strain amplitudes. Their results are reported in strain-number of cycles diagrams called *Coffin-Manson curves*, widely used still today in strain-based fatigue assessment of components under high temperatures and loads for few cycles, such as gas turbine discs and blades [28],[29].

In 1950s the jet aircraft de Havilland Comet reported some accidents related to fuselage failure. Causes were found in stress concentrations in rivet holes near passenger windows due to pressurization cycles. Accidents led the aeronautical normative authorities to change deeply tests to be done for aircraft certification, introducing full-scale test. Engineers began performing these tests on WW II aircraft to understand whether the theories discovered in the past decades (such as Miner rule) were reliable for the design of aircraft structures. Moreover, empirical diagrams (e.g. Haigh-Goodman diagram) were extended to aeronautical materials such as Dural. This work put the basis for the introduction of *fail-safe* design approach, a new alternative to *safe-life* one (design approaches will be discussed in the following section) [28],[29].

In 1951 the International Committee for Aeronautical Fatigue (ICAF) was founded, with the aim to gather all fatigue experts every two years for conferences, thus helping the dissemination of knowledge [28],[29].

In 1957 American G. Irwin, starting from Griffith ideas on fracture mechanics, developed the so-called *linear elastic fracture mechanics*. He stated that fatigue failure occurs when the stress-intensity factor, K, reaches a critical value, so that a static failure of the cracked sample occurs. Irwin found that critical K value was related to a parameter called *fracture toughness*. Five years later, Paris related the increment in crack size at each cycle da/dN to the range of stress-intensity factor ΔK in constant stress amplitude cycles with an linear equation in the log-log scale, known as *Paris low* [28],[29].

Thanks to the work of A.A. Wells (1961) and J.R. Rice (1968), who studied for first metals elastic-plastic behaviour, *elastic-plastic fracture mechanics was introduced*. They respectively introduced the concept of c*rack tip opening displacement* (CTOD) and *J-integral*. C.F. Shih in 1981 found out a relationship between these two parameters [31].

From the 1960's, thanks to microscopy advances, significant progress has been done. In 1956, Thompson, Wadsworth and Louat coined the term *persistent slip bands*, which are slip bands that persistently reappears in the same locations even after the removal of some material in fatigued metals. The first *fatigue striations* on fractured samples were observed, and distance between each other could be related to fatigue crack growth giving hint to new theories. Concomitantly, servo hydraulic test machines were introduced, making it possible to perform test with arbitrary amplitudes at higher frequencies. Servo hydraulic machine demonstrated that *Miner's rule* and *Gassner's blocked program* were unconservative. Nevertheless, in the following years, it was soon clear among the engineers that simulating real load spectra was a waste of time and resources, and standardized load spectra, such as *Twist*, *Falstaff* and many others were introduced [28],[29].

In 1974 United States Air Force (USAF), to explain the numerous structural failures of its fleet, introduced a new design approach, called *damage tolerant*. In the following decades, this approach was extended to commercial applications, causing huge increment in maintenance costs [28],[29].

In the 1970, German Elber's worked on the relation between the range of variation of stress intensity factor and the real history of the crack i.e. true operating cycles with variable amplitudes. His main achievement consisted in finding out that, after being loaded with a high tensile stress, crack closed before load was reduced to zero. Elber investigated the effect of a pre-existing plastic deformation on crack's growth or closure. In this decade and in the following one, researchers discovered that pre-existing plastic deformation was only of the mechanisms that could lead to crack closure. A lot of efforts were done to investigate these mechanisms [28],[29].

In the last decades, fatigue studies focused on better characterize the effect of variable amplitude loads on components life. Some attempts were done to try to represent variable amplitudes by "equivalent" constant amplitude, e.g., the *Root Mean Square (RMS) approach*. On the other hand, research focused also on corrosion, creep (high temperatures) and multiaxial fatigue [28],[29].

Regarding multiaxial fatigue, several conferences and symposia had place, and some books were written between 1980s and the first decade of new millennium [28],[29].

Kachanov (1958) first introduced a new theory, known as *Continuum Damage Mechanics (CDM)*, to evaluate damage related to creep under uniaxial stress in metals. Few years later (1969) Rabotnov worked on the same topics [33].

Since that moment, several scientist and engineers worked on the development of the theory, publishing lots of papers, monographies, and books especially in the 1980s and 1990s. The main contributes came from Chaboche (1987), Krajcinovic (1989), Voyiadjis and Kattan (2002), Lemaitre (2005) [34].

Growing interest on fatigue of ceramic, polymers and composite materials has grown since their unique properties which allow their employment under conditions that metals could not withstand. In 1990s Suresh and other researchers worked on these topics [28].

2.2. Design approaches to fatigue

As reported in section 2.1, through the years mainly three design approaches to fatigue had been developed.

2.2.1. Safe-life approach

Safe-life approach consist of assessing component maximum life before fatigue failure occurs. At the end of its (designed) life, the component is withdrawn from service and substituted by a new one, whether it was damaged or not [35],[36].

This approach makes necessary to carry out tests beforehand to verify that the component can operate without any damage for a period greater than the operational life. Due to fatigue data dispersion, an adequate scatter factor is needed, i.e. to guarantee a certain component life, in its design phase it is necessary to assure a life which has to be greater at least of a scatter factor than the one required [35],[36].

Safe-life approach leads to oversized thus heavier structures. In aeronautical field, this approach is suitable for so-called *Single Load Path* structures (e.g., landing gears, engine supports). In heavy-duty gas turbines, blades are designed following this approach since high loads and temperatures causes failure in few cycles after crack initiation [35],[36].

2.2.2. Fail-safe approach

Difficulties in predicting the life of a structure with sufficient accuracy and therefore the modest average exploitation of its operational life capabilities has led to the development of fail-safe approach to design. Fail-safe criterion is based on the principle that in case of a component failure, structure must guarantee enough structural and functional integrity to accomplish the mission despite failure [35],[36].

Fail-safe methodology involves the hyper static behaviour (redundancy) of the structures to which it is applied and requires periodic inspections which allow cracked components to be repaired or substituted. Good design in this sense also implies attention to detail to avoid the onset of cracks and structural solutions that limit their propagation (crack stoppers). It must be demonstrated that is always guaranteed a residual resistance capacity of the structure to withstand the operating conditions in the presence of damage. This approach is applied in so-called *multiple load path* structures [35],[36].

A correct inspection plan is fundamental, both for the inspection intervals and for the level of accuracy of the inspection to identify the first damage. From this perspective, the fail-safe philosophy has strong repercussions on the definition of the maintenance program and consequently on the operating costs. In design phase it has to be considered that fail-safe designed structures or components must be reached and checked while mounted quite easily by maintainers [35],[36].

2.2.3. Damage tolerant approach

Damage tolerant philosophy assumes the presence of an initial defect in every critical component whose failure can cause the loss of the whole structure. Defect size is assumed to be the greatest one that can't be detected with non-destructive testing (NDT), e.g., x-rays, ultrasonic tests, penetrant liquids [35],[36].

The main issue is providing an inspection plan accurate enough that these initial defects don't become critical before they are detected. To ensure it, designers have to evaluate two connected aspects: damage growth under cyclic loads form the initial size to the critical one and damage critical size which causes static failure under operating loads. This information is available to engineers thanks to *fracture mechanics* [35],[36].

Essentially, damage tolerant approach is the evolution of fail-safe criterion. While fail-safe is based mainly on the assumption that a crack can be detected before it reaches the critical size, damage tolerant employs fracture mechanics to understand when an initial damage reaches the critical size. The critical size depends on the operating loads that the component should withstand [35],[36].

Damage tolerance is a property and can be defined as the ability of the structure to accomplish its function in the presence of damage for a period of time long enough to detect them [35],[36].

The main aspect of damage tolerant design is concept of periodical inspection and therefore the definition of an inspection and maintenance plan [35],[36].

The best materials for this philosophy are those ones that are characterized by high fracture toughness and by a slow, stable crack growth (*slow crack growth* concept). A key role is covered by NDT [35],[36].

2.3. Fatigue estimation approaches

Fatigue can be divided in two main categories depending on the magnitude of number of cycles leading to failure:

- *High cycles fatigue (HCF)*: this type of fatigue is characterized by high frequency low amplitude loads causing elastic deformations. We talk about HCF when number of cycles exceeds 10^4. HCF approaches are based on stress variations. Examples of HCF is fatigue caused by flutter vibration in gas-turbine blades.
- *Low cycles fatigue (LCF)*: fatigue that occurs under low frequency high amplitude variable loads causing plastic deformations. We talk about LCF when the number of cycles doesn't exceed 10^4. LCF approaches are based on strain variations. An example of such loads is the centrifugal force acting on turbine blades during start-up and shut down cycle of the engine [31].

2.3.1. Stress-based approach

Wöhler curves, also named *S-N curves*, are the most widely used for HCF evaluations.

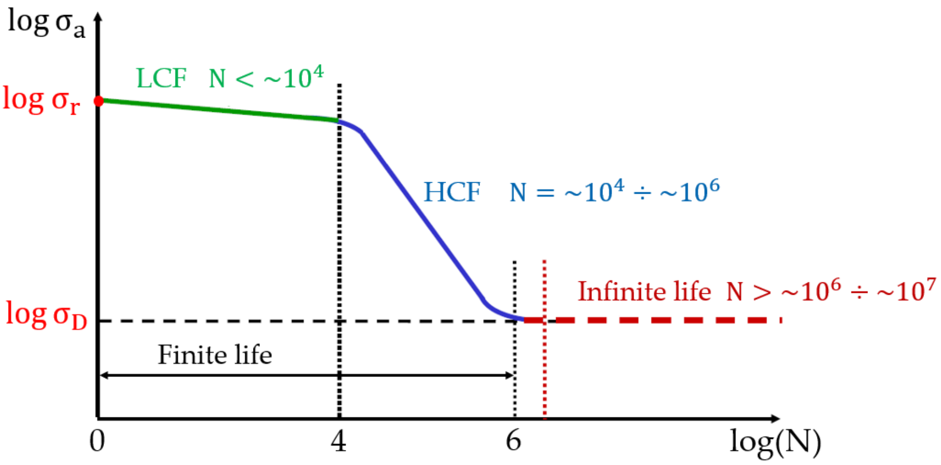

Figure 2.1. S-N diagram divided into fatigue life regions. The graph is in the log-log scale [37].

In Figure 2.1, σ_a is the stress amplitude of the axial load; σ_D is material's fatigue strength while σ_r is material's static strength. N is the number of cycles.

The HCF region can be well-approximated by an exponential equation – which in the log-log scale is a line – given by Basquin:

$$\sigma_a^k \cdot N = C \tag{2.1}$$

The parameters k and C are constants and has to be determined by Wöhler diagram. Eq. 2.1 can be used to estimate fatigue life by knowing stress amplitude and the values of k and C [37].

Wöhler curves are obtained via experimental tests and are characteristics of each material. Once fixed the stress amplitude, a significant number of samples (ASTM states twelve) are brought to their fatigue limit and the normal distribution of collected data is calculated. This is repeated for a range of stress amplitude between σ_D and σ_r [37].

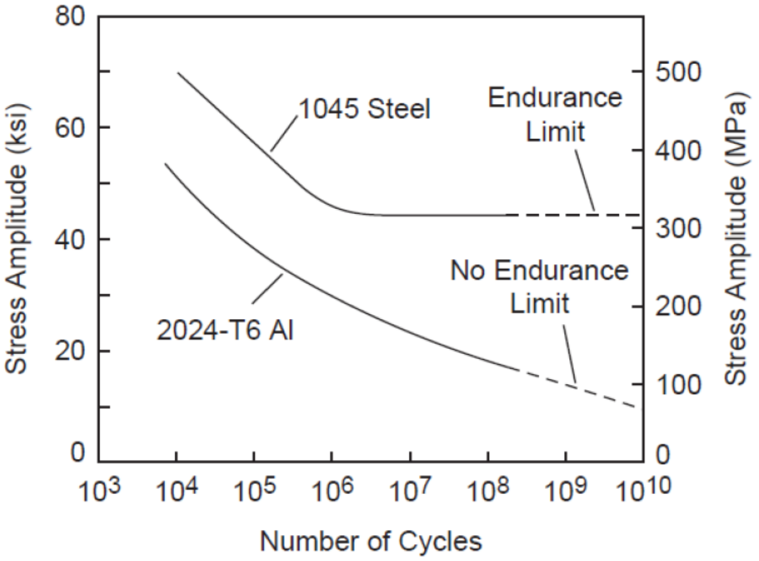

Figure 2.2. Comparison of S-N curves for 1045 steel alloy and 2024 aluminium alloy [38].

Figure above shows that, typically, steel alloys have a well-visible *endurance limit* (defined by the "knee" of the curve), while aluminium alloys doesn't. Some titanium alloys behave like steel alloys, whereas other non-ferrous alloys, like copper alloys and magnesium alloys behave like aluminium alloys. The endurance limit – also called fatigue strength or fatigue limit – is a limit below which there is no failure due to fatigue. Conventionally, for those alloys that doesn't show a proper endurance limit, it is defined a number of cycles beyond which fatigue life can be considered infinite, usually $10^6 \div 10^7$ cycles [37].

2.3.1.1. Effect of mean stress

S-N curves are obtained from experimental tests where the mean stress is equal to zero. The effect of the mean stress on number of cycles can be evaluated through *Haigh diagram* [37].

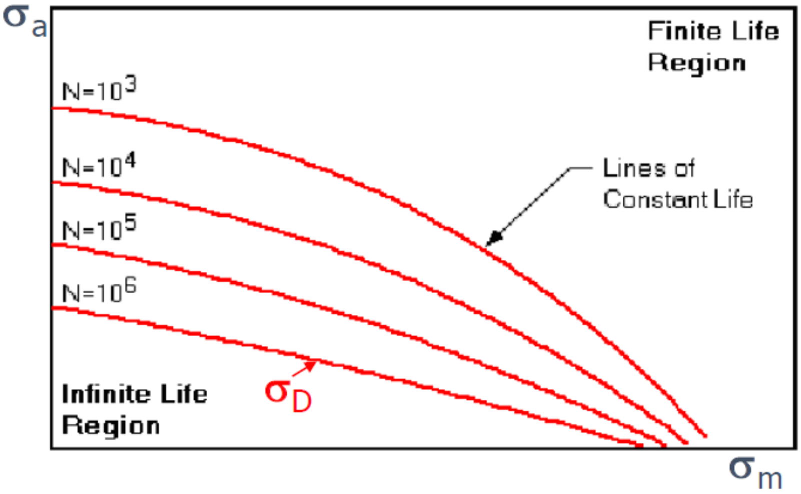

Figure 2.3. Haigh diagram. The x-axis reports the mean stress, the y-axis reports the stress amplitude [37].

Red curves in **Figure 2.3** are lines of constant life. The one at 10^6 cycles represents the boundary between finite (over the curve) and infinite (below the curve) life region; moreover, this curve reports the information about the fatigue limit for different values of the mean stress σ_m [37].

To evaluate the effect of the mean stress it is possible to reconduct the load cycle to an equivalent one with zero mean stress and the same fatigue life:

$$\sigma_{ar} = \frac{\sigma_a}{1 - \frac{\sigma_m}{\sigma_r}} \tag{2.2}$$

where σ_{ar} is the equivalent amplitude with zero mean stress that leads to the same fatigue life [37].

2.3.2. Strain based approach

This approach is used for LCF estimations. As written before, LCF is characterized by elastic-plastic strain hence it is necessary to consider cyclic hardening or softening of materials under cyclic loads, and $\sigma - \varepsilon$ monotonic curve has to be replaced and a new curve, called *cyclic curve* (see Appendix C.1), is introduced [31].

The typical $\varepsilon - N$ curve is called *Coffin-Manson curve,* whose equation is:

$$\varepsilon_{at} = \varepsilon_{ae} + \varepsilon_{ap} = \frac{\sigma_f'}{E}\left(2N_f\right)^b + \varepsilon_f'\left(2N_f\right)^c \tag{2.3}$$

For more details on the mathematical steps to obtain eq. 2.3 see Appendix C.2.

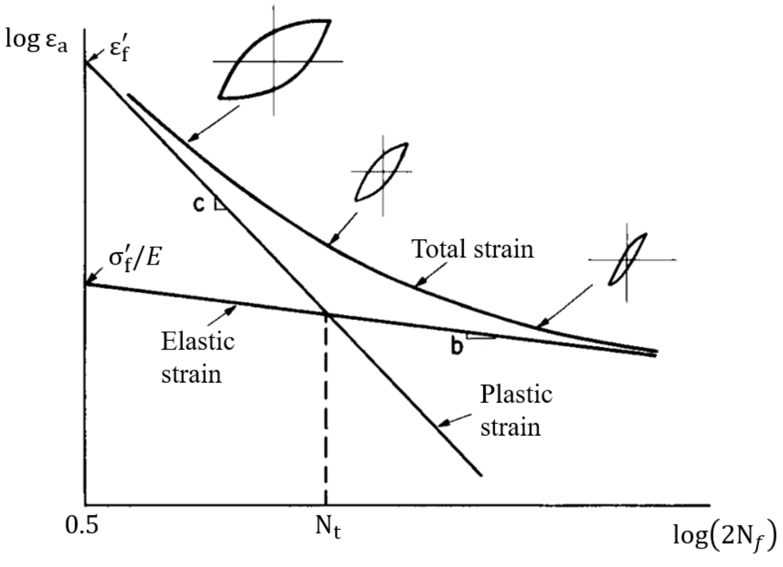

Figure 2.4. Coffin-Manson curve [31].

In **Figure 2.4** it can be observed that in short fatigue lives plastic strains are prevailing and the hysteresis loop is wide. Conversely, in long fatigue lives elastic strains are dominant and the hysteresis loop is thin. The crossing point of the elastic and plastic lines can be seen as the transition between low cycle fatigue and high cycle fatigue. In fact, N_t is called *fatigue transition life* and a typical value is 1000 [31].

The parameters b, c, ε_f' and σ_f' are material's characteristic constants. Conventionally, ε_f' and σ_f' are determined when $N_f = 0{,}5$. In absence of more precise information, these two parameters can be assumed equal to static rupture stress and strain values. The b exponent ranges from -0,05 to -0,12, while c exponent varies from -0,5 to -0,8 typically [31].

2.3.2.1. Effect of mean stress

Like the S-N curves, discussed in section 2.3.1, also the Coffin-Manson curves are usually obtained with zero mean stress. While in the stress-based approach it was rather easy to introduce the effect of the mean stress (see eq. 2.2), in the strain-based approach it is not so easy because in imposed deformation tests with large strain amplitudes mean stress relaxes cycle by cycle (*cycle dependent relaxation*) [31].

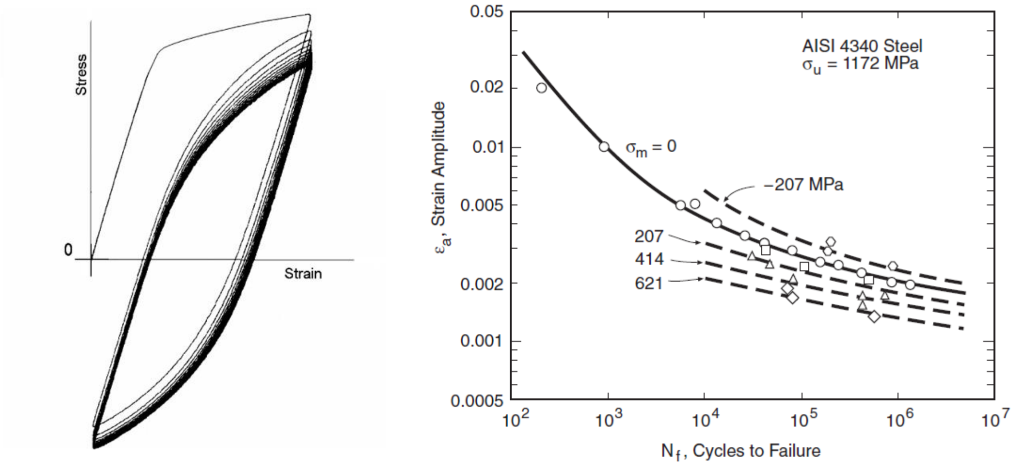

(**a**) (**b**)

Figure 2.5. (**a**) illustration of cycle dependent relaxation [39]; (**b**) effect of mean stress in strain-number of cycle diagram [31].

As **Figure 2.5b** shows, mean stress reduces fatigue life [31].

There are mainly three approaches to this problem: *Morrow* approach, *modified Morrow* approach and *Smith, Watson and Topper* approach [31].

(i) Morrow approach

J. Morrow made suitable eq. 2.2 for ε-N curves:

$$\sigma_{ar} = \frac{\sigma_a}{1 - \frac{\sigma_m}{\sigma_f'}} \tag{2.4}$$

where σ_{ar} is the equivalent stress amplitude that produces the same fatigue life as the combination of σ_a and σ_m [31].

It can be defined a *Morrow parameter* as $\left(1 - \frac{\sigma_m}{\sigma_f'}\right)^{\frac{1}{b}}$, that has to be introduced in the Coffin-Manson curve equation:

$$\varepsilon_{at} = \frac{\sigma_f'}{E}\left(1-\frac{\sigma_m}{\sigma_f'}\right)\left(2N_f\right)^b + \varepsilon_f'\left(1-\frac{\sigma_m}{\sigma_f'}\right)^{\frac{c}{b}}\left(2N_f\right)^c \tag{2.5}$$

In conclusion, Morrow approach follows this procedure: given a certain strain amplitude and the Coffin-Manson curve, first evaluate N^* by graphical way, then evaluate N_f by eq. C.9 (see Appendix C.3) [31].

The entire mathematical procedure is reported in Appendix C.3.

(ii) Modified Morrow approach

Morrow approach overestimates the effect of the mean stress because it doesn't consider mean stress relaxation. To consider this effect, eq. 2.5 has been modified as follow:

$$\varepsilon_{at} = \frac{\sigma_f'}{E}\left(1-\frac{\sigma_m}{\sigma_f'}\right)\left(2N_f\right)^b + \varepsilon_f'\left(2N_f\right)^c \tag{2.6}$$

where the Morrow parameter has been removed from the plastic strain component given that, under large strain amplitudes, mean stress has no effect on plastic deformations. The graphical resolution is not suitable for this approach [31].

(iii) Smith, Watson and Topper (SWT) approach

The maximum stress is defined:

$$\sigma_{max} = \sigma_m + \sigma_a \tag{2.7}$$

and then it is assumed that $\sigma_{max} \cdot \varepsilon_a$ to be constant. Hence, the relationship between the zero mean stress load cycle, i.e. $\sigma_{max} = \sigma_{ar}$ and $\varepsilon_a = \varepsilon_{ar}$, and the generical load cycle with $\sigma_m \neq 0$ is:

$$\sigma_{max} \cdot \varepsilon_a = \sigma_{ar} \cdot \varepsilon_{ar} \tag{2.8}$$

and then, by substituting eq. C.4 (see appendix C.3) and eq. 2.3 in eq. 2.8 [31]:

$$\sigma_{max} \cdot \varepsilon_a = \sigma_f'\left(2N_f\right)^b \cdot \left[\frac{\sigma_f'}{E}\left(2N_f\right)^b + \varepsilon_f'\left(2N_f\right)^c\right] \tag{2.9}$$

3. Component description and CAD model

The component selected for this study is a free-standing turbine blade and its correspondent disc sector. Its fir-tree attachment consists of a 3 lobes geometry whereas the airfoil is cooled through radial channels.

The blade and disc materials are a Nickel-based superalloy and a martensitic steel respectively.

The surfaces which get in contact with the disc when the turbine is working are called active planes. The fir-tree "branches" are called lobes. The part which connects the attachment to the airfoil is called shank. Component geometry above shank consists of a platform and an airfoil. This part is considered only as mass and its centrifugal force contribute has been applied on top surface of the shank (see **Figure 1.5**).

A set of parameters has been selected for this thesis work, all related to a 2D study model.

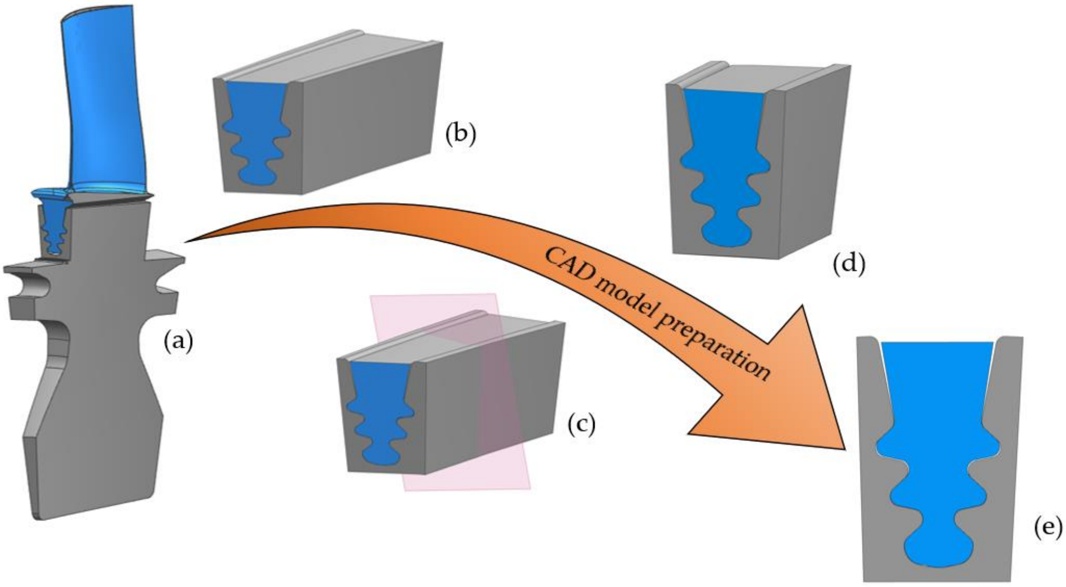

Figure 3.1. (**a**) 3D CAD model with the entire blade and its disc sector; (**b**) fir-tree and disc groove 3D sub-model; (**c**) details of the cutting plane; (**d**) cutted 3D portion; (**e**) 2D final CAD model.

Furthermore, the 2D section has been built from 3D CAD model of the component cutting the blade fir-tree and disc groove with a plane normal to blade-disc mounting direction.

The angle between the horizontal direction and the lobe 1 active plane is called α_1. In the same way, the inclination respectively of the second and third lobe are called α_2 and α_3. The offset between the active planes of the first lobe and the second lobe is called L_1. In the same way, L_2 is the offset between the active planes of the first lobe and the third lobe.

All these definitions and parameters are reported in the following pictures.

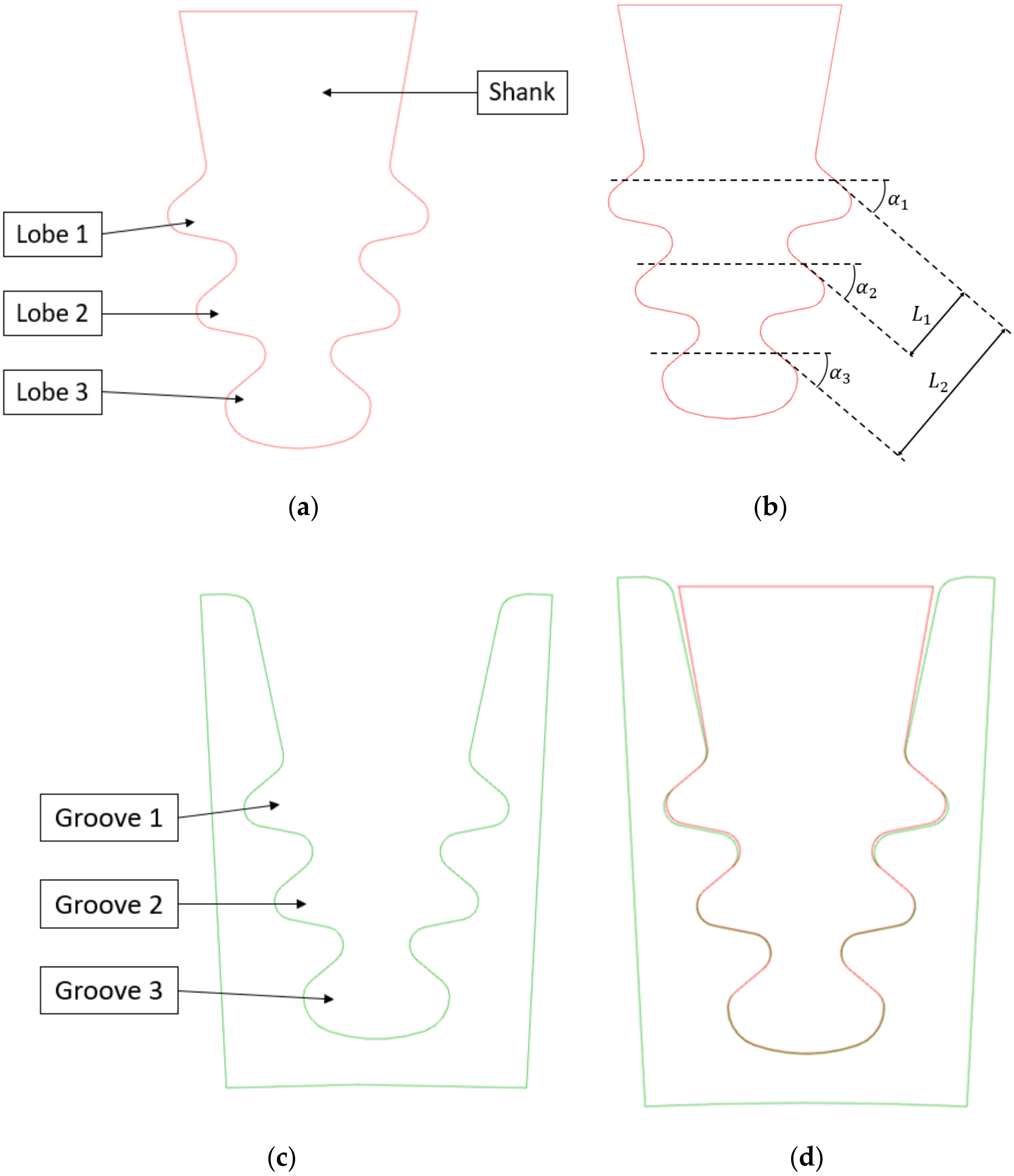
Shank
Lobe 1
Lobe 2
Lobe 3
α_1
α_2
α_3
L_1
L_2
Groove 1
Groove 2
Groove 3

(**a**) (**b**)

(**c**) (**d**)

Figure 3.2. (**a**) Blade fir-tree attachment definitions; (**b**) parameters considered in the analysis; (**c**) Disc groove definition; (**d**) Coupling between blade's attachment and disc groove.

4. Statistical analysis on out of tolerance (machining process)

To investigate which parameters were more affected by non-compliances, a statistical analysis has been carried out. Some parameters such as planarity involves 3D effects which are not considered in this study, so they are not kept into consideration.

During a standard machining qualification process for the blade fir-tree attachment, several data have been collected from post-process measurements and used as statistical starting point for this work. Machining process experience imposes the tolerance upper and lower limits: for a given process, the OEM knows the machine maximum precisions and establishes tolerance range.

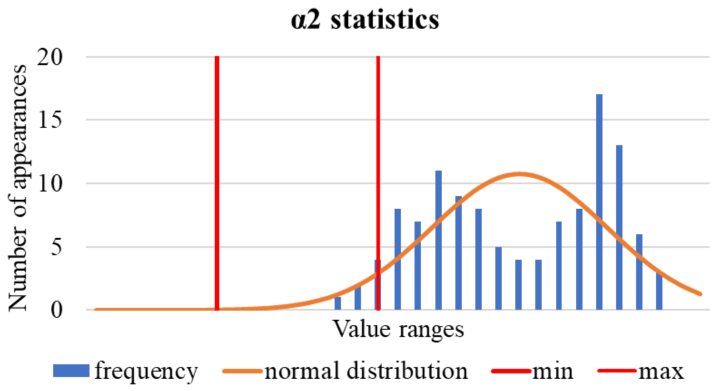

(a)

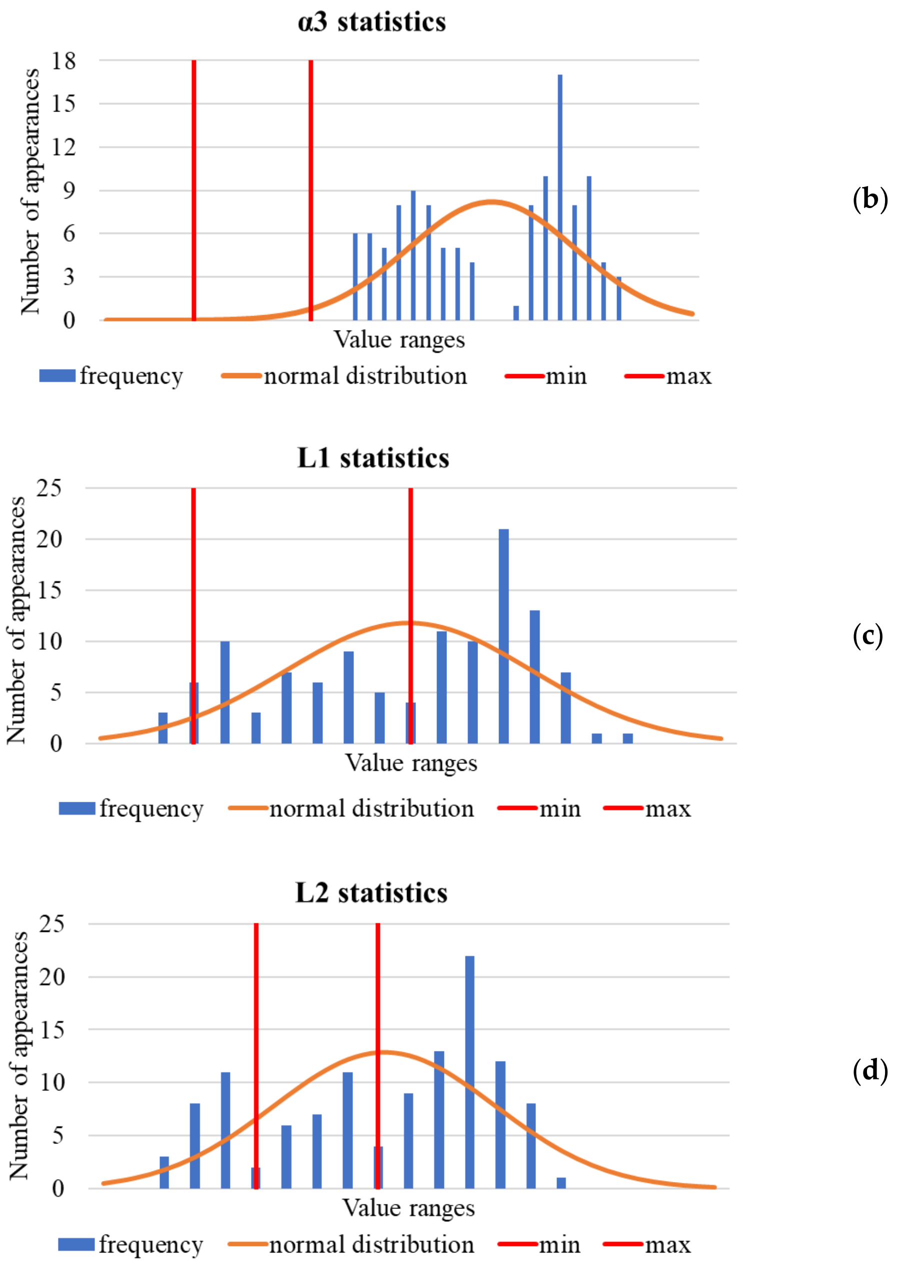

Figure 4.1. (**a**) α_2 measurements statistical distribution; (**b**) α_3 measurements statistical distribution; (**c**) L_1 measurements statistical distribution; (**d**) L_2 measurements statistical distribution.

The two vertical red lines represents the tolerance upper (on the right, *max* voice of the legend) and lower limits (on the left, *min* voice of the legend). The orange curve is the normal distribution curve. The parameter variation range has been divided into sub-ranges. The blue bars represent the number of occurrences within a certain sub-range.

5. Fatigue life assessment tools

Fatigue life estimations were performed using two AEN analytical in-house tools.

5.1. In-house tool for blade fir-tree attachment LCF assessment

AEN tool for blade attachment life estimation requires as input a text file containing the results of an elastic calculation.

In **Figure 5.1** is reported a scheme which shows a generic procedure for LCF assessment. Starting from FEA results, the procedure involves the use of Neuber's hyperbola (see appendix A), Ramberg-Osgood (see appendix B) and Coffin-Manson curves (see section 2.3.2) and applies Morrow correction (see section 2.3.2.1) to obtain the number of cycles before crack initiation [31].

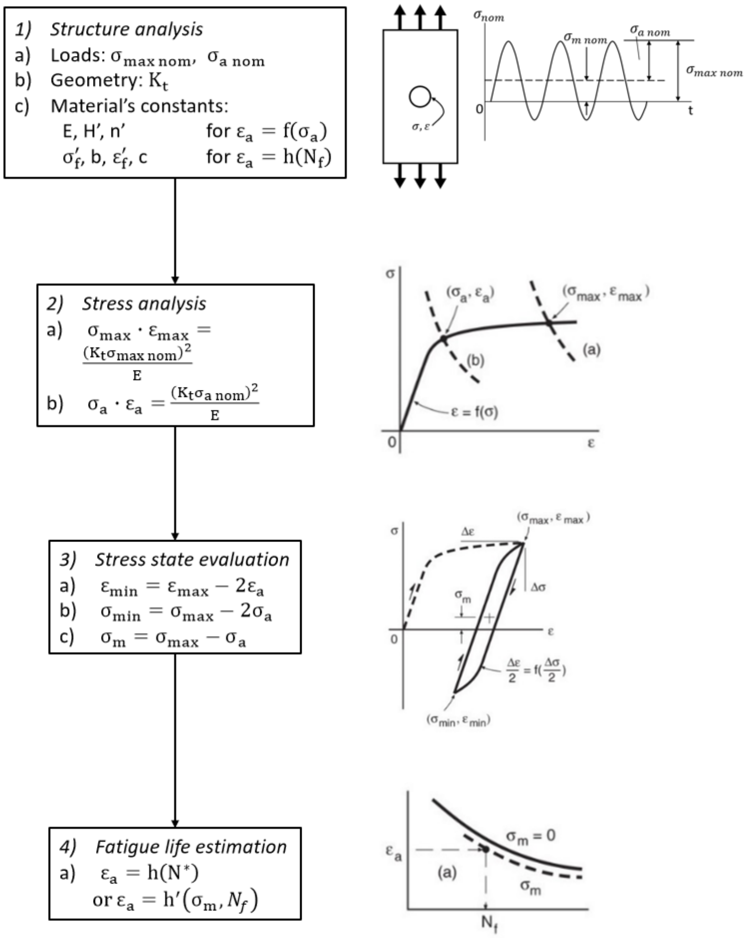
1) Structure analysis
a) Loads: σmax nom, σa nom
b) Geometry: Kt
c) Material's constants:
E, H', n' for εa = f(σa)
σ'f, b, ε'f, c for εa = h(Nf)
σnom
σm nom
σa nom
σmax nom
0
t
σ, ε
2) Stress analysis
a) σmax · εmax = (Ktσmax nom)²/E
b) σa · εa = (Ktσa nom)²/E
σ
(σa, εa)
(σmax, εmax)
(b)
(a)
ε = f(σ)
0
ε
3) Stress state evaluation
a) εmin = εmax − 2εa
b) σmin = σmax − 2σa
c) σm = σmax − σa
(σmax, εmax)
Δε
Δσ
σm
Δε/2 = f(Δσ/2)
(σmin, εmin)
4) Fatigue life estimation
a) εa = h(N*)
or εa = h'(σm, Nf)
εa
σm = 0
(a)
σm
Nf

Figure 5.1. Example of a possible procedure for a generic blade fir-tree attachment LCF evaluation [31].

5.2. In-house tool for rotor disc LCF assessment

AEN tool for disc groove life estimation requires as input a file containing the results of an elastic-plastic calculation

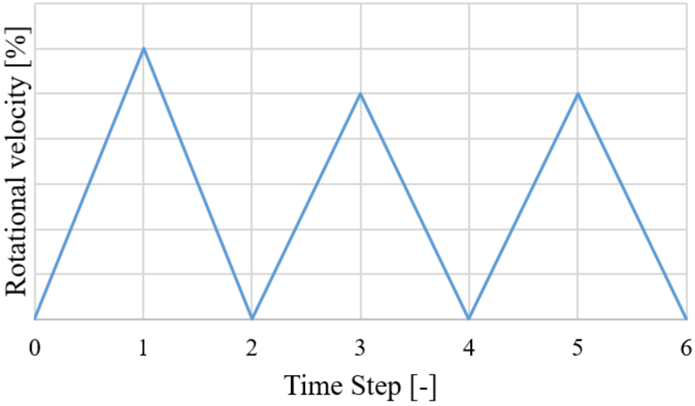

Figure 5.2. Stabilized load cycle.

It implements a *critical plane approach* to multiaxial fatigue. Critical plane approach searches for a plane where stresses and strains are the most severe and uses those values to estimate fatigue life. More details are reported in [40].

The tool workflow is reported in **Figure 5.3**.

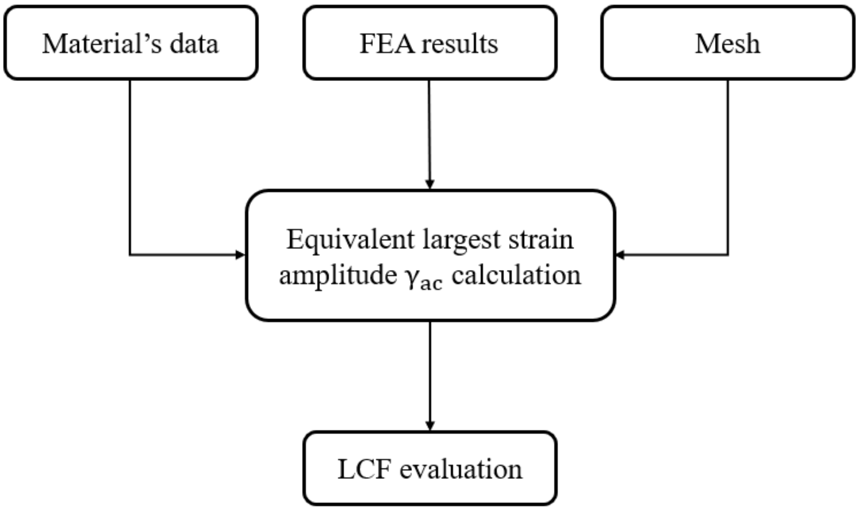
Material's data
FEA results
Mesh
Equivalent largest strain amplitude γ_{ac} calculation
LCF evaluation

Figure 5.3. Tool for disc groove LCF assessment workflow.

5.3. Stress gradient approach

A local approach to blade fir-tree attachment lifing, applied by AEN in-house tool, can be overconservative, considering that very localized stress concentrations can occur. To keep this aspect into consideration also a non-local approach based on stress gradient [41][42] has been investigated.

Stress gradient approach is based on experimental tests on notched samples which provide several S-N curves parameterized by temperature and stress gradient value. For each case are reported design and mean curve. A non-dimensional example is reported in **Figure 5.4**.

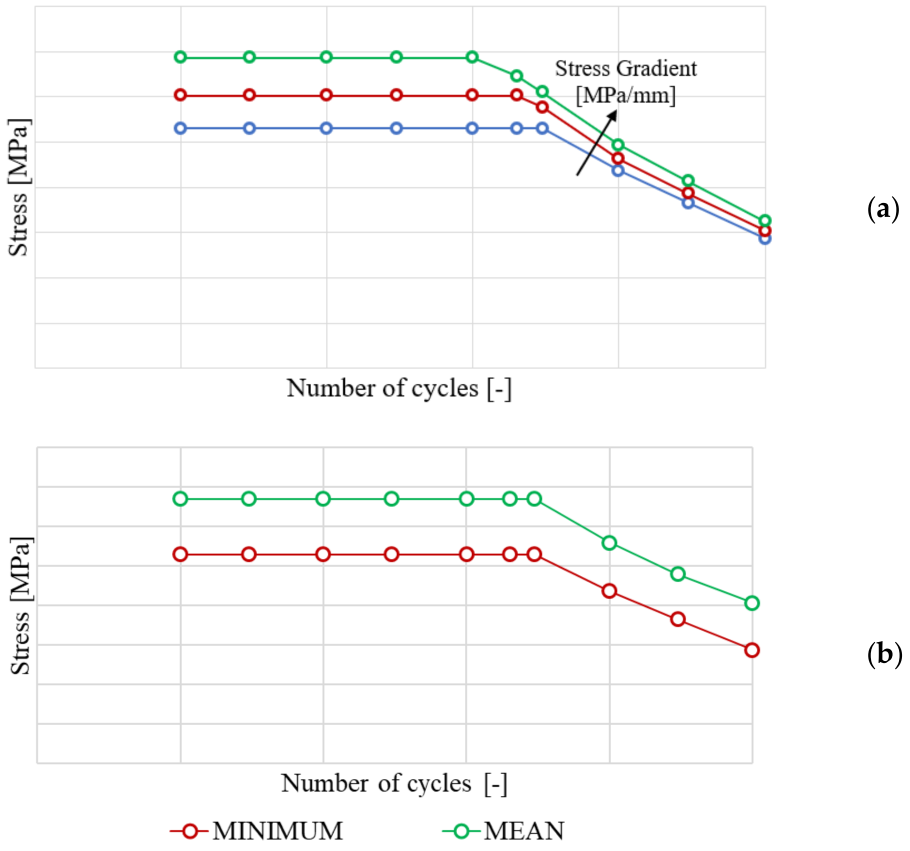

Figure 5.4. (**a**) S-N curves parameterized by stress gradient; (**b**) comparison between minimum (design) and mean curves.

Furthermore, an example of stress gradient application is reported in **Figure 5.5**.

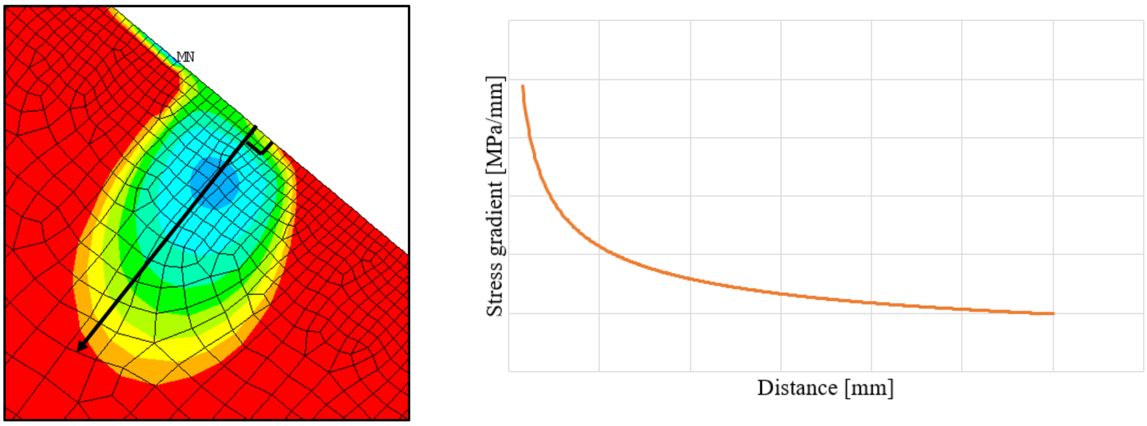

(**a**) (**b**)

Figure 5.5. (**a**) LCF contours and stress gradient direction (black arrow); (**b**) stress gradient trend with respect to distance.

6. Tests matrix definition

Considering five parameters there are $2^5 - 1$ possible combinations. Each parameter alone can assume four possible values i.e., nominal, upper tolerance, lower tolerance, and out-of-tolerance value (except from the angle α_1 which has no out-of-tolerances).

Table 6.1. Considered values for each parameter.

Parameter	Nominal	Upper tolerance	Lower tolerance	Out-of-tolerance maximum value
$\boldsymbol{\alpha_1}$	Yes	Yes	Yes	No
$\boldsymbol{\alpha_2}$	Yes	Yes	Yes	Yes
$\boldsymbol{\alpha_3}$	Yes	Yes	Yes	Yes
$\boldsymbol{L_1}$	Yes	Yes	Yes	Yes
$\boldsymbol{L_2}$	Yes	Yes	Yes	Yes

All possible combinations are too much, thus only a few of them – the most representative – have been considered. Test cases are reported in **Table 6.2**.

All these case studies have been compared with the nominal condition to evaluate their lifing impact.

For sake of briefness, in the following sections upper tolerance limit value is abbreviated with *toll up*, lower tolerance limit value is abbreviated with *toll low* and out-of-tolerance maximum value is abbreviated with *max*.

Table 6.2. Case studies.

Test	α_1	α_2	α_3	L_1	L_2
1	nominal	nominal	nominal	nominal	nominal
2	upper tolerance	nominal	nominal	nominal	nominal
3	lower tolerance	nominal	nominal	nominal	nominal
4	nominal	upper tolerance	nominal	nominal	nominal
5	nominal	lower tolerance	nominal	nominal	nominal
6	nominal	out-of-tolerance	nominal	nominal	nominal
7	nominal	nominal	upper tolerance	nominal	nominal
8	nominal	nominal	lower tolerance	nominal	nominal
9	nominal	nominal	out-of-tolerance	nominal	nominal
10	upper tolerance	upper tolerance	nominal	nominal	nominal
11	lower tolerance	lower tolerance	nominal	nominal	nominal
12	upper tolerance	nominal	upper tolerance	nominal	nominal
13	lower tolerance	nominal	lower tolerance	nominal	nominal
14	nominal	upper tolerance	upper tolerance	nominal	nominal
15	nominal	lower tolerance	lower tolerance	nominal	nominal
16	nominal	out-of-tolerance	out-of-tolerance	nominal	nominal
17	upper tolerance	upper tolerance	upper tolerance	nominal	nominal
18	lower tolerance	lower tolerance	lower tolerance	nominal	nominal
19	nominal	nominal	nominal	upper tolerance	nominal
20	nominal	nominal	nominal	lower tolerance	nominal
21	nominal	nominal	nominal	out-of-tolerance	nominal
22	nominal	nominal	nominal	nominal	upper tolerance

23	nominal	nominal	nominal	nominal	lower tolerance
24	nominal	nominal	nominal	nominal	out-of-tolerance
25	nominal	nominal	nominal	upper tolerance	upper tolerance
26	nominal	nominal	nominal	lower tolerance	lower tolerance
27	nominal	nominal	nominal	out-of-tolerance	out-of-tolerance
28	upper tolerance	upper tolerance	upper tolerance	upper tolerance	upper tolerance
29	lower tolerance	lower tolerance	lower tolerance	lower tolerance	lower tolerance
30	nominal	out-of-tolerance	out-of-tolerance	out-of-tolerance	out-of-tolerance

7. Parameters modification

All the out-of-tolerance CAD models were prepared to ensure that a single parameter modification would not affect others, so that each effect could be studied alone. Combinations of these parameters were also studied with the same criteria: the modification of two or more of them didn't affect the unmodified ones.

Angles were modified rotating around the mid-point of the active planes. Offset were modified translating the mid-points of the active planes.

Models were prepared in *Siemens NX software*.

7.1. Angles modification

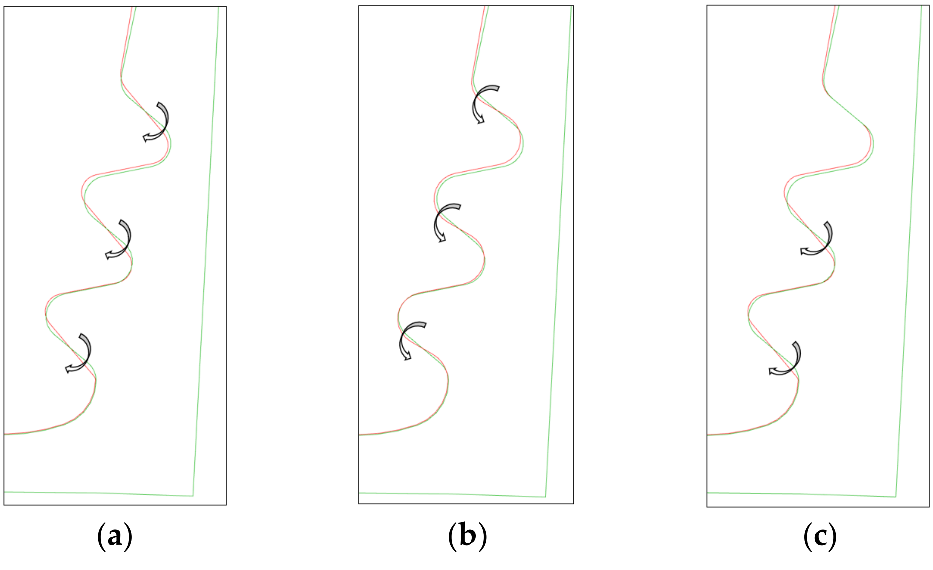
(**a**) (**b**) (**c**)

Figure 7.1. (**a**) Rotation of active planes for angles upper tolerance limit cases; (**b**) rotation of active planes for angles lower tolerance limit cases; (**c**) Rotation of active planes for angles out-of-tolerance cases.

7.2. Offsets modifications

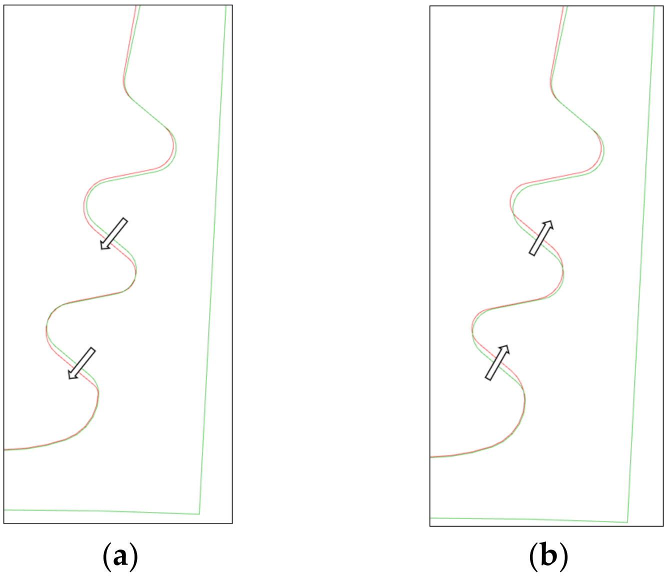
(a) (b)

Figure 7.2. (**a**) Translation of active planes for offsets upper tolerance and out-of-tolerance cases; (**b**) Translation of active planes for offsets lower tolerance limit cases.

7.3. Angles and offsets modification

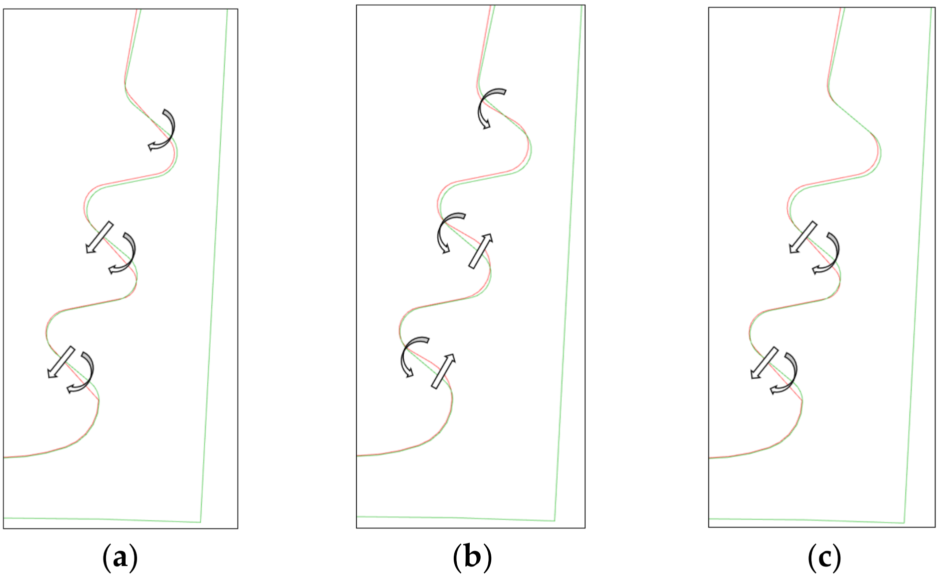
(a) (b) (c)

Figure 7.3. (**a**) angles and offsets upper tolerance limit cases; (**b**) angles and offsets lower tolerance limit cases; (**c**) angles and offsets out-of-tolerance cases.

8. FE model preparation

FE model was developed in *ANSYS Workbench 19.2* and *ANSYS Mechanical APDL 19.2*.

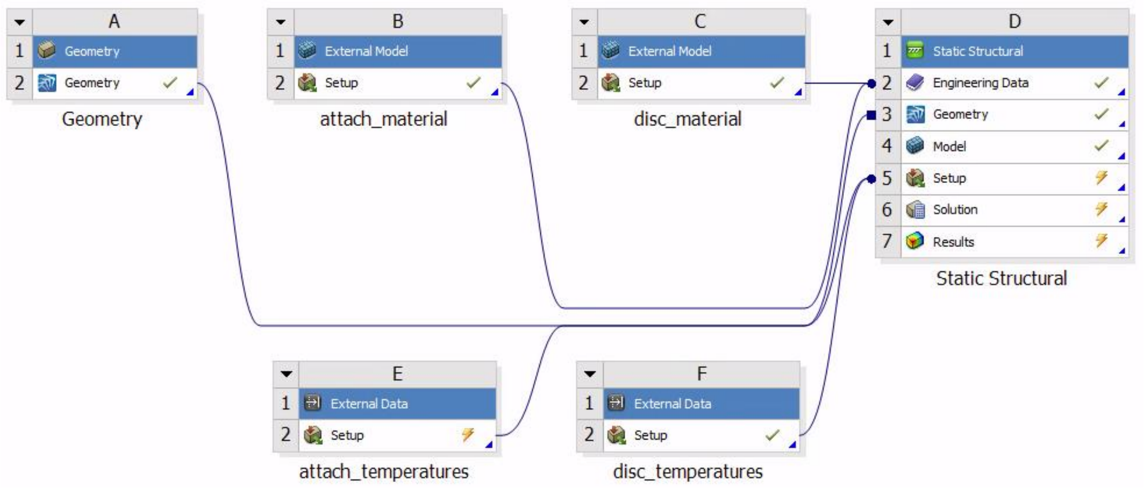
A
1 Geometry
2 Geometry
Geometry
B
1 External Model
2 Setup
attach_material
C
1 External Model
2 Setup
disc_material
D
1 Static Structural
2 Engineering Data
3 Geometry
4 Model
5 Setup
6 Solution
7 Results
Static Structural
E
1 External Data
2 Setup
attach_temperatures
F
1 External Data
2 Setup
disc_temperatures

Figure 8.1. FE model from *ANSYS Workbench 19.2*.

Performed analysis is 2D *Static Structural* (block D). Materials model (block B and C) and operating temperatures (block E and F) were imported in block D and assigned to correspondent bodies. Always in block D were selected the contact edges and were generated the mesh. Geometry CAD was imported in *ANSYS Spaceclaim* (block A).

The 2D selected approximation is *Generalized Plane strain* considering a constant (but different from zero) strain along the axial direction to enable thermal expansion. If *Plane Strain* approximation is set, deformation along the axial direction is assumed to be zero, thus thermal expansion is prevented and axial stresses are very high, leading to not reliable results.

2D elements used for blade attachment and disc groove were 8-nodes *PLANE183*, while contact elements were 1D 3-nodes *CONTA172* and target elements were 1D 3-nodes *TARGE169*.

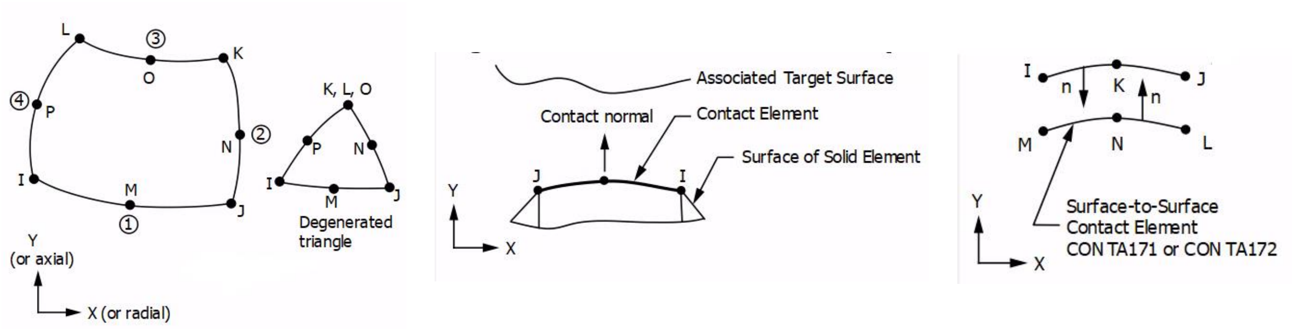
L
③
K
O
④
P
N
②
I
M
J
①
K, L, O
P
N
I
M
J
Degenerated triangle
Y (or axial)
X (or radial)
Associated Target Surface
Contact normal
Contact Element
Surface of Solid Element
J
I
Y
X
I
n
K
n
J
M
N
L
Surface-to-Surface Contact Element CONTA171 or CONTA172
Y
X

(**a**) (**b**) (**c**)

Figure 8.2. Mesh elements [43]. (**a**) PLANE183; (**b**) CONTA172; (**c**) TARGE169.

Figure 8.3 shows used coordinate systems respect to 2D model. The cylindrical one has x-axis as radial direction, y-axis as tangential direction and z-axis as axial direction. This latter one is equal to the global cartesian coordinate system. Z-axis is emerging from the plane of the sheet for both coordinate systems.

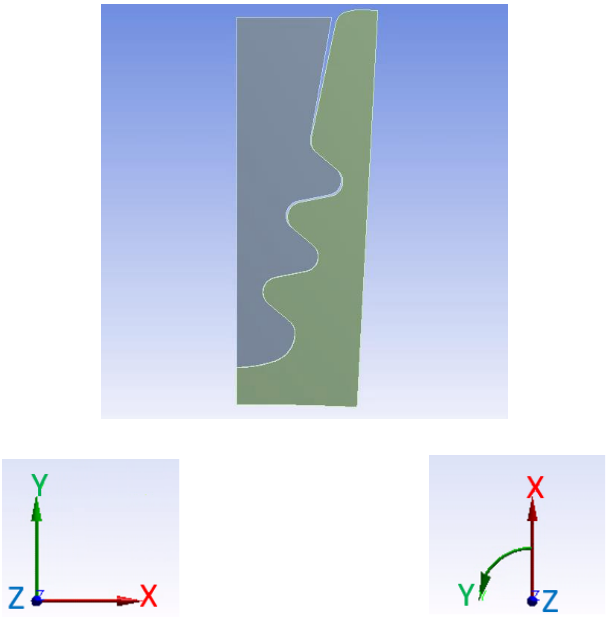

(**a**) (**b**)

Figure 8.3. (**a**) Global cartesian coordinate system; (**b**) cyclindrical coordinate system.

8.1. Boundary conditions

From a 3D FEA analysis of the component, performed by AEN blade, mechanical and thermal boundary conditions were extracted in terms of nodal temperature and disc displacement respectively.

8.1.1. Lower cut section

In the disc lower section, radial displacements have been imposed considering both mechanical and thermal loads. In **Figure 8.4** is reported the distribution of radial displacements on the lower section. An average value from the middle of the section was taken as reference.

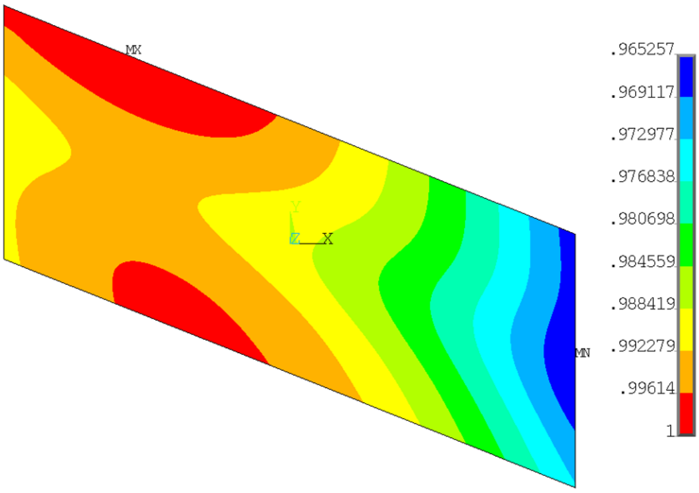

Figure 8.4. Radial displacement at lower cut section from 3D FEA results. Contour values are normalized by maximum radial displacement.

8.1.2. Upper cut section

The centrifugal force to be applied in the top part of the blade root was evaluated considering the removed mass over the cut section and its centre of gravity, at the operating rotational velocity. Then, to check that the centrifugal force was correct it was integrated the radial stress distribution in **Figure 8.5a** to estimate the total centrifugal force, and then the obtained value has been divided by blade attachment length to find the uniform distributed centrifugal load on the considered section. Blade internal cooling channels are neglected.

Also bending effect are neglected considering that the blade's centre of gravity position is designed to balance the effects related to the pressures of the hot gas on the airfoil in base load condition. **Figure 8.5**a shows radial stress distribution of a FEA where the only centrifugal force has been considered, it is notable that it is not symmetric. **Figure 8.5**b instead reports the same results in base load conditions: now the distribution is much more symmetric, for the reason just explained (keeps into account the pressures of the hot gas).

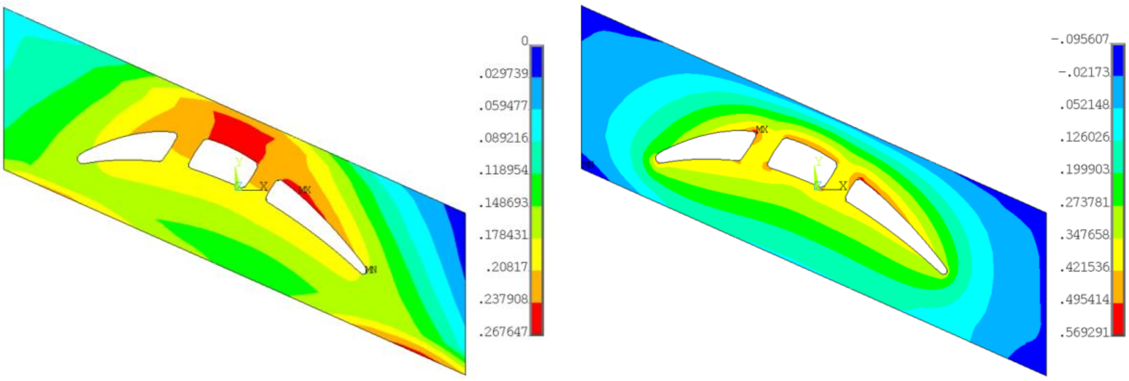

(**a**) (**b**)

Figure 8.5. Radial stress at upper cut section from 3D FEA results. Contour values are normalized by a reference value. (**a**) mechanical analysis; (**b**) thermomechanical analysis.

8.1.3. Lateral boundary conditions

As it can be seen in **Figure 3.2**, the model is symmetric, so only half part of the model has been used for analyses. At the symmetry section, zero circumferential displacement has been imposed for both blade and disc. The same for the disc lateral cut on the right side.

All boundary conditions are shown in **Figure 8.6**.

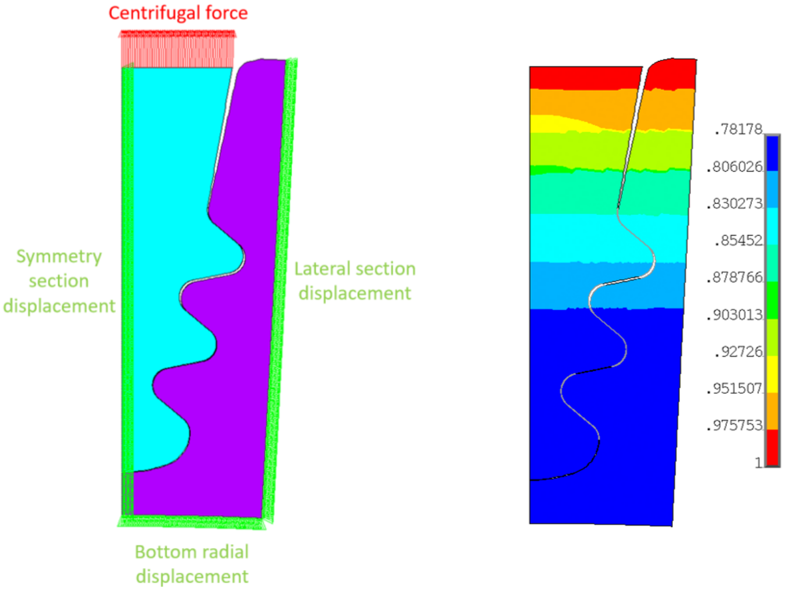
Centrifugal force
Symmetry section displacement
Lateral section displacement
Bottom radial displacement
.78178
.806026
.830273
.85452
.878766
.903013
.92726
.951507
.975753
1

(**a**) (**b**)

Figure 8.6. (**a**) mechanical boundary conditions; (**b**) body temperatures normalized by maximum temperature.

Operating body temperatures have been extracted from 3D FEA. Rotational velocity is not reported in the images, it is directed along axial direction and its value is 3000 rpm.

8.2. Contact setting

To achieve reliable results, contact settings was a critical phase. First, considering that the contact could have extended beyond the flat segment of the active plane, the adjacent curved lines were also added to the contact edges.

ANSYS Pair Based Contact Manager allowed us to manage these options:

- *Contact algorithm*: set to *Augmented Lagrange Method*.
- *Normal penalty stiffness factor*: influences contact and target relative penetration, the higher is the factor, the lower is the penetration [43]. Trail values were 0.05, 0.1, 0.2, 0.5, 0.7, 1, 1.2, 1.5, 2. **Figure 8.7** reports the effect of the factor on contact maximum pressure. This factor was set to 1.

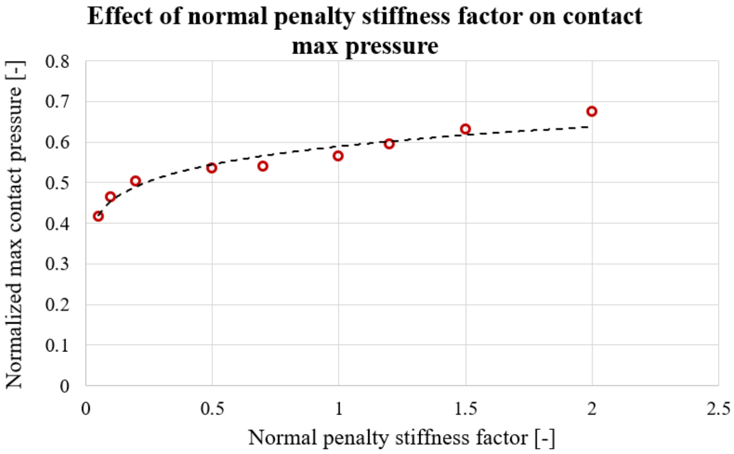

Figure 8.7. Effect of normal penalty stiffness factor on maximum contact pressure obtained with elastic calculation. Pressures are normalized by a reference value.

- *Contact detection*: there were four possibilities. The first one is contact detection at *Gauss points*, while in the last three contact detection is on nodes and are: *on nodes - normal to target, on nodes - normal from contact* and *surface projection method*. The first one has contact normal perpendicular to target surface; the second one has contact normal perpendicular to contact surface and finally in the latter one the contact detection remains at contact nodes but contact occurs on an overlapping region of the contact and target surfaces and penetration/gap is averaged on the overlapping region [43]. Contact detection was finally set at Gauss points.
- *Initial penetration*: possible options were *included* or *exclude everything*. Include everything option was set to keep into consideration possible gaps or penetrations.
- *Friction coefficient*: analyses were performed considering 0.01, 0.1, 0.2, 0.3, 0.4. The selected value was 0.2. **Figure 8.8** shows that it is a good compromise, moreover this is a common value used in industrial application.

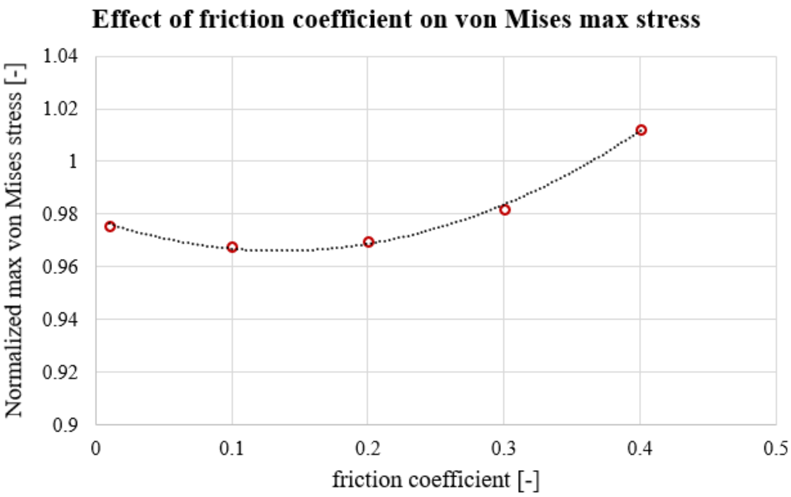

Figure 8.8. Effect of friction coefficient on von Mises maximum stress obtained with elastic-plastic calculation. Values of stress are normalized with material's yield stress.

- *Automated contact adjustment*: options were *no automated adjustment, close gap, reduce penetration, close gap/reduce penetrations,* and *default ICONT*. Close gap/reduce penetration option was chosen because helps the analysis convergence trying to reset gaps or penetration at the analysis first step.

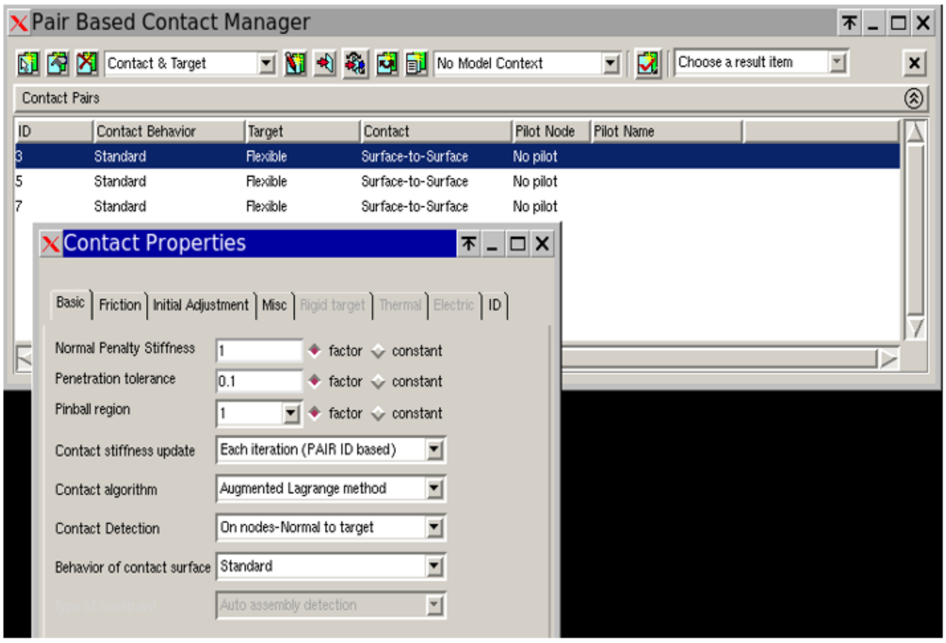
Pair Based Contact Manager
Contact & Target
No Model Context
Choose a result item
Contact Pairs
Contact Properties
Basic
Friction
Initial Adjustment
Misc
Rigid target
Thermal
Electric
ID

ID	Contact Behavior	Target	Contact	Pilot Node	Pilot Name
3	Standard	Flexible	Surface-to-Surface	No pilot	
5	Standard	Flexible	Surface-to-Surface	No pilot	
7	Standard	Flexible	Surface-to-Surface	No pilot	

Normal Penalty Stiffness: 1 ● factor ○ constant
Penetration tolerance: 0.1 ● factor ○ constant
Pinball region: 1 ● factor ○ constant
Contact stiffness update: Each iteration (PAIR ID based)
Contact algorithm: Augmented Lagrange method
Contact Detection: On nodes-Normal to target
Behavior of contact surface: Standard
Auto assembly detection

Figure 8.9. *ANSYS Pair Based Contact Manager*. Image is taken from *ANSYS Mechanical APDL 19.2*.

The following element *CONTA172* key-options have been modified:

- *Behaviour of contact surface* (key-option twelve): there were two possibilities, *standard* or *rough*, and it was set to standard.

- *Sliding behaviour* (key-option eighteen): possible options were *small* or *finite sliding*. Because of very little size elements behaviour was set to finite sliding to assure analysis convergence.

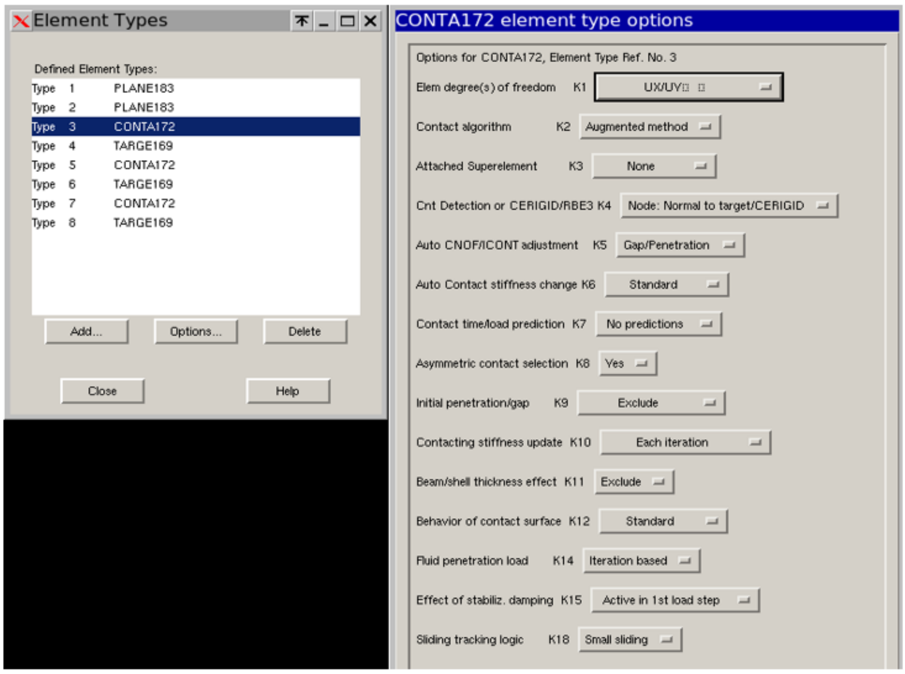

Defined Element Types:
Type 1 PLANE183
Type 2 PLANE183
Type 3 CONTA172
Type 4 TARGE169
Type 5 CONTA172
Type 6 TARGE169
Type 7 CONTA172
Type 8 TARGE169

Options for CONTA172, Element Type Ref. No. 3
Elem degree(s) of freedom K1 UX/UY
Contact algorithm K2 Augmented method
Attached Superelement K3 None
Cnt Detection or CERIGID/RBE3 K4 Node: Normal to target/CERIGID
Auto CNOF/ICONT adjustment K5 Gap/Penetration
Auto Contact stiffness change K6 Standard
Contact time/load prediction K7 No predictions
Asymmetric contact selection K8 Yes
Initial penetration/gap K9 Exclude
Contacting stiffness update K10 Each iteration
Beam/shell thickness effect K11 Exclude
Behavior of contact surface K12 Standard
Fluid penetration load K14 Iteration based
Effect of stabiliz. damping K15 Active in 1st load step
Sliding tracking logic K18 Small sliding

Figure 8.10. *CONTA172* key-options. Image is taken from *ANSYS Mechanical APDL 19.2*.

9. Mesh refinement process

Mesh refinement process was carried out to achieve mesh-independent results. **Table 9.1** reports trial mesh size.

Table 9.1. Mesh refinement tests.

Mesh name	Number of nodes	Blade surface element size [mm]	Disc surface element size [mm]	Blade contacts edges element size [mm]
70k	70203	0,5	0,5	0,5
270k	276696	0,25	0,25	0,25
43k	43384	1	1	0,2
79k	78557	1	1	0,1
125k	125334	1	1	0,06
240k	241340	1	1	0,03
355k	354821	1	1	0,02
693k	692708	1	1	0,01
1350k	1350673	1	1	0,005

An important aspect to underline is that 2D approach was fundamental in achieving such refinement level. It would have been computationally out of question to perform 3D FEA including the whole blade and the correspondent disc sector with these element size. Also, the symmetric assumption was important to further reduce element size.

Considering an equal zoom of the first lobe and groove, it is possible to graphically compare element size mesh by mesh:

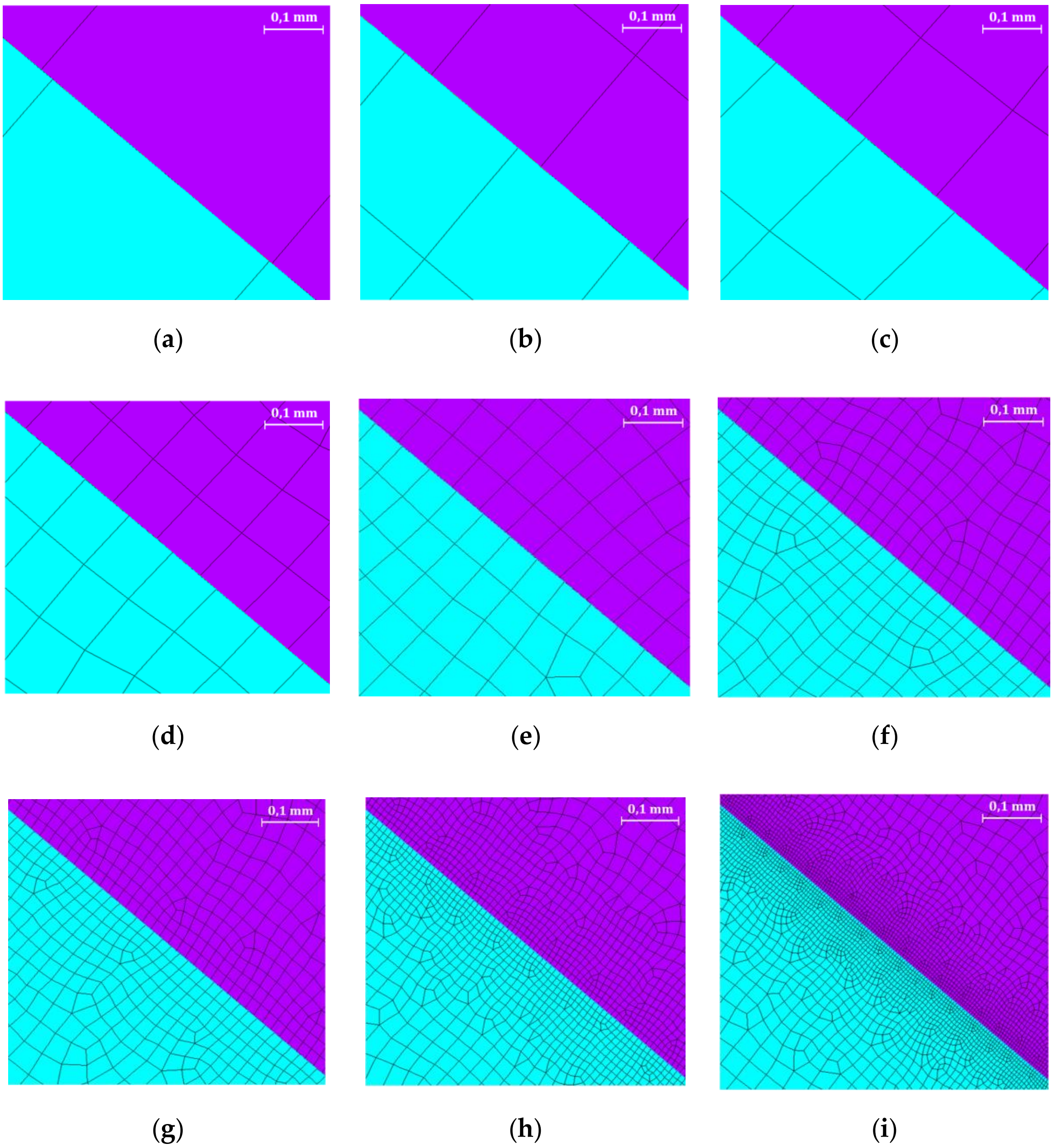
0,1 mm
0,1 mm
0,1 mm
(a)
(b)
(c)
0,1 mm
0,1 mm
0,1 mm
(d)
(e)
(f)
0,1 mm
0,1 mm
0,1 mm
(g)
(h)
(i)

Figure 9.1. Mesh size comparison. Contact size is (**a**) 0,5 mm; (**b**) 0,25 mm; (**c**) 0,2 mm; (**d**) 0,1 mm; (**e**) 0,06 mm; (**f**) 0,03 mm; (**g**) 0,02 mm; (**h**) 0,01 mm; (**i**) 0,005 mm.

To provide an example, in **Figure 9.2** is reported the contour distribution of the main results for the most refined mesh (see **Figure 9.1i**). Distribution of contours in the other cases is similar, only the peak values are different.

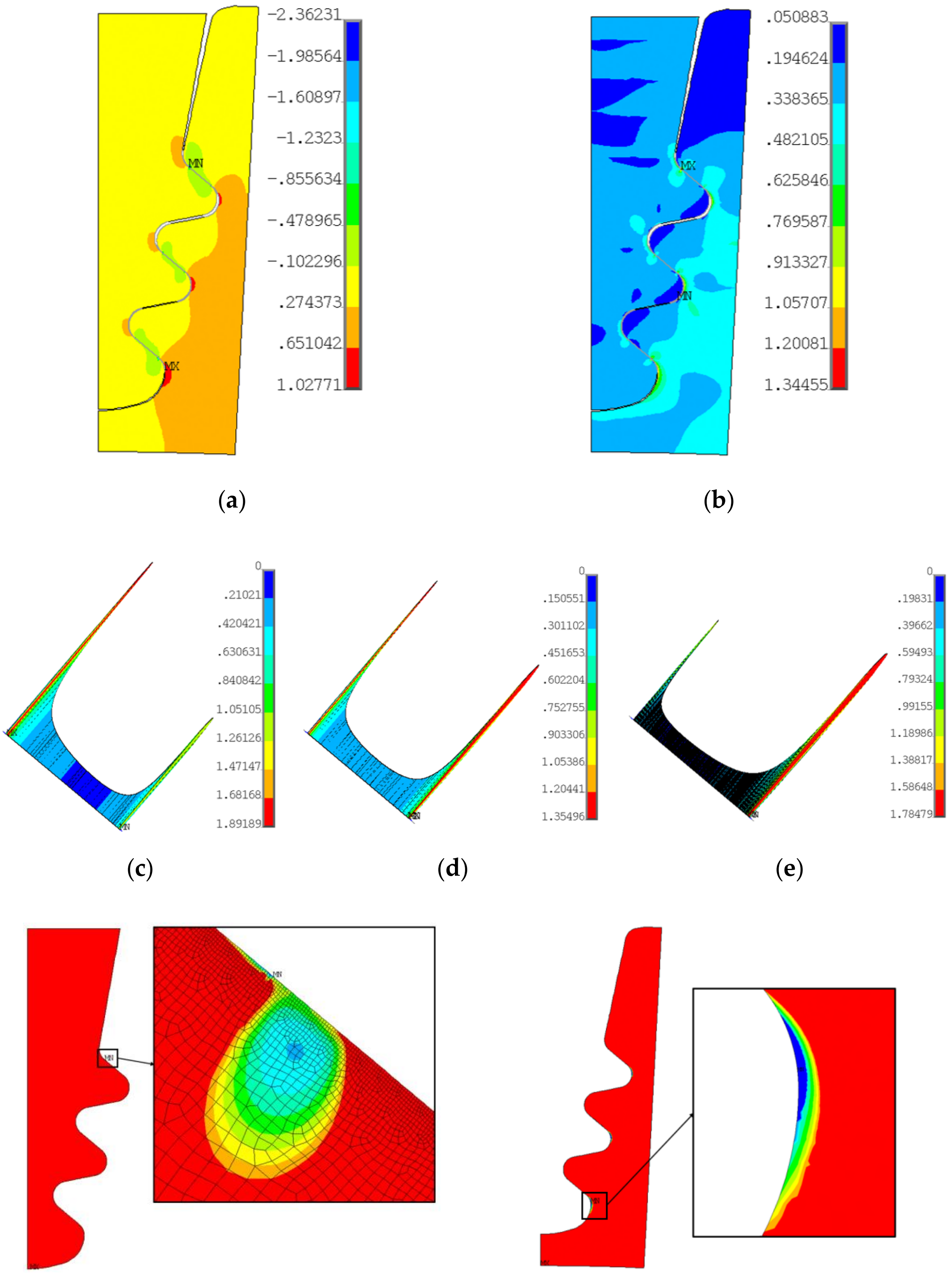
-2.36231
-1.98564
-1.60897
-1.2323
-.855634
-.478965
-.102296
.274373
.651042
1.02771
MN
MX
.050883
.194624
.338365
.482105
.625846
.769587
.913327
1.05707
1.20081
1.34455
MX
MN
0
.21021
.420421
.630631
.840842
1.05105
1.26126
1.47147
1.68168
1.89189
0
.150551
.301102
.451653
.602204
.752755
.903306
1.05386
1.20441
1.35496
0
.19831
.39662
.59493
.79324
.99155
1.18986
1.38817
1.58648
1.78479
MN
MN

(a) (b)

(c) (d) (e)

(f) (g)

Figure 9.2. (**a**) Radial stress contours; (**b**) von Mises stress contours; (**c**) contact pressure on lobe 1; (**d**) contact pressure on lobe 2; (**e**) contact pressure on lobe 3;
(**f**) blade LCF contours; (**g**) disc LCF contours.

Stresses and contact pressure are normalized by blade's material yield strength. Talking of results in absolute terms, disc groove reported both the radial stress peak values, while blade's attachment reported the maximum von Mises stress.

Figure 9.2f shows LCF evaluations regarding blade attachment. The minimum number of cycles in the little blue region in depth was taken as reference for comparisons. The minimum value – *MN* in the picture – reported by the software was considered unreliable given that in such position there is the transition from contact – non-contact.

9.1. Stress comparison

9.1.1. Blade fir-tree attachment results

Table 9.2. Blade attachment stresses. Values are normalized by a reference one.

Mesh	Maximum radial stress [-]	Minimum radial stress [-]	Maximum von Mises stress [-]
70k	0,681	-1,211	0,927
270k	0,689	-1,604	1,069
43k	0,693	-1,878	1,169
79k	0,688	-1,723	1,357
125k	0,693	-2,217	1,382
240k	0,692	-2,154	1,342
355k	0,695	-2,171	1,340
693k	0,693	-2,189	1,340
1350k	0,693	-2,206	1,345

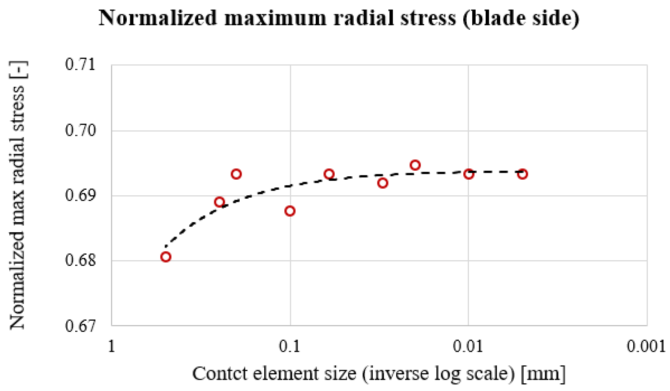

(a)

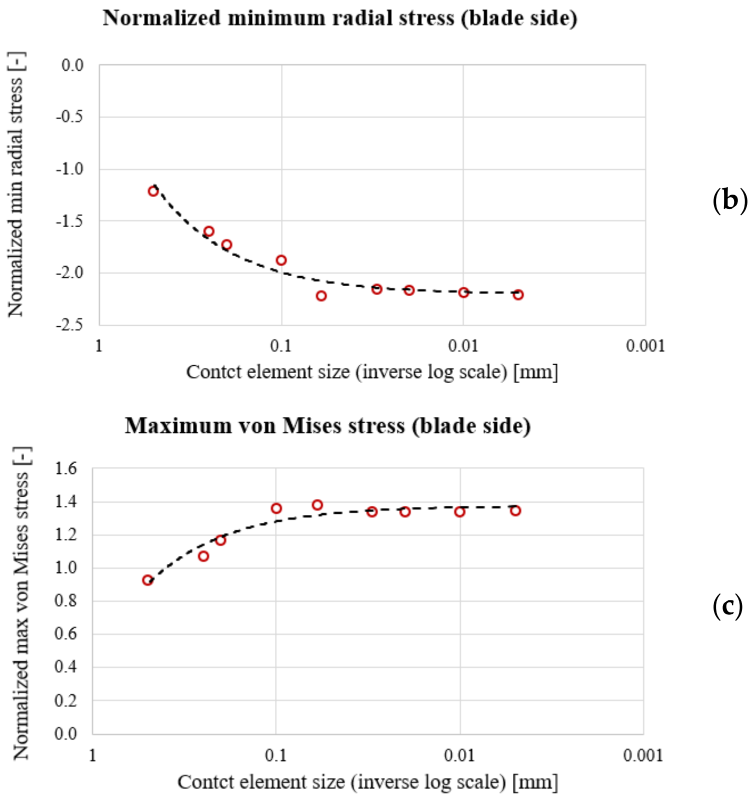

Figure 9.3. (**a**) maximum radial stress trend with respect to contact element size; (**b**) minimum radial stress trend with respect to contact element size; (**c**) maximum von Mises stress trend with respect to contact element size.

Results reported in **Table 9.2** and in **Figure 9.3** shows that mesh refinement process led to mesh-independent results, given that for the most fine meshes the results are almost the same.

9.1.2. Disc groove results

Table 9.3. Disc groove stresses. Values are normalized by a reference one.

Mesh	Maximum radial stress [-]	Minimum radial stress [-]	Maximum von Mises stress [-]
70k	0,934	-1,358	0,852
270k	0,932	-1,537	1,047
43k	0,935	-1,598	1,142
79k	0,935	-1,962	1,214
125k	0,936	-2,032	1,240
240k	0,936	-2,091	1,176
355k	0,936	-2,093	1,170
693k	0,936	-2,106	1,173
1350k	0,936	-2,152	1,177

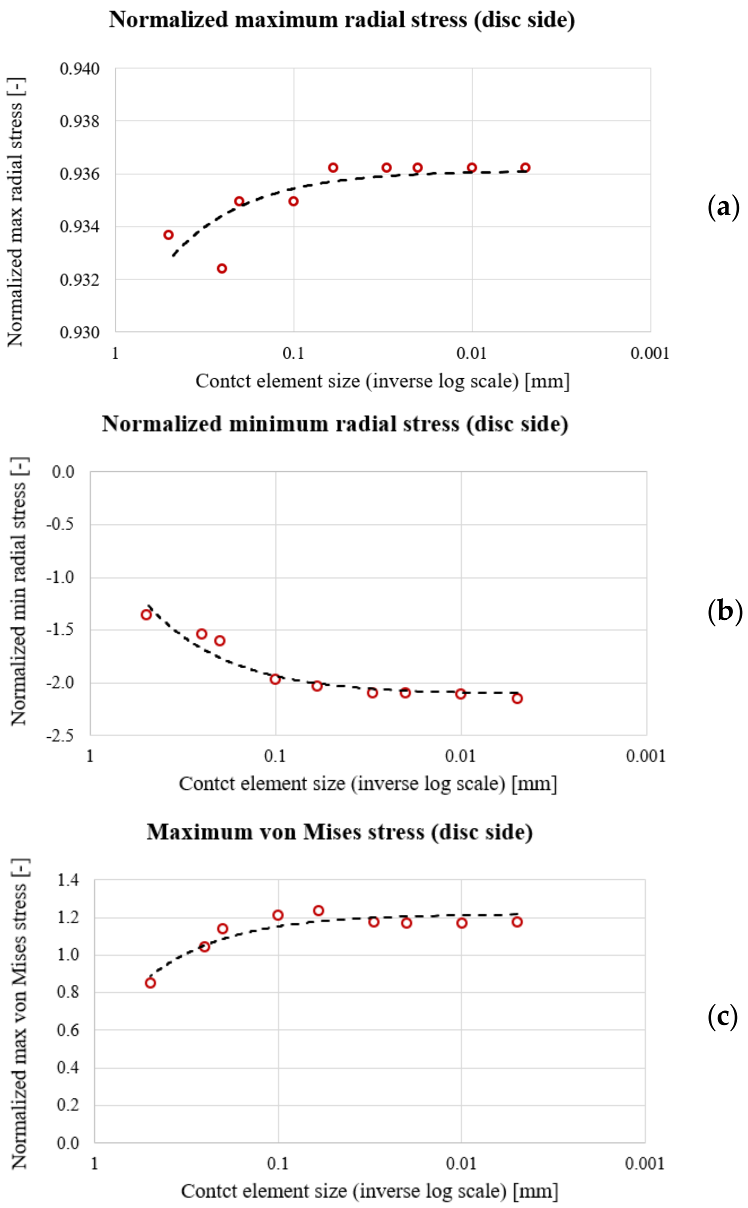

Figure 9.4. (**a**) maximum radial stress trend with respect to contact element size; (**b**) minimum radial stress trend with respect to contact element size; (**c**) maximum von Mises stress trend with respect to contact element size.

The same considerations written for the blade attachment results in the preceding section can be applied those ones of the disc groove.

9.2. Contact pressure comparison

Table 9.4. Peak contact pressures comparison. Values are normalized by a reference one.

Mesh	Peak contact pressure on lobe 1 [-]	Peak contact pressure on lobe 2 [-]	Peak contact pressure on lobe 3 [-]
70k	1,104	0,608	0,894
270k	1,160	0,875	1,356
43k	1,245	1,029	1,571
79k	1,667	1,167	1,557
125k	1,758	1,241	1,685
240k	1,840	1,300	1,741
355k	1,859	1,329	1,756
693k	1,874	1,353	1,779
1350k	1,892	1,354	1,784

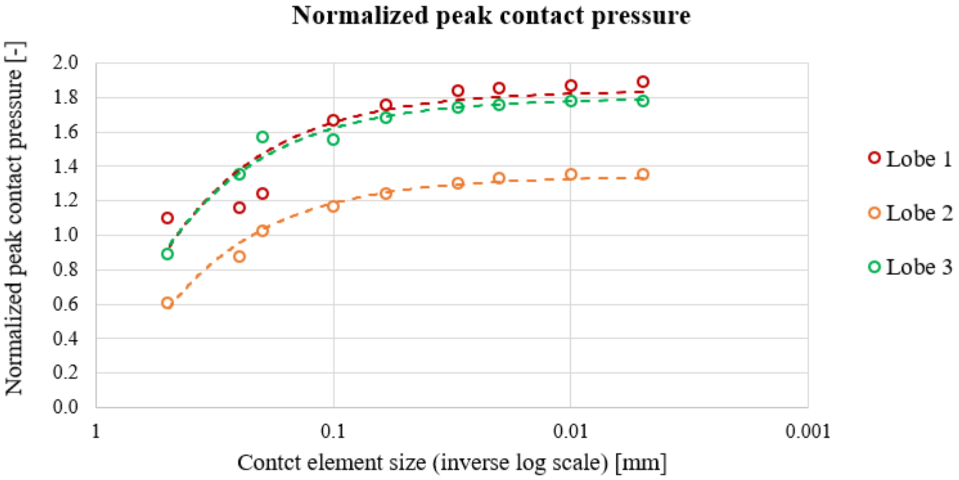

Figure 9.5. Contact pressure trend with respect to contact element size.

As shown in the picture above, the second lobe is the less loaded, while in general the first one reports the maximum pressure except from two cases, which are 270k and 43k meshes. As before, the last meshes show comparable values.

9.3. LCF comparison

In this section the results and the pictures of the critical region from LCF point of view for both blade attachment and disc groove are reported.

As explained few paragraphs before, there are two minimum values considered for blade attachment, the first occurs on contact-not contact transition zone whereas the second is internal. Both take part at the comparison.

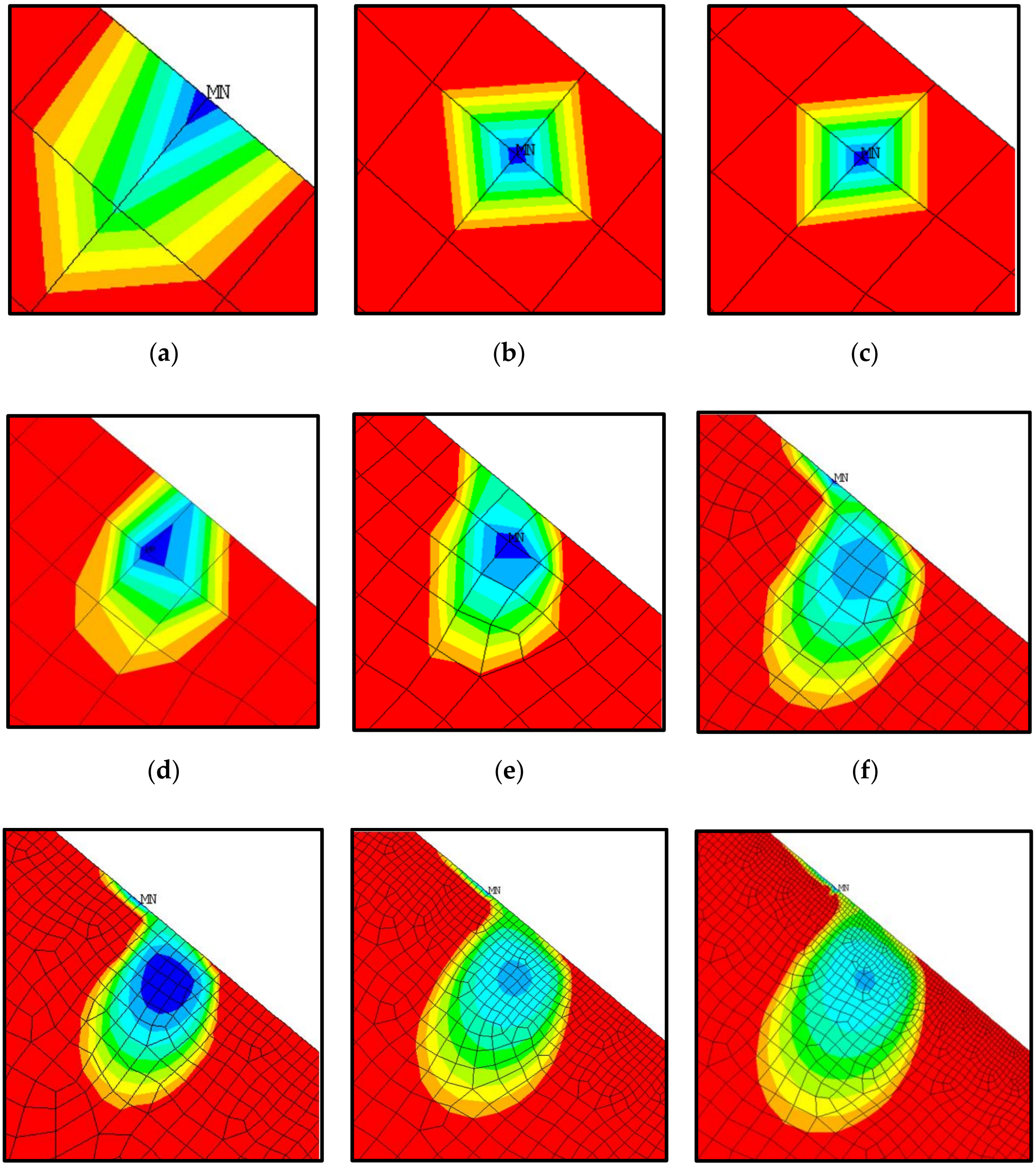

(**a**) (**b**) (**c**)

(**d**) (**e**) (**f**)

(g) **(h)** **(i)**

Figure 9.6. Blade root LCF critical region comparison. (**a**) 70k mesh; (**b**) 270k mesh; (**c**) 43k mesh;(**d**) 79k mesh; (**e**) 125k mesh; (**f**) 240k mesh; (**g**) 355k mesh; (**h**) 693k mesh; (**i**) 1350k mesh.

Figure 9.6 shows that over a given size (that is 0,03mm, see **Figure 9.1f**) the LCF minimum located at the contact – non-contact transition doesn't appear. On the other hand, the coarsest mesh (0,5mm) has the minimum located there because elements are too big to catch the correct position.

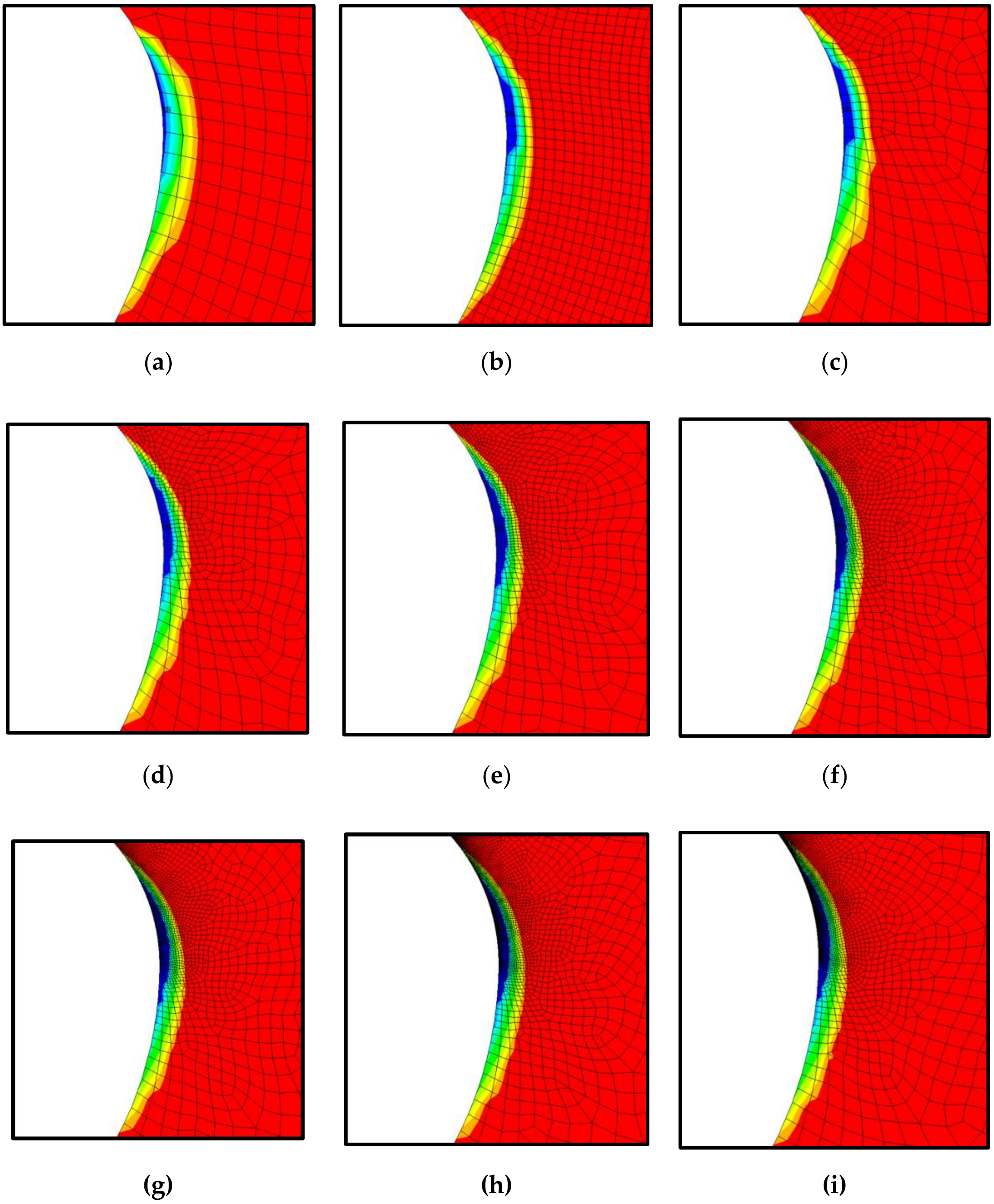
(**a**) (**b**) (**c**)

(**d**) (**e**) (**f**)

(**g**) (**h**) (**i**)

Figure 9.7. Disc groove LCF critical region comparison. (**a**) 70k mesh; (**b**) 270k mesh; (**c**) 43k mesh;(**d**) 79k mesh; (**e**) 125k mesh; (**f**) 240k mesh; (**g**) 355k mesh; (**h**) 693k mesh; (**i**) 1350k mesh.

As shown in **Figure 9.7**, the low cycle region is quite similar for all meshes. It can be concluded that mesh-independent results relative to disc groove are achieved with a larger mesh size than the ones relative to blade root. A further proof of what just written can be found in **Figure 9.8**.

Table 9.5. Blade root and disc groove LCF results.

Mesh name	Blue region minimum blade [-]	Minimum blade [-]	Minimum disc [-]
70k	1,000	1,000	1,000
270k	0,535	0,535	0,866
43k	0,358	0,358	0,856
79k	0,188	0,188	0,799
125k	0,173	0,173	0,777
240k	0,197	0,112	0,766
355k	0,198	0,197	0,761
693k	0,198	0,067	0,755
1350k	0,195	0,048	0,753

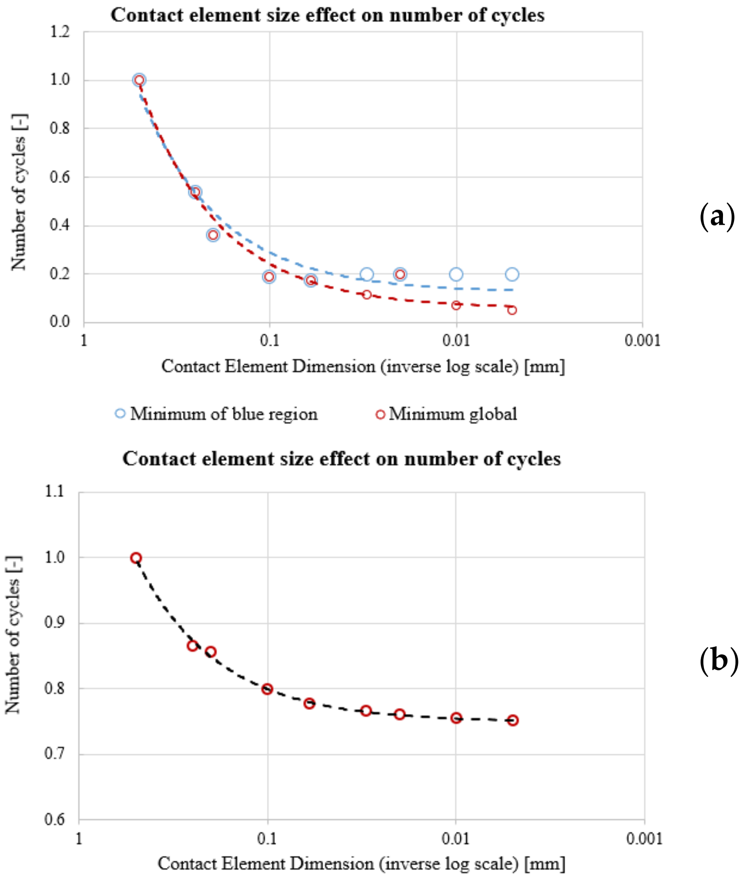

Figure 9.8. (**a**) Effect of contact mesh size on blade attachment number of cycles; (**b**) effect of contact mesh size on disc groove number of cycles.

Results reported in **Table 9.5** and **Figure 9.8** are normalized by LCF result of the 70k mesh. It can be clearly noted that mesh-independent results are obtained with a greater size for the disc then for the blade.

9.4. Final mesh selection

In sight of the results reported in sections 9.1, 9.2 and 9.3, it can stated that a good compromise between mesh-independent results and affordable computation costs can be met by the mesh named 693k, i.e. the one with element size of 0,01mm.

Further evidence of the independence of the results from the mesh is the comparison between the maximum radial stress obtained by FEA (SMX, green circles) and the maximum radial stress that *ANSYS* estimates to be the best value for the given mesh (SMXB, red circles).

As reported in **Figure 9.9**, high precision levels are already achieved with a contact mesh size of 0,1 mm (ten times greater than the chosen one).

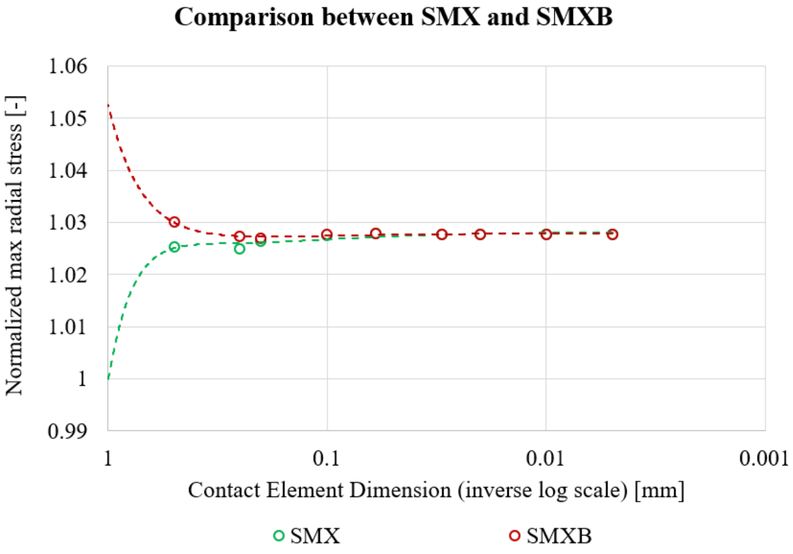

Figure 9.9. Comparison between maximum radial stress (green SMX) and maximum radial stress predicted by *ANSYS* (red SMXB).

Chosen mesh details are reported below.

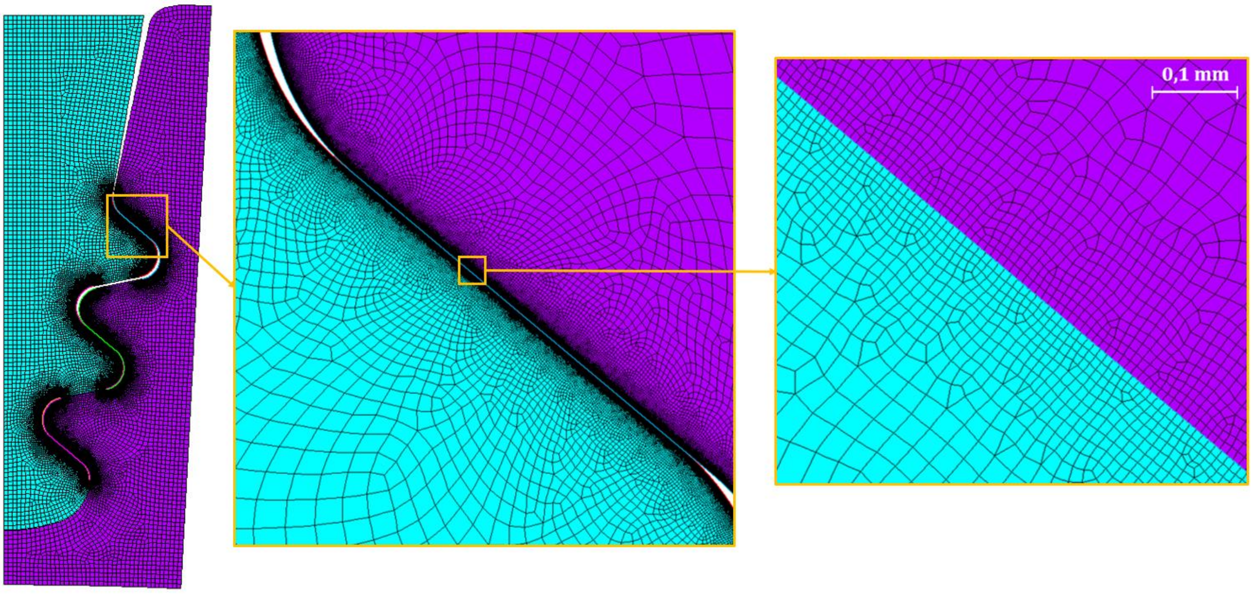

Figure 9.10. Chosen mesh for the analysis.

10. Results

For sake of briefness, in this section are reported the results of the nominal case as reference, and the ones of most representative out-of-tolerance cases. The cylindrical coordinate system (see **Figure 8.3b**) was used as reference to plot the displacements and stresses.

According to AEN procedures, for blade attachment are reported the elastic FEA results and for the disc are reported elastic-plastic FEA results. The reported contact pressures are obtained from elastic analyses. Blade attachment and disc groove results are normalized by their material's yield strength, respectively.

10.1. Nominal geometry

10.1.1. Displacements

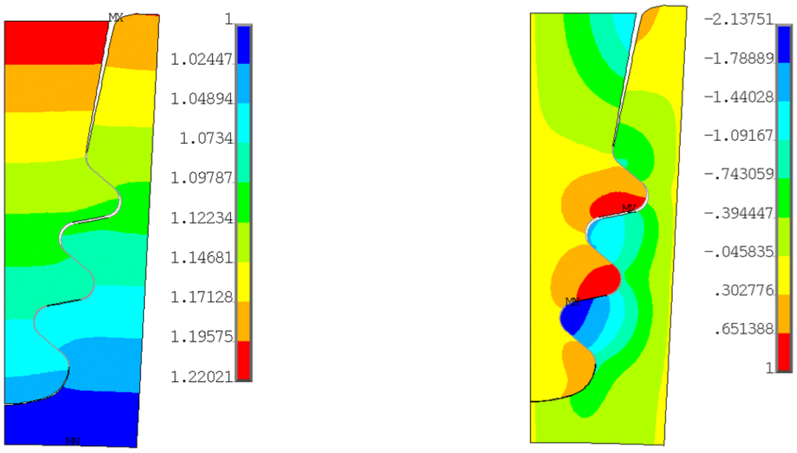

(**a**) (**b**)

Figure 10.1. (**a**) Radial displacements contours; (**b**) circumferential displacement contours. Values are normalized by a reference one.

The result obtained is consistent. Maximum radial displacement is in the blade attachment upper zone where acts the centrifugal force. The lower zone instead has minimum radial displacement, and it is the same that was imposed as boundary condition.

As shown in **Figure 10.1b** also lateral boundary conditions are consistent, in fact, circumferential displacement is zero (yellow contour).

10.1.2. Radial stress and von Mises stress distribution

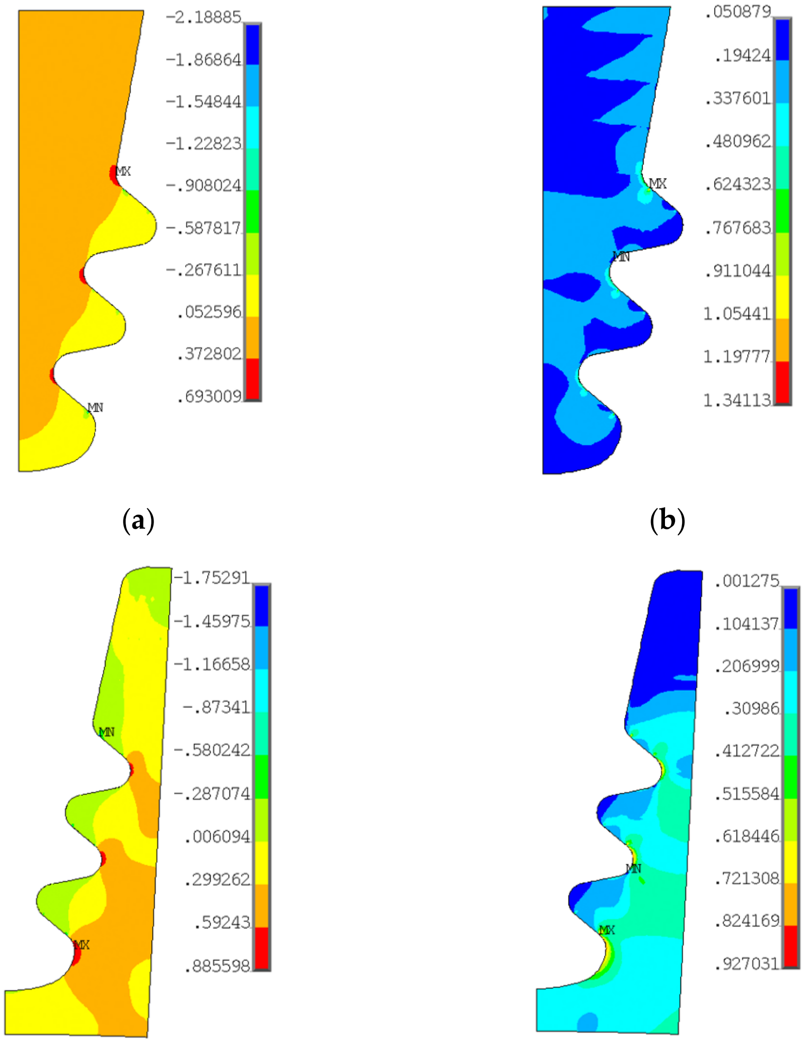

(**a**) (**b**)

(**c**) (**d**)

Figure 10.2. (**a**) blade root radial stress contours; (**b**) blade root von Mises stress contours; (**c**) disc groove radial stress contours; (**d**) disc groove von Mises stress contours.

As shown by the contours in **Figure 10.2d**, stresses in the top part of the disc groove are circa zero. High radial tensile stress (red contours) is localized on inner curved edges. These results are coherent with model physics. Tensile stress reports higher values on disc groove than on blade attachment.

The active planes of the blade attachment withstand compression stresses. Two compression peaks can be observed on the active planes located in contact – non-contact transition. In this position, a high value of von Mises stress is also reported. The same consideration can be applied to the planes of the disc groove that get in contact with blade root lobes.

In general, von Mises stress has higher values on the disc groove than on the blade attachment. Highest values are recorded on the inner curved edges.

10.1.3. Contact results

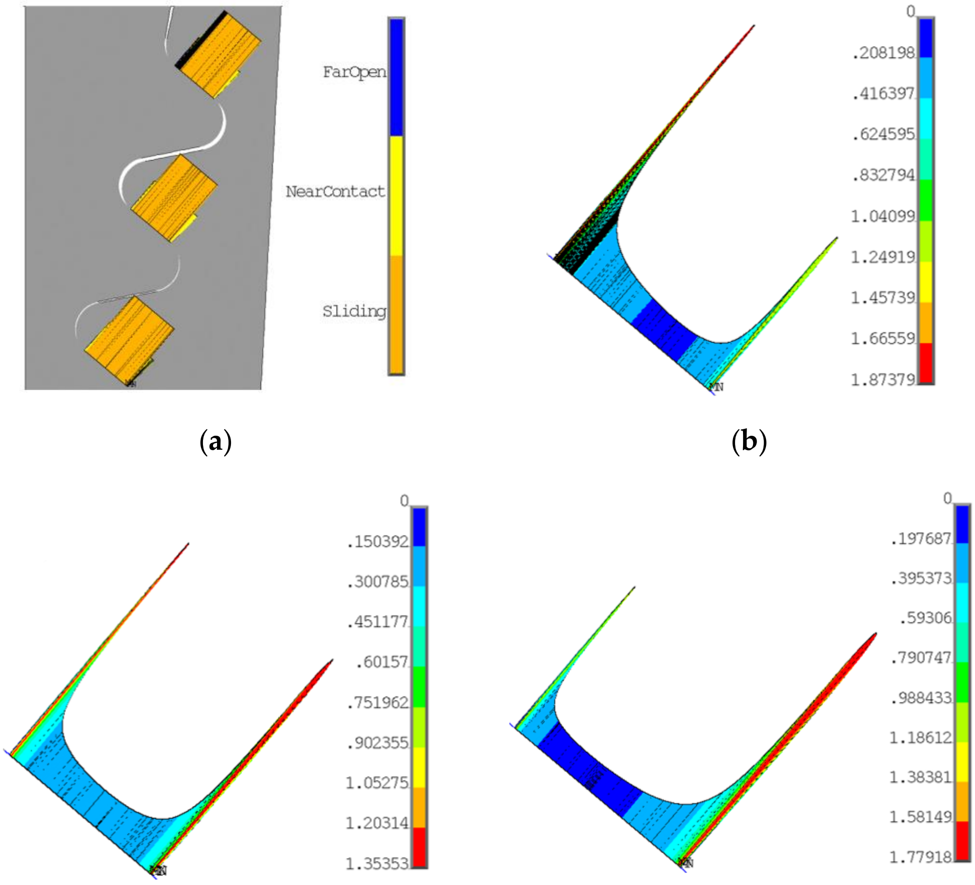
FarOpen
NearContact
Sliding
0
.208198
.416397
.624595
.832794
1.04099
1.24919
1.45739
1.66559
1.87379
0
.150392
.300785
.451177
.60157
.751962
.902355
1.05275
1.20314
1.35353
0
.197687
.395373
.59306
.790747
.988433
1.18612
1.38381
1.58149
1.77918

(**a**) (**b**)

(**c**) (**d**)

Figure 10.3. (**a**) contact status; (**b**) contact pressure on lobe 1; (**c**) contact pressure on lobe 2; (**d**) contact pressure on lobe 3.

As expected for flat active planes, there are two peaks where the contact ends. Contact pressure peaks are located in the same position of the radial compression peaks. Contact status in **Figure 10.3a** shows where the is contact

(*Sliding*) and where there is the transition between contact – non-contact (*Near Contact*).

10.1.4. LCF evaluation

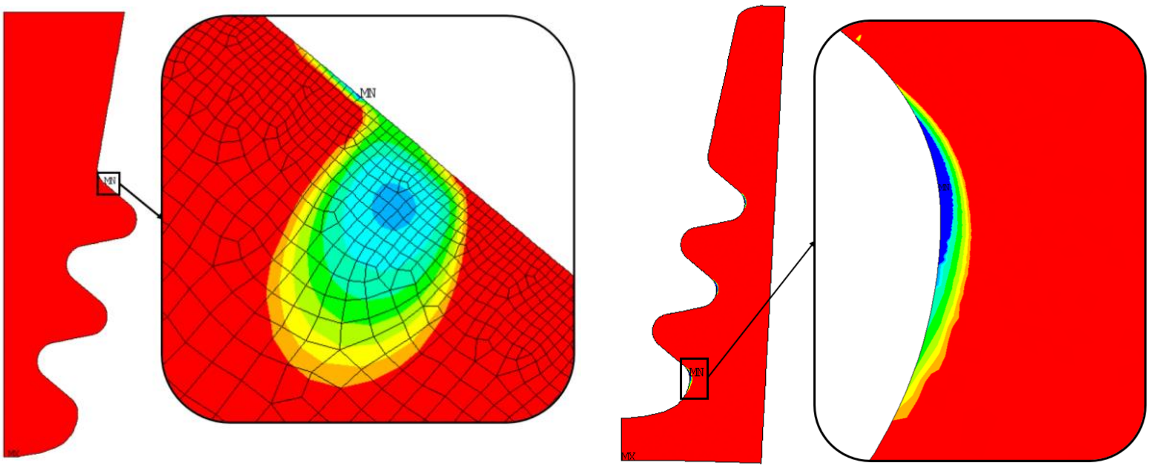

(**a**) (**b**)

Figure 10.4. (**a**) blade fir-tree attachment – number of cycles distribution and critical zone; (**b**) disc groove – number of cycles distribution and critical zone.

As shown in **Figure 10.4**, almost everywhere the attachment exceeds the maximum considered LCF limit. The value chosen as reference is the minimum on the blue region in depth. As written in section 5.1, these fatigue results are obtained from elastic calculation.

As for the attachment, also here number of cycles exceeds the maximum reference limit. There are three main zones that report a lower number of cycles and those zones are near the inner curved edge of the groove. These zones are the ones that reports high radial tensile stress and von Mises equivalent stress as shown in **Figure 10.2**. Disc groove LCF results are obtained from elastic-plastic calculations.

10.2. Out-of-tolerance on the active plane angle of the third lobe

10.2.1. Radial and von Mises stress distribution

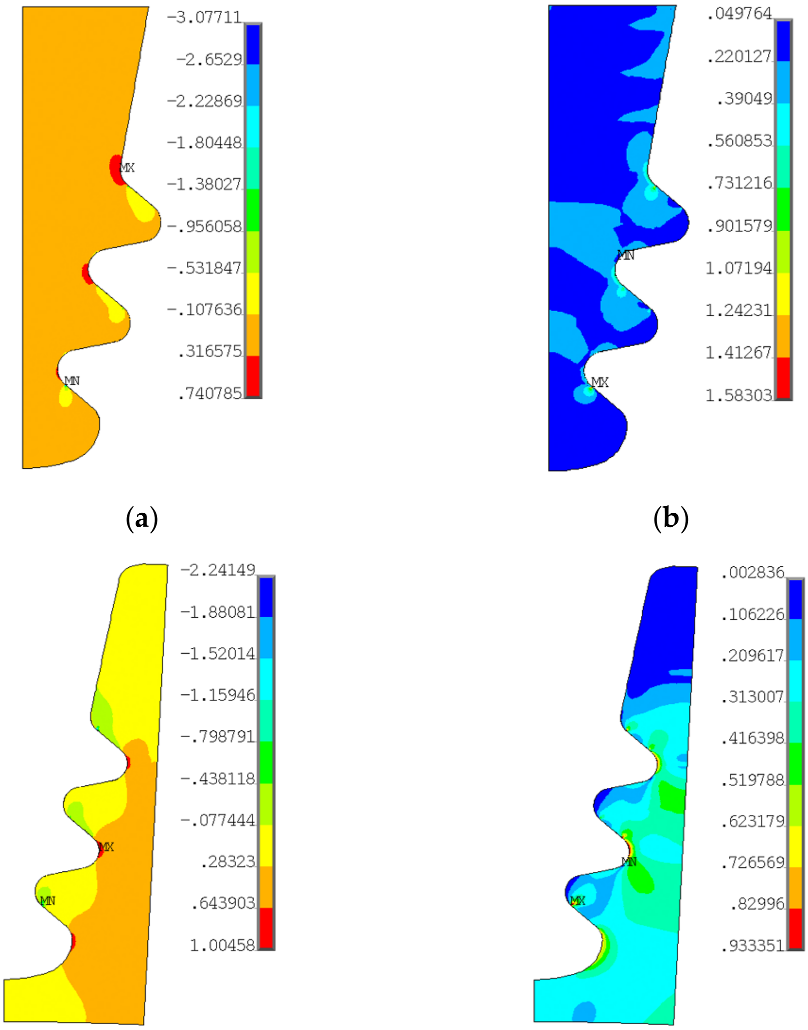
-3.07711
-2.6529
-2.22869
-1.80448
-1.38027
-.956058
-.531847
-.107636
.316575
.740785
MX
MN
.049764
.220127
.39049
.560853
.731216
.901579
1.07194
1.24231
1.41267
1.58303
MN
MX
-2.24149
-1.88081
-1.52014
-1.15946
-.798791
-.438118
-.077444
.28323
.643903
1.00458
MX
MN
.002836
.106226
.209617
.313007
.416398
.519788
.623179
.726569
.82996
.933351
MN
MX

(**a**) (**b**)

(**c**) (**d**)

Figure 10.5. (**a**) blade root radial stress contours; (**b**) blade root von Mises stress contours; (**c**) disc groove radial stress contours; (**d**) disc groove von Mises stress contours.

Radial stress distribution on the blade root is now considered. The first consideration to be done is that there is much more tensile stress (red contour) on first and second lobe, while on the third lobe the red contour is reduced respect to nominal case. Besides, compression peak (*MN* on the image) on third lobe has moved from right to left side. Maximum radial stress is located in the same position. Maximum von Mises stress moved from active plane of lobe 1 to active plane of lobe 3. The von Mises stress distribution is quite similar in both cases.

Now the attention is focused on the disc groove. Red contour of radial stress on groove 3 is reduced respect to nominal geometry and, as a consequence, maximum radial stress value has moved to groove 2. The minimum value has moved from the first groove to the third one.

The maximum value of von Mises stress has moved from the right to the left of the third groove, while the minimum is on the same position. Greater values are recorded on groove 2 (red and yellow contour are larger).

10.2.2. Contact status and pressure

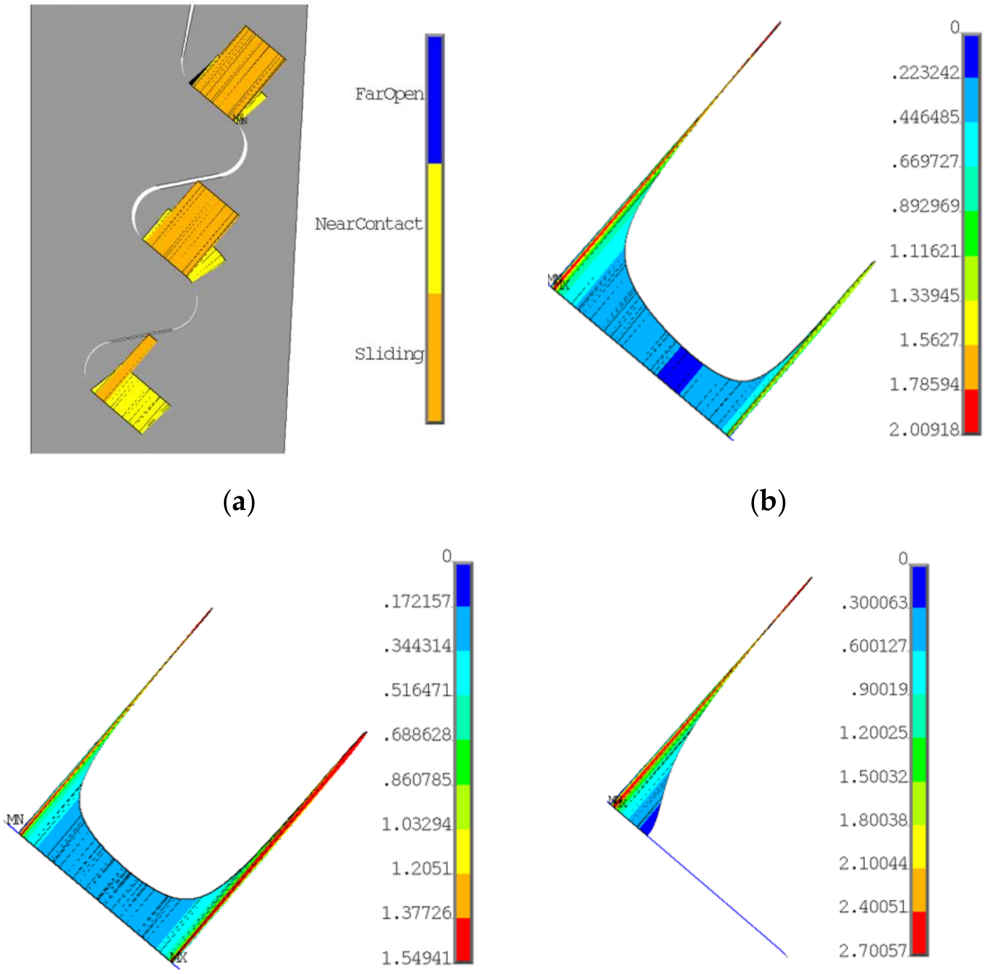

(**a**) (**b**)

(**c**) (**d**)

Figure 10.6. (**a**) contact status; (**b**) contact pressure on lobe 1; (**c**) contact pressure on lobe 2; (**d**) contact pressure on lobe 3.

Coherently with geometry modification, third active plane is loaded only on the left side due to the applied rotation of the active plane. As shown in **Figure 10.6d**, the right side of the active plane doesn't get in contact with disc groove (*Near*

Contact contour). Pressure peak here is much higher than in nominal geometry. Regarding lobe 1 and 2, there are no significant consideration to be done.

10.2.3. LCF evaluation

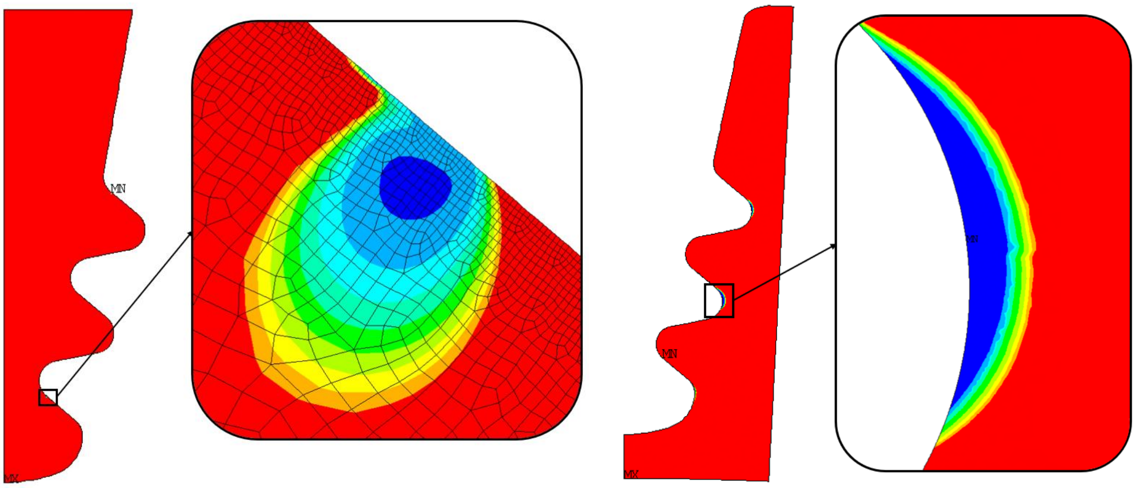

(**a**) (**b**)

Figure 10.7. (**a**) blade fir-tree attachment – number of cycles distribution and critical zone; (**b**) disc groove – number of cycles distribution and critical zone.

The blade attachment LCF critical region has moved from first to third lobe, coherently with the results reported above. Respect to nominal case, blade attachment life has been reduced about 54%.

About the disc groove, the LCF minimum has moved from third groove to the second one. Also in this case, the result is coherent with stress distribution reported above. Disc groove LCF have suffered circa 79% reduction.

10.3. Out-of-tolerance on the active plane offset of the second lobe

10.3.1. Radial and von Mises stress distribution

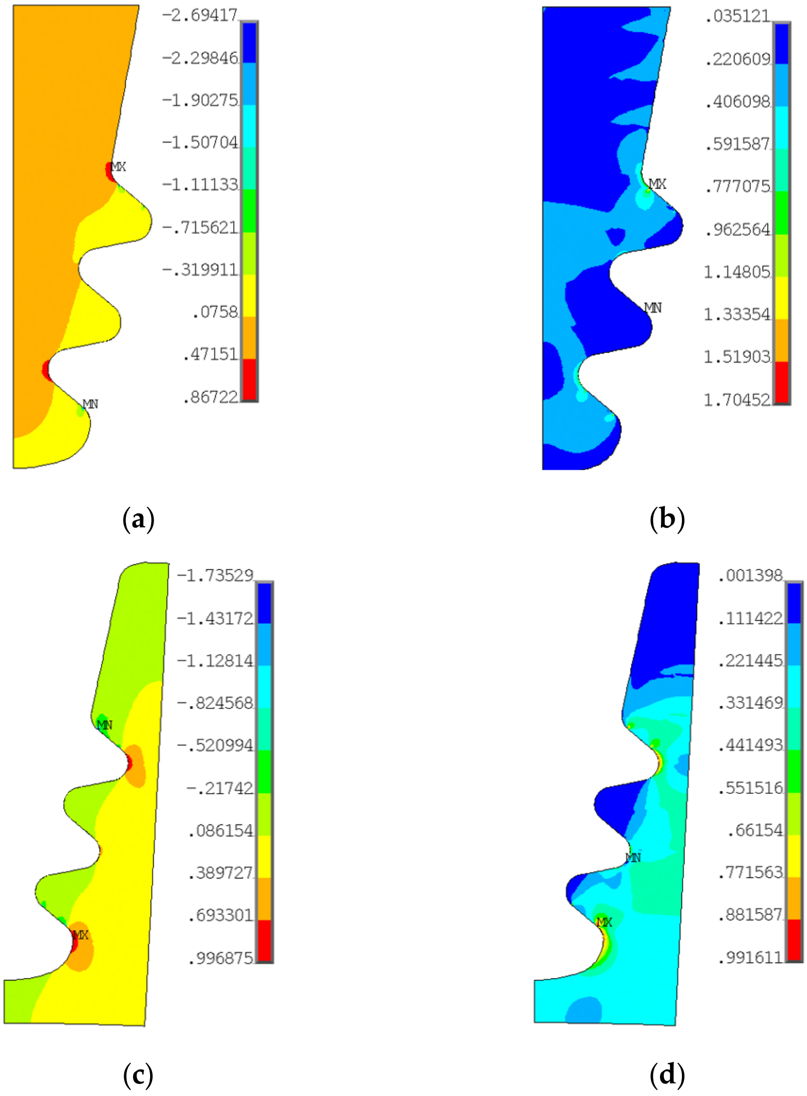
-2.69417
-2.29846
-1.90275
-1.50704
-1.11133
-.715621
-.319911
.0758
.47151
.86722
MX
MN
.035121
.220609
.406098
.591587
.777075
.962564
1.14805
1.33354
1.51903
1.70452
MX
MN
-1.73529
-1.43172
-1.12814
-.824568
-.520994
-.21742
.086154
.389727
.693301
.996875
MN
MX
.001398
.111422
.221445
.331469
.441493
.551516
.66154
.771563
.881587
.991611
MN
MX

(**a**) (**b**)

(**c**) (**d**)

Figure 10.8. (**a**) blade root radial stress contours; (**b**) blade root von Mises stress contours; (**c**) disc groove radial stress contours; (**d**) disc groove von Mises stress contours.

Looking at blade root stress distribution, the only notable difference respect to nominal case is that lobe 2 is almost unloaded. The radial stress red contour here has disappeared like the compression peaks, and von Mises stress is zero all over the lobe.

From disc side, higher tensile radial stress is recorded on the first and third groove, while the one on groove 2 is much reduced. The same considerations apply to von Mises stress.

10.3.2. Contact status and pressure

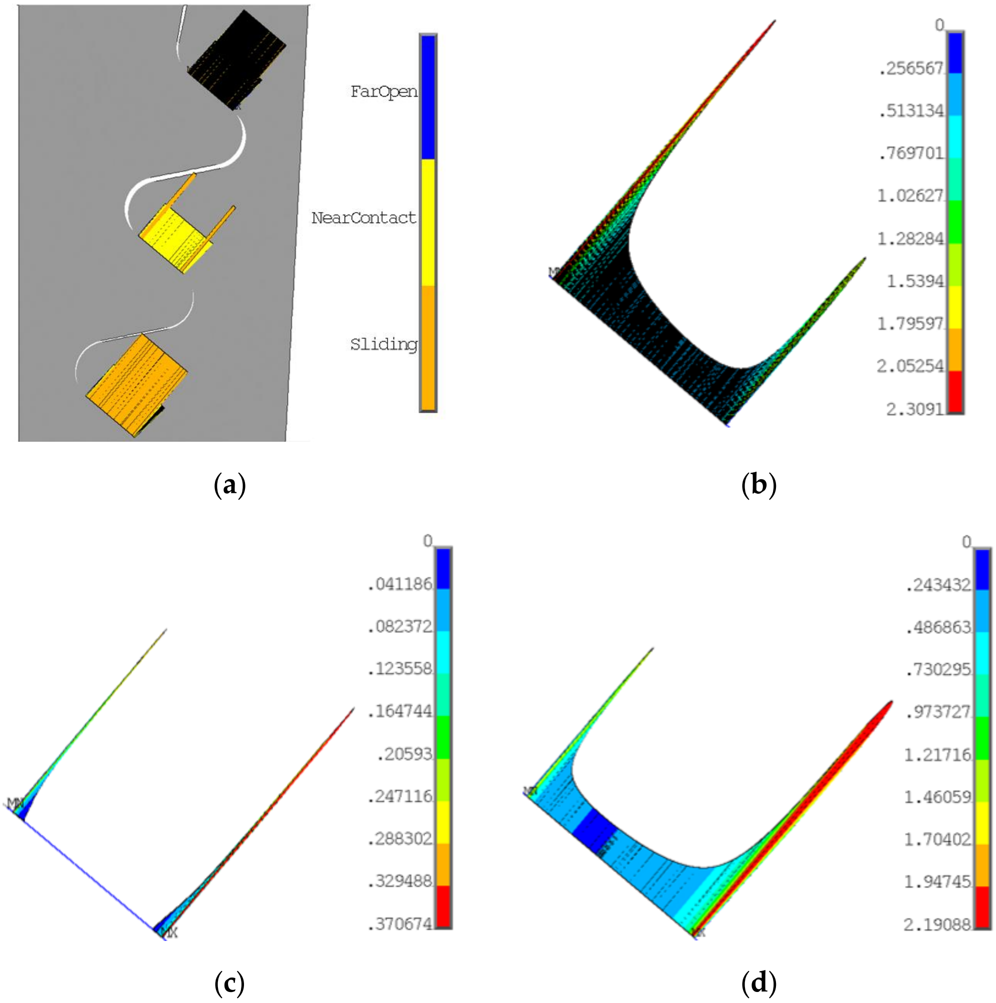
FarOpen
NearContact
Sliding
0
.256567
.513134
.769701
1.02627
1.28284
1.5394
1.79597
2.05254
2.3091
0
.041186
.082372
.123558
.164744
.20593
.247116
.288302
.329488
.370674
0
.243432
.486863
.730295
.973727
1.21716
1.46059
1.70402
1.94745
2.19088

(**a**) (**b**)

(**c**) (**d**)

Figure 10.9. (**a**) contact status; (**b**) contact pressure on lobe 1; (**c**) contact pressure on lobe 2; (**d**) contact pressure on lobe 3.

Figure 10.9 confirm that the second lobe is almost unloaded. There is no contact except at the boundaries of the active plane. Peak pressures on lobe 1 and 3 are greater, because now they withstand also the load that in nominal case was on lobe 2.

10.3.3. LCF evaluation

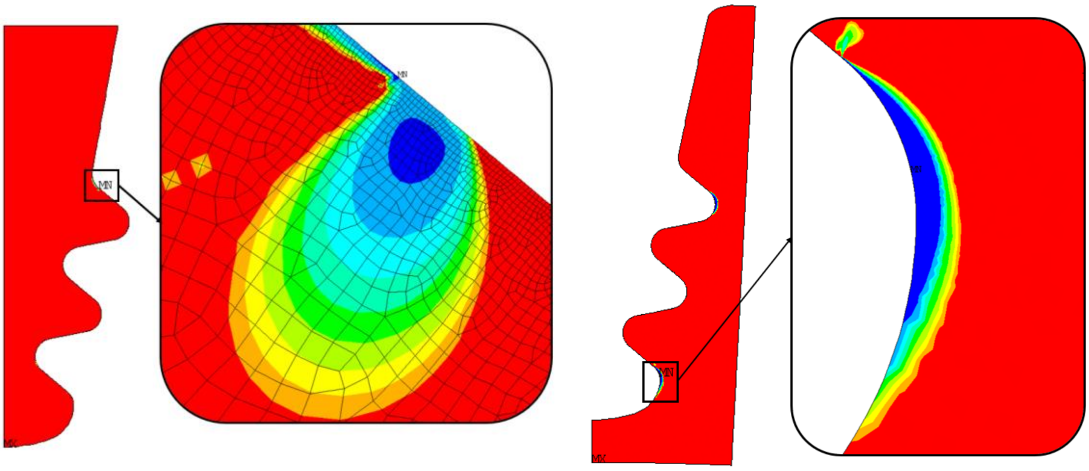

(**a**) (**b**)

Figure 10.10. (**a**) blade fir-tree attachment – number of cycles distribution and critical zone; (**b**) disc groove – number of cycles distribution and critical zone.

The critical region on blade attachment now is larger than in nominal geometry and takes also the curved edge over the active plane, in fact stresses here are higher than in nominal geometry. Out-of-tolerance caused fatigue life reduction of about 68%.

Regarding the disc, the low number of cycles zone is larger than in nominal geometry. As in nominal geometry, the minimum is located on the third groove. The low number of cycles area on groove has disappeared (all nodes exceed the maximum limit), while the one on groove 1 has become larger. In percentual terms, life has been reduced of circa 79%.

10.4. All parameters on maximum out-of-tolerance values

10.4.1. Radial and von Mises stress distribution

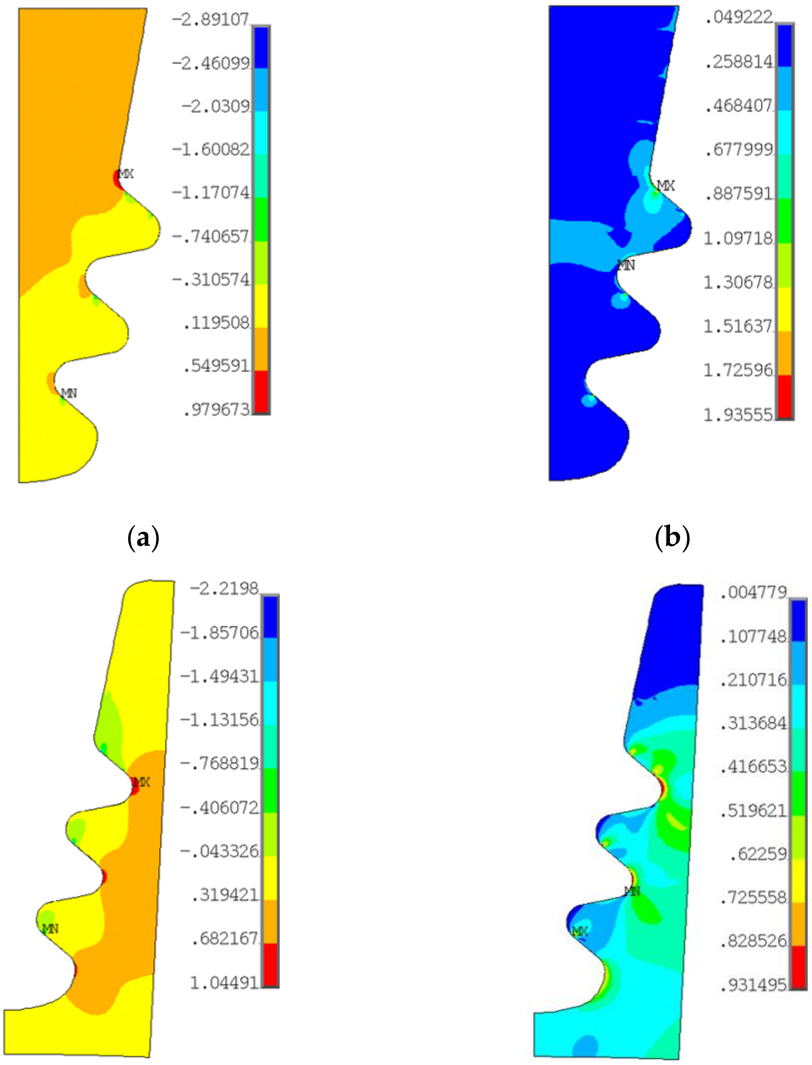

(**a**) (**b**)

(**c**) (**d**)

Figure 10.11. (**a**) blade root radial stress contours; (**b**) blade root von Mises stress contours; (**c**) disc groove radial stress contours; (**d**) disc groove von Mises stress contours.

Blade root stress distribution is now discussed. From radial stress point of view, the red contours on the second lobe and third now has disappeared. There are larger compression contours (green ones) on the first lobe, while on the second and third lobes compression contours are on the left side only. This stress distribution is mainly related to angles rotations. The dark blue contour of von Mises stress is greater than in all previous cases, meaning that this is the worst case in terms of load distribution on lobes. In fact, there are only localized high stress regions near the left side of each active plane.

Now the focus is put on the disc groove. Considering radial stress distribution, it can be said that compression region on each groove is much greater than in nominal geometry. Compression is located only on the left side of the grooves. Tensile stress is lower on the third groove, and are greater on the first one. In fact, maximum radial stress has moved from third to first groove while the minimum has done the reverse route. From von Mises stress distribution, it can be clearly observed that groove 1 is much more stressed than in nominal case. Higher values are also recorded on groove 2, while groove 3 reported no relevant difference. The only difference here is the position of the maximum value, coherent with the angle rotation, on the left side.

10.4.2. Contact status and pressure

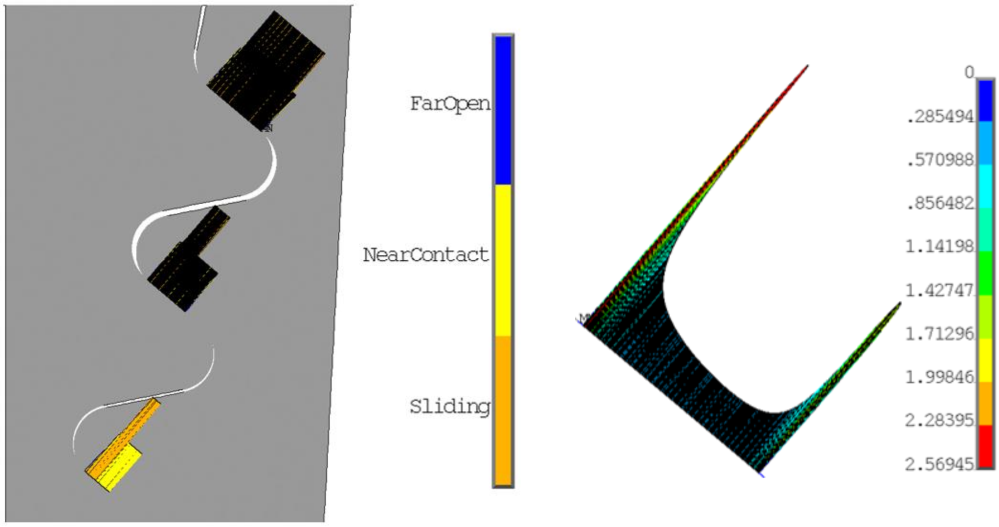

(**a**) (**b**)

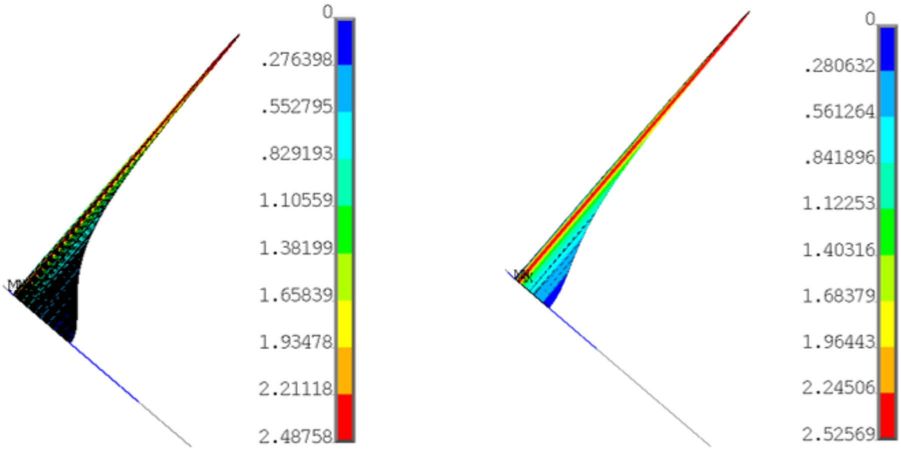

(**c**) (**d**)

Figure 10.12. (**a**) contact status; (**b**) contact pressure on lobe 1; (**c**) contact pressure on lobe 2; (**d**) contact pressure on lobe 3.

From **Figure 10.12a** it is clear that only a part of lobe 2 and 3 gets in contact with disc groove. Peak pressures on each lobe are much higher than in nominal case. These contact results are coherent with stress distribution reported in the preceding section.

10.4.3. LCF evaluation

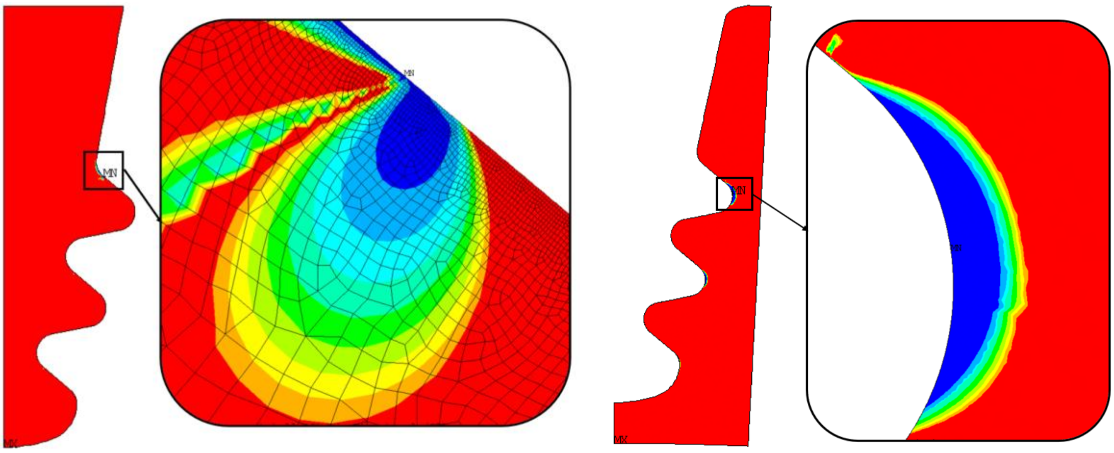

(**a**) (**b**)

Figure 10.13. (**a**) blade fir-tree attachment – number of cycles distribution and critical zone; (**b**) disc groove – number of cycles distribution and critical zone.

Blade attachment LCF critical region is larger than in all previous cases, confirming that in this case load distribution is the worst. The dark blue region extends to the curved edge on the left side of the active plane, in fact here tensile stress are high. In this case, blade attachment lost about 84% of its nominal cycles.

LCF critical region of the disc groove now is located on the first groove. This result could be expected from stress distribution in **Figure 10.11c** and **d**. Disc groove suffered about 89% fatigue life reduction.

11. Comparison with nominal geometry results

Results obtained from nominal geometry evaluation are taken as reference for the comparison.

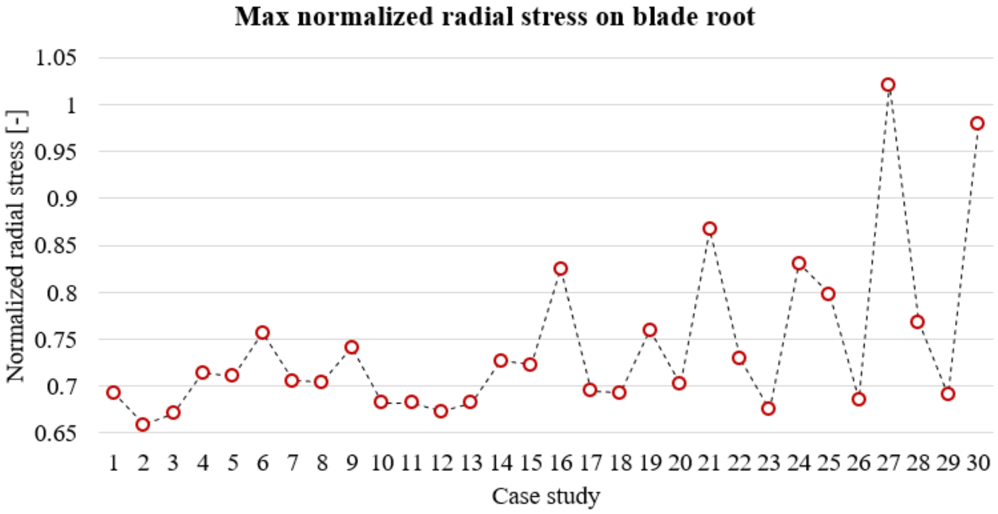

Figure 11.1. Comparison of maximum radial stress on the blade root.

Figure 11.1 shows that the case study number 27 ($L_{1,2}$ max) reported maximum radial stress on the blade attachment. To perform a reliable comparison, the node that recorded this value was taken as reference. The region of interest is the one surrounded by the black square in **Figure 11.2a**. Hence, for all the other case studies an equivalent node was selected and its radial stress value was saved. **Figure 11.2b** reports these results.

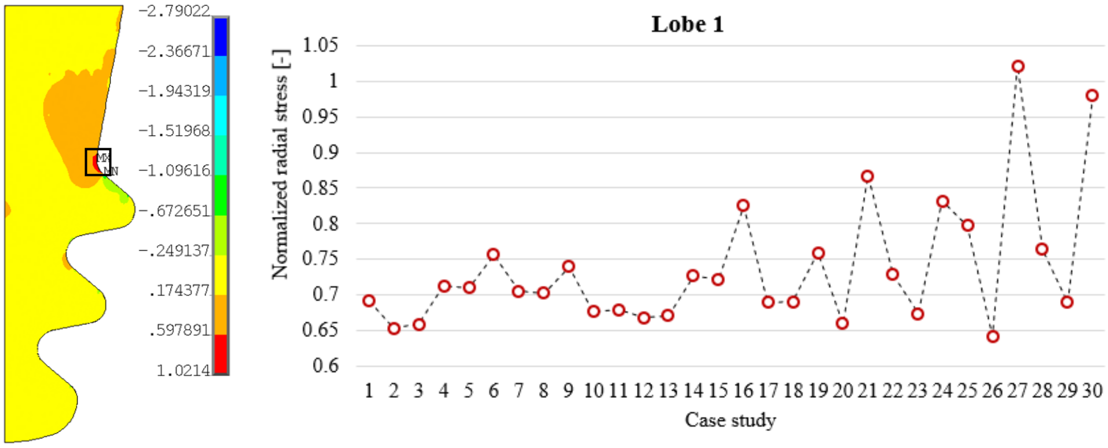

(**a**) (**b**)

Figure 11.2. (**a**) radial stress distribution in $L_{1,2}$ max case; (**b**) Comparison of radial stress for the first lobe of the blade root.

The maximum value of radial stress in case number 27 ($L_{1,2}$ max) was recorded on the first lobe, like in the nominal geometry. The percentage increase is 47% compared with the nominal case. The modification done consisted of a downward translation of the second and third active planes. A gap has therefore been created between blade root and disc groove causing an overload on the first active plane because this comes in contact much earlier than the other two. This is the reason that lead to such an increase in radial stress. A similar consideration can be applied to case 30 ($\alpha_{2,3}$, $L_{1,2}$ max, see section 10.4), in this case together with offset downward translation has been applied a clockwise rotation to active planes 2 and 3 ($\alpha_{2,3}$). In this case the maximum radial stress is a little bit lower than in the previous one because active planes rotation causes them to come into contact with disc groove earlier, even if only partially (see **Figure 10.12**). In case number 30 ($\alpha_{2,3}$, $L_{1,2}$ max), the percentage radial stress increase is 41%. The same applies to downward translation of the active plane of lobe 2 and 3 individually, i.e. case number 21 (L_1 max) and case number 24 (L_2 max).

In general, a downward translation of the active planes of lobes 2 and 3 (upper tolerance or maximum out-of-tolerance of parameters L_1 and L_2), individually or combined together, causes an increase in maximum radial stress while the opposite translation (lower tolerance of parameters L_1 and L_2) causes a decrease in maximum radial stress, in fact an upward translation makes the second and third active planes to come into contact before the first one. Clearly, this effect is much more visible in out-of-tolerance cases (*max*).

Angles rotation will now be discussed. In **Figure 11.2b** it can be understood that a rotation of the first active plane, both clockwise or counter clockwise, individually or combined with other angles, causes a decrease of maximum radial stress on lobe 1 compared with nominal case. This can be explained considering that a modification of this active plane causes a non-optimal contact, i.e. that a part or the active plane comes into contact before than the other, and therefore lobes 2 and 3 withstands a higher load. In fact, in these cases radial stress on lobes 2 and 3 is higher than in nominal case.

Figure 11.3 shows the same comparison for the second and third lobes. A reference node located in the red contour radial stress of lobe 2 and 3 was chosen for the comparison (see **Figure 10.2a**).

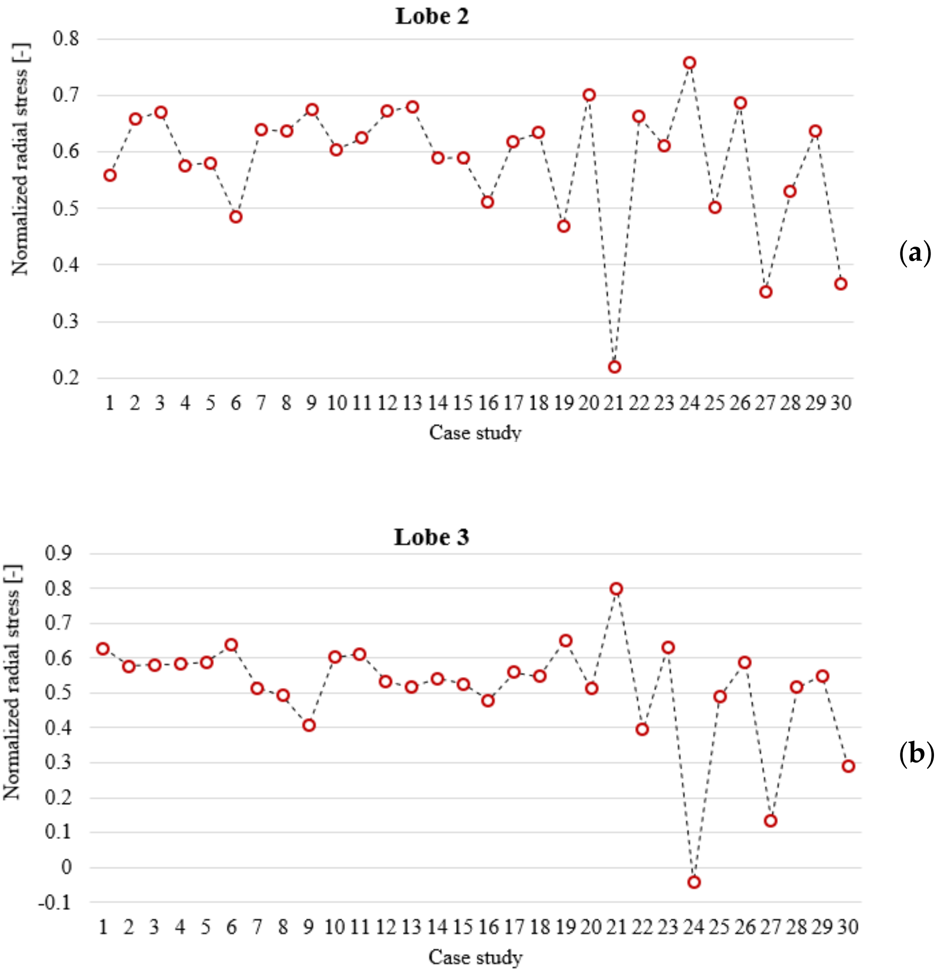

Figure 11.3. (**a**) Comparison of radial stress for the second lobe of the blade root; (**b**) Comparison of radial stress for the third lobe of the blade root.

Looking at **Figure 11.2b** and **Figure 11.3** it can be stated that applying out-of-tolerance to the angles leads to an overloading of the remaining nominal active planes. Considering α_2 *max* case, it can be observed that the active planes of lobes 1 and 3 withstand a higher load while the active plane of lobe 2 is less loaded. Analogous consideration can be done for α_3 *max* case. The combination of the two, i.e. case number 16 ($\alpha_{2,3}$ *max*), causes an overload of lobe 1, while lobe 2 and 3 withstand a lower load. The reason could be that by changing an angle, only a portion of the active plane comes into contact and is not sufficient to withstand the entire load, which is redistributed on the other active planes.

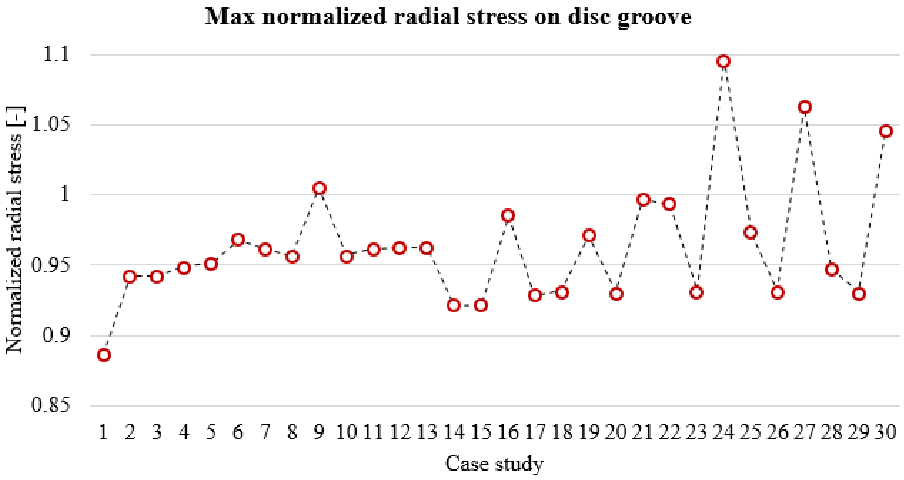

Figure 11.4. Comparison of maximum radial stress on the disc groove.

From disc side, the most critical case is number 24 (L_2 *max*), in fact radial stress is increased about 23,7%. Other remarkable case studies in terms of radial stress increase are cases number 16 ($\alpha_{2,3}$ *max*), 27 ($L_{1,2}$ *max*) and 30 ($\alpha_{2,3}$, $L_{1,2}$ *max*). In general, the considerations already done for the blade attachment are suitable also for the disc groove.

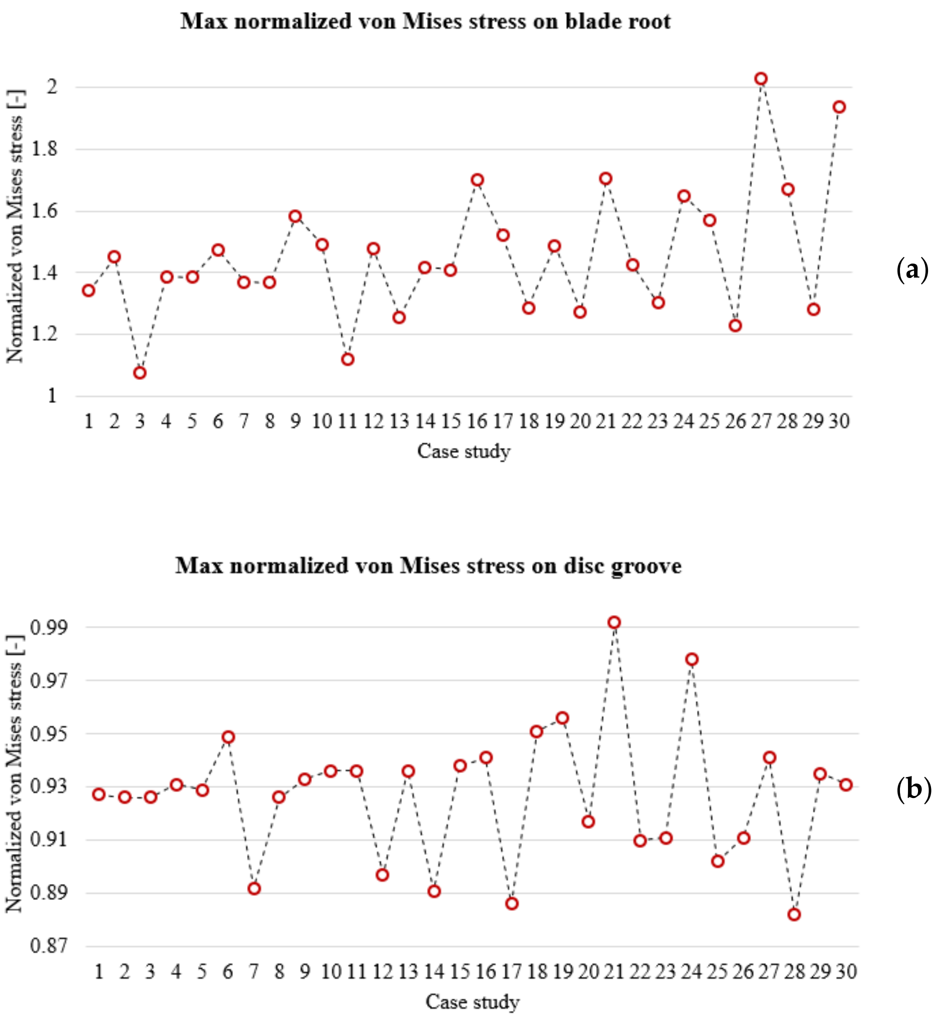

Figure 11.5. (**a**) Comparison of maximum von Mises stress on the blade root; (**b**) Comparison of maximum von Mises stress on the disc groove.

As reported in **Figure 11.5**, the most critical cases in terms of von Mises equivalent stress are number 27 ($L_{1,2}$ *max*) from blade root side and number 21 (L_1 *max*) from disc side. In nominal geometry case study, the maximum von Mises stress was recorded on the left side of the first active plane of the blade attachment (see **Figure 10.2c**) on the right side of the third disc groove (see **Figure 10.2d**).

Two gaps between contact surfaces in lobes 2 and 3 are created in case number 27 ($L_{1,2}$ *max*). As a consequence, the first lobe withstands a higher load, increasing its maximum von Mises stress about 51%.

In case number 21 (L_1 *max*) a gap is created between contact surfaces on the second lobe and groove, and for this reason, the load is redistributed on lobes and grooves 1 and 3. Given that groove 3 was already the most loaded one and gets a further amount of load, this explains why L_1 *max* is the most critical with about 7% von Mises stress increase.

It has to be considered that blade attachment results are obtain through an elastic FEA, while disc groove ones are obtained through elastic-plastic FEA. Variation related to the disc groove respect to nominal geometry are smaller because one reached the yield point, stresses increases much slowly than in simple elastic case. The same comparison done considering elastic calculation leads to an increase of about 29% in maximum von Mises stress on the disc groove.

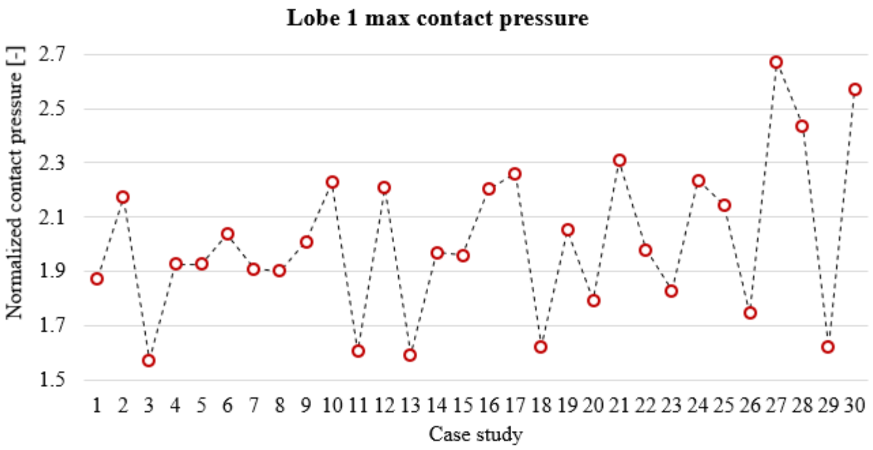

(**a**)

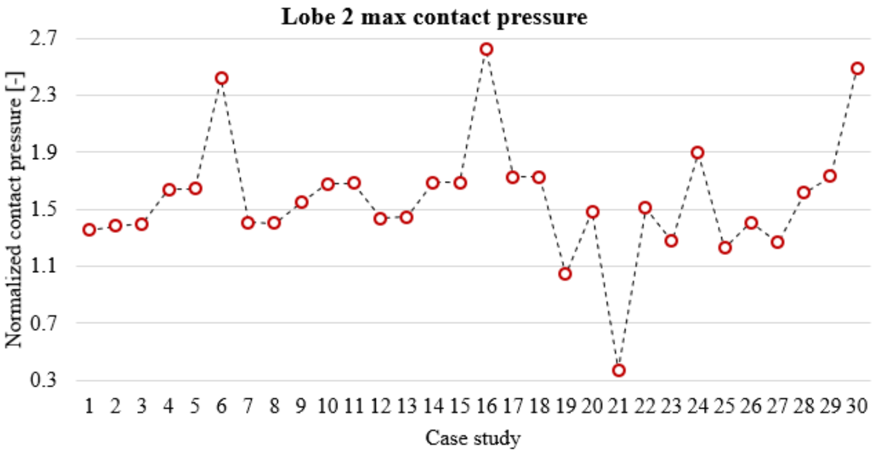

(**b**)

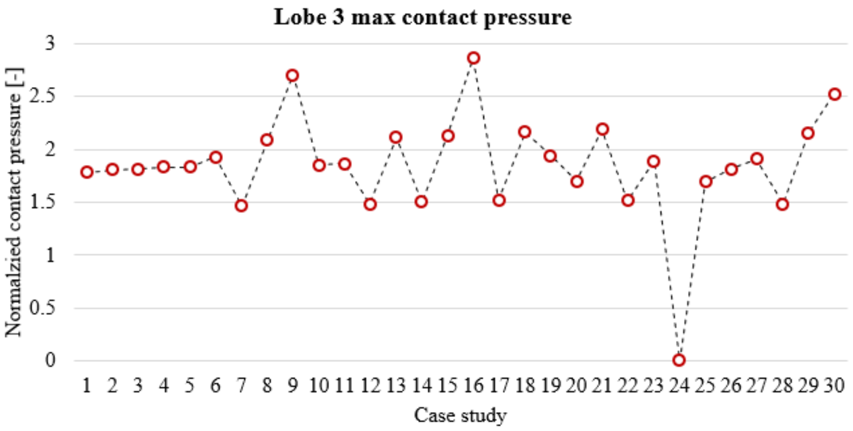

(**c**)

Figure 11.6. (**a**) contact pressure on lobe 1 comparison; (**b**) contact pressure on lobe 2 comparison; (**c**) contact pressure on lobe 3 comparison.

Contact pressure results are coherent with stress ones. Another time, the same consideration written in the previous paragraphs can be now applied. Angles modification leads to higher contact pressure on the modified active plane due to a non-optimal contact distribution. Examples are the peak values recorded in case number 6 (α_2 max, see **Figure 11.6b**), α_3 max case number 9 (α_3 max, see **Figure 11.6c**) and case number 16 ($\alpha_{2,3}$ max, see **Figure 11.6b** and **c**).

Another general trend is observable in **Figure 11.6a**: if a counter clockwise rotation of the first active plane is applied, i.e. lower tolerance limit of angle α_1, maximum contact pressure on lobe 1 decreases. This is correct considering that the maximum in nominal case was located on the left side of the active plane and applying this rotation creates a little gap on this side of the contact.

Applying out-of-tolerance value to offsets L_1 and L_2 causes a great decrease in contact pressure on the correspondent lobes (see case 21, i.e. L_1 max, in **Figure 11.6b**, case 24, i.e. L_2 max, in **Figure 11.6c** and case 27, i.e. $L_{1,2}$ max, in **Figure 11.6b** and **c**) and an increase on the others.

Out-of-tolerances in blade fir-tree geometry lead to a significant decrement in number of cycles, for both blade and disc. Even though such a decrement, minimum requirements are satisfied if we consider mean curve and not design curve for the evaluation.

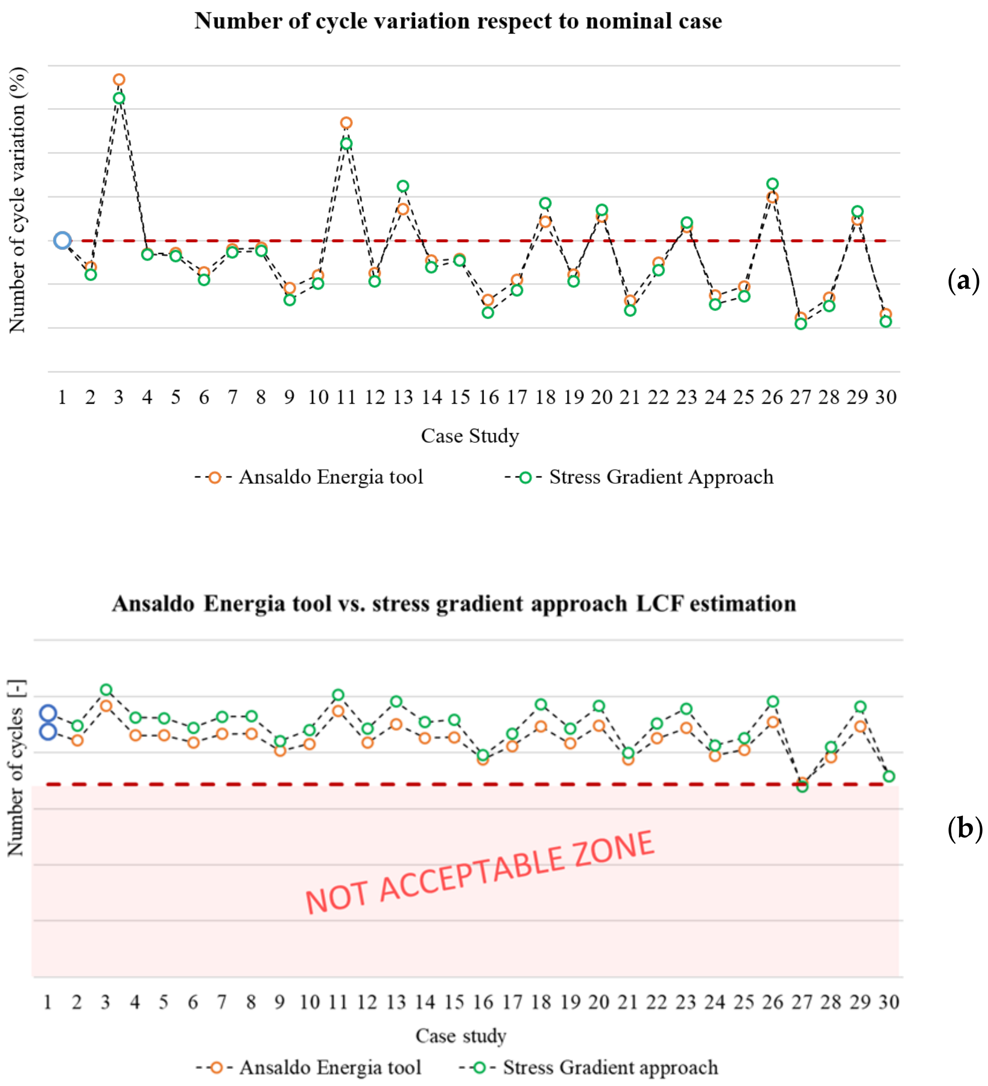

Figure 11.7. LCF estimations of the blade attachment. (**a**) Comparison of number of cycles percentage variations respect to nominal results; (**b**) comparison of number of cycles for each case.

Looking at **Figure 11.7** it can be clearly stated that all cases involving a counter clockwise rotation of the first active planes, i.e. lower tolerance limit of angle α_1, records an increase in fatigue life. The same happens when is applied an upward translation of the active plane of the lobes 2 and 3, i.e. lower tolerance limit of offsets L_1 and L_2. This is due to the fact that the critical region from LCF point of view (see **Figure 10.4a**) in these cases withstands a lower load and thus number of cycles here increases.

Instead, if we consider out-of-tolerance cases, it can be seen that a relevant percentage of life is lost. The highest losses are recorded for cases number 27 ($L_{1,2}$

max) and 30 ($\alpha_{2,3}$, $L_{1,2}$ *max*), but there also other relevant cases such as number 16 ($\alpha_{2,3}$ *max*), 21 (L_1 *max*) and 24 (L_2 *max*).

Other cases like number 17 ($\alpha_{1,2,3}$ *toll up*), 25 ($L_{1,2}$ *toll up*) and 28 ($\alpha_{1,2,3}$, $L_{1,2}$ *toll up*) shows a considerable life reduction. This are all cases that leads to an increase of stresses and contact pressure in the LCF critical region (left side of the first active plane).

As it can be observed in the figure above, the two approaches to LCF estimation (AEN tool and stress gradient) give almost equal results.

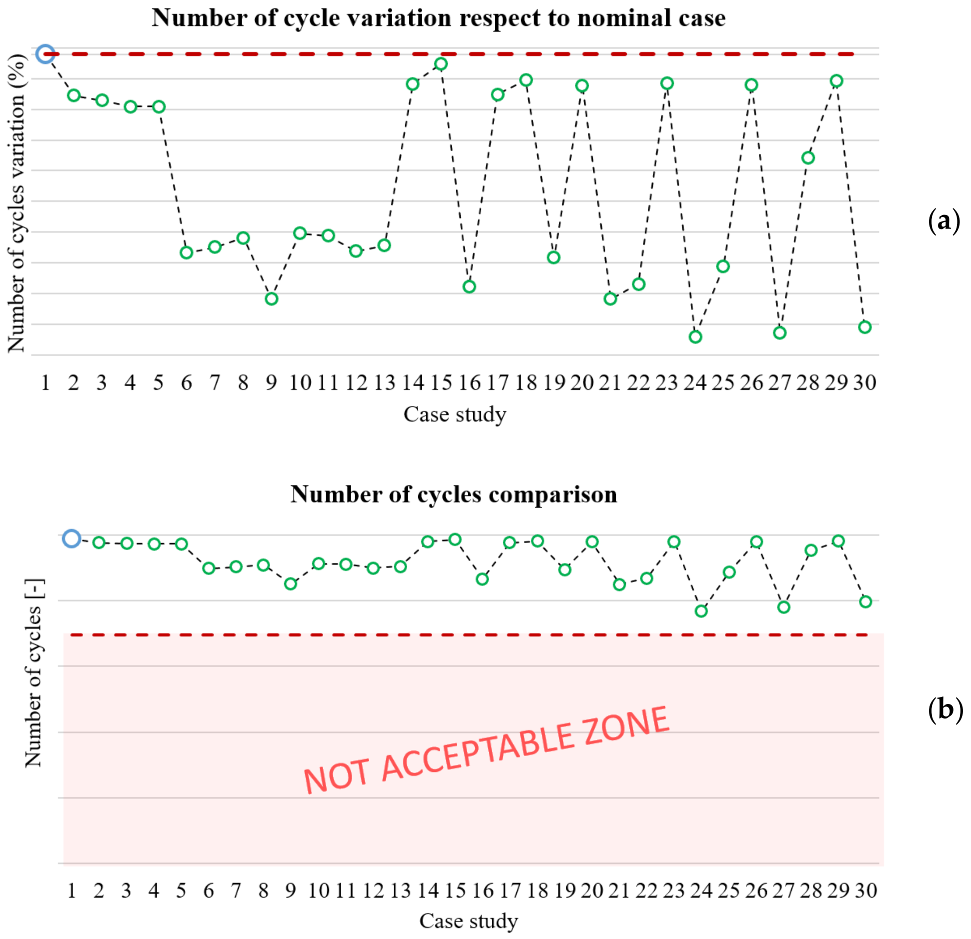

Figure 11.8. LCF estimations of the disc groove. (**a**) comparison of number of cycles percentage variations respect to nominal results; (**b**) comparison of number of cycles for each case.

Figure 11.8 shows that each geometry modification leads to a loss in number of cycles. The most impactful cases are the one with out-of-tolerance values.

Among these last ones, case number 6 (α_2 *max*) has the lowest impact in terms of life reduction.

In nominal geometry, the critical region was the third groove (see **Figure 10.4b**).

Other relevant reductions are recorded in cases number 19 (L_1 *toll up*), 22 (L_2 *toll up*) and 25 ($L_{1,2}$ *toll up*). The first case involves a downward translation of second active plane which causes an overloading on the grooves 1 and 3. The critical region remains on the third groove and number of cycles are reduced respect to nominal geometry. The second one considers a downward translation of the third active plane, causing an increase of load on grooves 1 and 2 and the critical region moves to the second groove. The last one considers both these modifications. Critical region moves to the first groove because now it withstands a part of the load that previously belonged to grooves 2 and 3.

12. Conclusions

Considering all the above results, some conclusions can be drawn and discussed.

The statistical approach applied to the CTQ (Critical to Quality) measurements from the machining process permits to better represent out-of-tolerances. In detail, this approach provides us a more accurate method to quantify and evaluate the magnitude of the out-of-tolerances. Also, the trend of the process can be better investigated and a final decision about which out-of-tolerance values deserve a more in-depth assessment. Hence, the statistical approach, applied to the studied geometry and to the first available CTQ data from the new second source supplier, allowed us to make a reliable selection on the most representative out-of-tolerance parameters and their magnitude.

The second step of this work has been the mesh refinement process and the FE model setting. This phase was essential to achieve precise and reliable results on nominal geometry. All stresses, contact pressures and LCF results can be considered as mesh independent. At the end of this process the final FE model settings were selected. Then, the same settings, applied to all out-of-tolerance cases, permitted to obtain comparable results without any mesh-related or contact behaviour uncertainties.

The results obtained from the out-of-tolerance analyses are consistent with the applied modifications to the nominal geometry and the impact on the lifing of the blade fir-tree attachment has been estimated.

It was found a significant fatigue life reduction, especially in out-of-tolerance cases. Furthermore, there are some case studies at tolerance limits which also recorded a non-negligible lifing reduction. The counter clockwise rotation of the active plane of the first lobe, i.e. lower tolerance limit of angle α_1, improves fatigue life on the blade root because it relieves the most stressed point.

In all cases, there is a sufficiently large margin from the minimum number of cycles required from the product specification.

Anyway, before lifing limit, the blade is disassembled, refurbished and reconditioned. So, a possible indications or damages can be detected and evaluated.

All these results have been obtained on an existing geometry for a component with a well-proven life duration. So, the contents of this work are useful for a comparison between calculation results and field returns. Surely, all other parameters need to be investigated by means of dedicated analyses: out-of-tolerance along the lobe axially for example (planarity of the active planes).

Furthermore, also in case of a new blade design, these comparisons could be considered and applied to define a new tolerance range for fir-tree attachment during the machining process.

Another achieved goal of this work is the setting of an easy-to-implement procedure that can be futuristically applied to other similar components and geometries. As a consequence, a possible insight should be to apply the same approach to other similar fir-tree attachments and compare results to evaluate the lifing impact of these out-of-tolerances as function of turbine stages (centrifugal loads, materials and temperatures influence).

Considering all the above comments and possible insights, future goals could be a critical review of the out-of-tolerance ranges, modifications of the component maintenance plans, establish an empirical formula as function of the out-of-tolerance magnitude for the component lifing and the impact of an out-of-tolerance component on rotor groove in anticipation of next LTE (Life-Time Extension).

Appendix

A. Neuber's rule

As long as the material has linear elastic behaviour, notch effects can be estimated using an only one coefficient named stress concentration factor k_t such that [44]:

$$\begin{cases} \sigma_{max} = k_t \sigma_{nom} \\ \varepsilon_{max} = k_t \varepsilon_{nom} \end{cases} \tag{A.1}$$

When the yield point is exceeded it is not so easy to evaluate the notch effects because of non-linearities. Typically, FE analysis are used for this aim but there are also approximated approaches. Among these last ones there is *Neuber's rule*, that is suitable for plane stress state. In notch areas, plasticity tends to soften the maximum stress and to concentrate strain. Hence, it is necessary to introduce two different factors, the stress concentration factor k_σ and the strain concentration factor k_ε [44]:

$$k_\sigma = \frac{\sigma_{max}}{\sigma_{nom}}; \qquad k_\varepsilon = \frac{\varepsilon_{max}}{\varepsilon_{nom}} \tag{A.2}$$

According to Neuber, the geometry mean of these two factors is equal to k_t [44]:

$$k_t^2 = k_\sigma k_\varepsilon \tag{A.3}$$

Neuber assumed that the elastic energy related to $\sigma_{max,el}$ and $\varepsilon_{max,el}$ was equal to the elastic-plastic one related to σ_{max} and ε_{max}. **Figure A.1** shows graphically these energies on the $\sigma - \varepsilon$ plane.

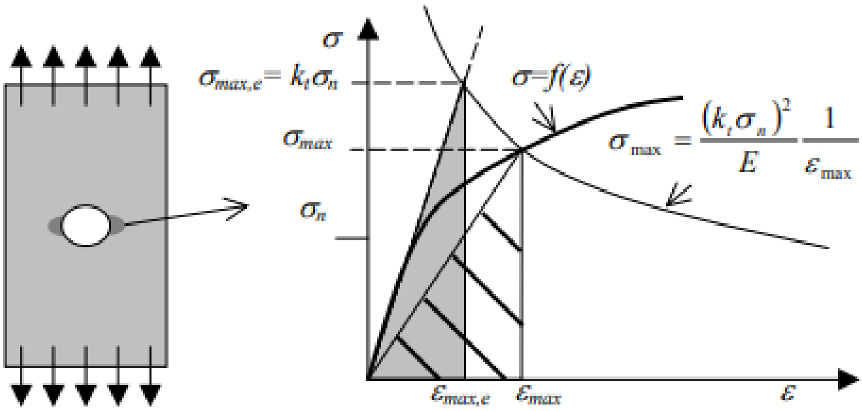

Figure A.1. On the left, a sample with a notch; on the right, the representation of the elastic (grey triangle) and elastic-plastic (dashed triangle) energies.

The area of the two triangles, i.e. the energy, can be evaluated as follow [44]:

$$dU_{elastic} = \frac{1}{2}\sigma_{max,el}\varepsilon_{max,el}dV = \frac{1}{2}k_t\sigma_n k_t\varepsilon_n dV \tag{A.4}$$

$$dU_{elastic-plastic} = \frac{1}{2}\sigma_{max}\varepsilon_{max}dV = \frac{1}{2}k_\sigma\sigma_n k_\varepsilon\varepsilon_n dV \tag{A.5}$$

Equializing eq. A.4 and A.5 we obtain [44]:

$$\sigma_{max}\varepsilon_{max} = \sigma_{max,el}\varepsilon_{max,el} = k_t^2\sigma_n\varepsilon_n \tag{A.6}$$

It is known that for increasing loads $k_\sigma \rightarrow 1$ so, from eq. A.3 it results that for increasing loads $k_\varepsilon \rightarrow k_t^2$ [44].

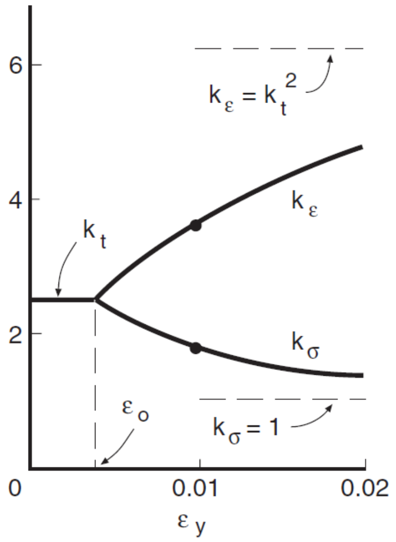

Figure A.2. k_σ and k_ε trend respect to notch strain [31].

If the equation of the plastic curve $\sigma_{max} = f(\varepsilon_{max})$ is known, it can be written a system of equations [44]:

$$\begin{cases} \sigma_{max}\varepsilon_{max} = k_t^2\sigma_n\varepsilon_n = \dfrac{(k_t\sigma_n)^2}{E} \\ \sigma_{max} = f(\varepsilon_{max}) \end{cases} \tag{A.7}$$

For a given notch and a given nominal stress, k_t and σ_n are known. Hence, on the $\sigma - \varepsilon$ plane the Neuber's rule can be translated into a hyperbola of equation [44]:

$$\sigma_{max} = \frac{(k_t\sigma_n)^2}{E}\frac{1}{\varepsilon_{max}} \tag{A.8}$$

B. Ramberg-Osgood model

It is a simplified model that introduces material's plasticity. This model considers the total strain composed of two separate components, the elastic and the plastic ones. The elastic strain component is related to the stress by the young modulus, while the plastic one is related to the stress by an exponential equation [31]. In formula:

$$\varepsilon_t = \varepsilon_e + \varepsilon_p = \frac{\sigma}{E} + \left(\frac{\sigma}{H}\right)^{\frac{1}{n}} \tag{B.1}$$

where n is called *strain hardening exponent* and H is called *resistance coefficient* [31].

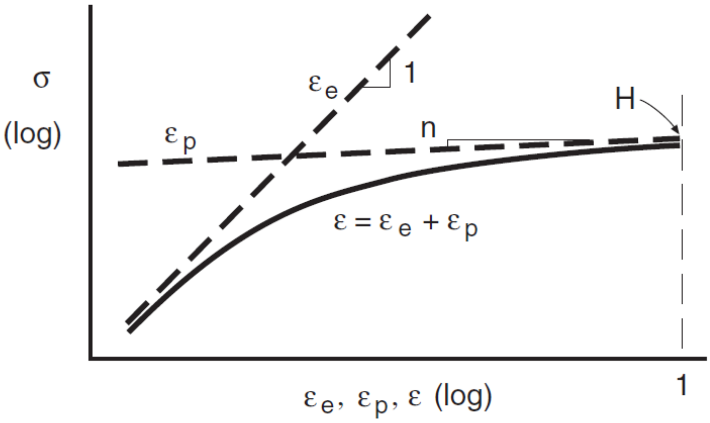

Figure B.1. Ramberg-Osgood curve [31].

As shown in **Figure B.1**, the plastic strains can be represented by a line with angular coefficient equal to n (in log-log scale), while the elastic ones can be represented by the bisector of the first quadrant. In the diagram it can be observed that when $\sigma = H$ then $\varepsilon = 1$. The two lines intersect themselves in the yield point, i.e. $\sigma = \sigma_y$ [31].

C. Strain-based approaches to fatigue life

C.1. Material's cyclic curve

Materials behaviour can be seen through experimental tests with imposed constant strain amplitude ε_a. The maximum strain is $\varepsilon_{max} = +\varepsilon_a$, the minimum strain is $\varepsilon_{min} = -\varepsilon_a$, hence strain range is $\Delta\varepsilon = 2\varepsilon_a$. Hardening occurs when it is necessary to increase the stress to achieve the limit strain at each cycle whereas softening occurs when the stress to reach the limit strain decreases at each cycle [31].

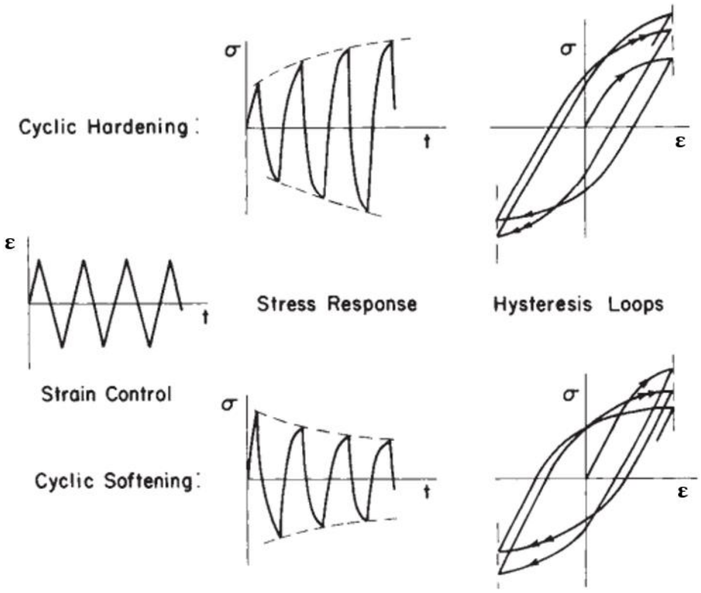
Cyclic Hardening:
σ
t
σ
ε
ε
t
Stress Response
Hysteresis Loops
Strain Control
σ
Cyclic Softening:
t
σ
ε

Figure C.1. Cyclic hardening and softening [39].

In this way we obtain a hysteresis loop on $\sigma - \varepsilon$ diagram. The so-called *cyclic curve* of a material is the curve that passes through the apexes of the different stabilized hysteresis loops [31].

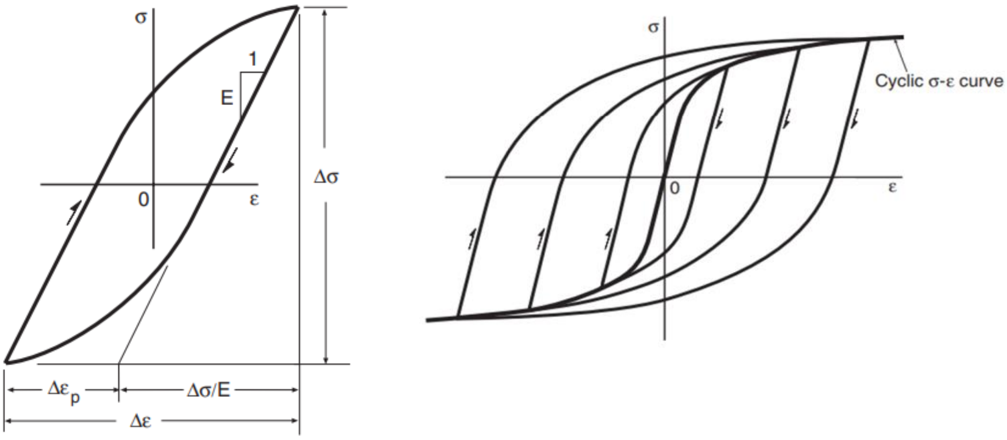

(**a**) (**b**)

Figure C.2. (**a**) stabilized hysteresis loop; (**b**) cyclic stress-strain curve [31].

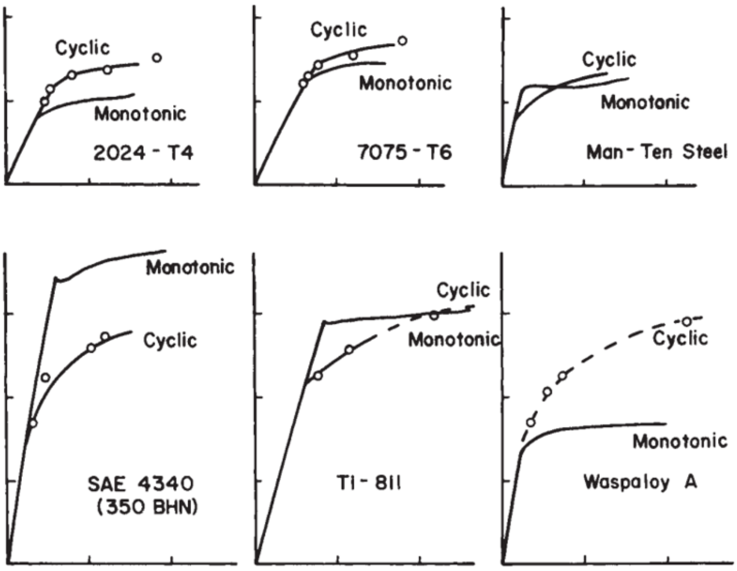

Figure C.3. Example of monotonic and cyclic curves for different metals and alloys [31].

C.2. Coffin-Manson equation

For the evaluation of LCF, total strain amplitude is divided into its two components, elastic and plastic strain:

$$\varepsilon_{at} = \varepsilon_{ae} + \varepsilon_{ap} \tag{C.1}$$

where $\varepsilon_{ae} = \sigma_a/E$ is the elastic strain, ε_{ap} is the plastic strain [31].

Thanks to the cyclic curve, it is possible to write a linear relation – in the log-log scale – between elastic and plastic strain and the number of cycles:

$$\begin{gathered}\varepsilon_{ae} = \frac{\sigma_a}{E} = \frac{\sigma_f'}{E}\left(2N_f\right)^b \\ \varepsilon_{ap} = \varepsilon_f'\left(2N_f\right)^c\end{gathered} \tag{C.2}$$

hence, the total strain amplitude is:

$$\varepsilon_{at} = \varepsilon_{ae} + \varepsilon_{ap} = \frac{\sigma_f'}{E}\left(2N_f\right)^b + \varepsilon_f'\left(2N_f\right)^c \tag{C.3}$$

This is the equation of the *Coffin-Manson curve* [31].

C.3. Morrow approach to mean stress – mathematical steps

As previously written in subsection 2.3.2.1, Morrow started from eq. 2.2 and made it suitable for $\varepsilon - \mathrm{N}$ curves.

In the log-log scale $\mathrm{S} - \mathrm{N}$ curve, the straight-line equation can be written as:

$$\sigma_{ar} = \sigma_f'\left(2N_f\right)^b \tag{C.4}$$

therefore:

$$\sigma_a = \left(\sigma_f' - \sigma_m\right)\left(2N_f\right)^b \tag{C.5}$$

It is introduced the *Morrow parameter* $\left(1 - \frac{\sigma_m}{\sigma_f'}\right)^{\frac{1}{b}}$, so that it can be written:

$$\sigma_a = \sigma_f'\left[\left(1 - \frac{\sigma_m}{\sigma_f'}\right)^{\frac{1}{b}}\left(2N_f\right)\right]^b \tag{C.6}$$

and, by comparing eq. C.4 and C.5:

$$N^* = N_f\left(1 - \frac{\sigma_m}{\sigma_f'}\right)^{\frac{1}{b}} \tag{C.7}$$

where N^* is the fatigue life evaluated when the mean stress is equal to zero. Then, by substituting N^* in eq. C.3 we obtain:

$$\varepsilon_{at} = \frac{\sigma_f'}{E}(2N^*)^b + \varepsilon_f'(2N^*)^c \tag{C.8}$$

and finally, the effective fatigue life can be assessed as:

$$N_f = \frac{N^*}{\left(1 - \frac{\sigma_m}{\sigma_f'}\right)^{\frac{1}{b}}} \tag{C.9}$$

The Coffin-Manson curve equation can also be rewritten as [31]:

$$\varepsilon_{at} = \frac{\sigma_f'}{E}\left(1 - \frac{\sigma_m}{\sigma_f'}\right)\left(2N_f\right)^b + \varepsilon_f'\left(1 - \frac{\sigma_m}{\sigma_f'}\right)^{\frac{c}{b}}\left(2N_f\right)^c \tag{C.10}$$

D. Shot peening

Shot peening is a cold working process that consists of bombarding a surface with little spherical metal bodies at high velocity. The bombardment deforms locally and permanently the surface, inducing residual compression stresses at and under the surface. When the compressed zone reaches a satisfactory thickness below the surface, the process ends [45].

The process increases the component's resistance to fatigue failure, corrosion fatigue and fretting fatigue. Furthermore, this process also adds to the treated component the benefits of the cold working processes, i.e. material's hardening, better intergranular corrosion resistance, closing of porosity [45].

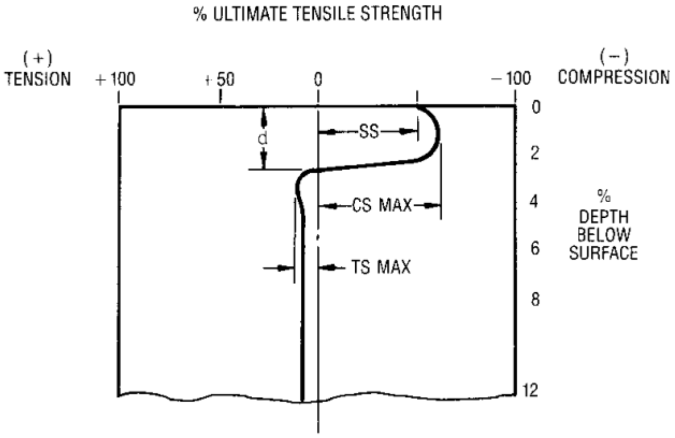

Figure D.1. Typical residual stress profile obtained with shot peening [45].

As shown in **Figure D.1** the maximum compression stress obtained (*CS MAX*) exceed the half of the material's ultimate tensile stress. *SS* is the compression stress that can be measured at the surface after the process, while *TS MAX* is the maximum tensile stress. This last one generates to guarantee the component's internal equilibrium, and have to be kept below a certain in order to avoid the component's failure. The thickness of the compressed zone is called *d* [45].

Machining processes, such as grinding (see section 1.7.1) or EDM (see section 1.7.2), are detrimental to fatigue properties because generates residual tensile stresses at the surface, enhancing the sensitivity to notches and the probability of crack initiation. Nevertheless, as explained in the preceding chapters, machining processes are essential to achieve the required precision by the design tolerances. Hence, shot peening has to be performed also to recover the machining processes disadvantages [45].

Figure D.2 reports experimental data relative to fretting fatigue of a peened specimen (triangles) and a unpeened specimen (black circles). It can be clearly observed that under the same stress, the first one can withstand a much greater number of cycles.

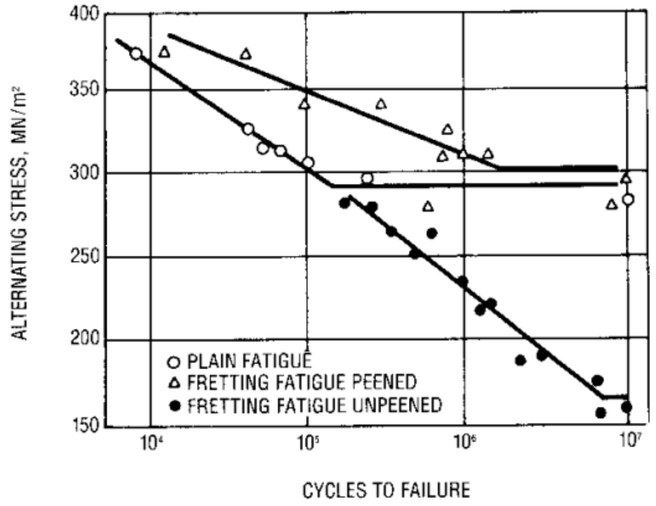

Figure D.2. Effect of shot peening on fretting [45].

Shot peening enhance component's fatigue resistance by arresting crack propagation, in fact, under compressive stress a crack doesn't propagates. When an external load is applied, the residual compression has to be balanced before a tensile stress is generated in the component and its peak value is also reduced (see **Figure D.3**) [45].

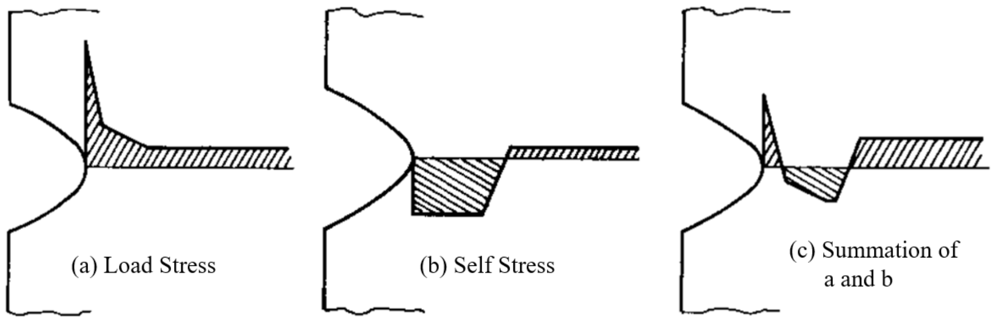

Figure D.3. (**a**) stress profile generated by the external load; (**b**) stress profile generated by shot peening; (**c**) the effective stress profile is the combination of the two [45].

Resistance to corrosion fatigue is another property which shot peening successfully improves. The combination of harsh environments and high stresses can lead to failure due to corrosion fatigue. Shot peening retards this type of failure. Benefits are shown in **Figure D.4** [45].

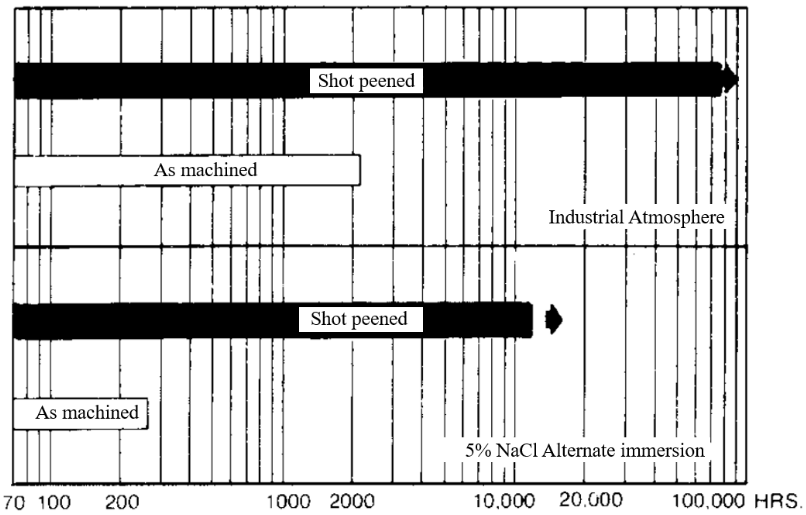

Figure D.4. Comparison of corrosion fatigue resistance of a peened and of an unpeened specimen operating in industrial atmosphere (top) and in a 5% NaCl solution (bottom) [45].

Gas-turbine blades are a typical component on which shot peening is performed. Usually it is performed on the attachment to increase its fatigue life and to recover detrimental effects of machining processes, but it can be also performed on the airfoil to improve its general fatigue properties [45].

E. Case studies results comparisons

Table E.1. Radial stress comparison.

Case study	Max normalized radial stress on blade root [-]	Min normalized radial stress on blade root [-]	Max normalized radial stress on disc groove [-]	Min normalized radial stress on disc groove [-]
1	0,693	-2,189	0,886	-1,753
2	0,659	-2,376	0,942	-1,521
3	0,671	-2,225	0,942	-1,521
4	0,714	-2,250	0,949	-1,756
5	0,711	-2,252	0,951	-1,755
6	0,757	-2,754	0,968	-2,139
7	0,706	-2,038	0,961	-1,755
8	0,704	-2,558	0,956	-1,776
9	0,741	-3,077	1,005	-2,241
10	0,682	-2,428	0,957	-1,914
11	0,682	-2,289	0,961	-1,531
12	0,673	-2,410	0,962	-1,906
13	0,682	-2,593	0,962	-1,783
14	0,727	-2,093	0,921	-1,761
15	0,723	-2,618	0,922	-1,787
16	0,825	-3,250	0,985	-2,261
17	0,695	-2,459	0,928	-1,918
18	0,693	-2,652	0,932	-1,786
19	0,760	-2,392	0,971	-1,767
20	0,702	-2,095	0,931	-1,757
21	0,867	-2,694	0,997	-1,735
22	0,729	-2,102	0,993	-1,767
23	0,675	-2,328	0,932	-1,751
24	0,831	-2,358	1,096	-0,978
25	0,798	-2,267	0,973	-1,757
26	0,686	-2,230	0,932	-1,751
27	1,021	-2,790	1,062	-1,657
28	0,768	-2,634	0,947	-1,900
29	0,691	-2,642	0,931	-1,803
30	0,980	-2,891	1,045	-2,220

Table E.2. von Mises stress comparison.

Case study	Max normalized von Mises stress on blade root [-]	Max normalized von Mises stress on disc groove [-]
1	1,341	0,927
2	1,450	0,926
3	1,075	0,926
4	1,387	0,931
5	1,386	0,929
6	1,475	0,949
7	1,370	0,892
8	1,367	0,926
9	1,583	0,933
10	1,493	0,936
11	1,119	0,936
12	1,479	0,897
13	1,256	0,936
14	1,418	0,891
15	1,410	0,938
16	1,700	0,941
17	1,521	0,886
18	1,287	0,951
19	1,487	0,956
20	1,273	0,917
21	1,704	0,992
22	1,427	0,910
23	1,302	0,911
24	1,649	0,978
25	1,568	0,902
26	1,231	0,911
27	2,028	0,941
28	1,672	0,882
29	1,281	0,935
30	1,936	0,931

Table E.3. Contact pressure comparison.

Case study	Lobe 1 max pressure [-]	Lobe 2 max pressure [-]	Lobe 3 max pressure [-]
1	1,874	1,353	1,779
2	2,174	1,384	1,804
3	1,573	1,397	1,810
4	1,927	1,637	1,830
5	1,926	1,644	1,831
6	2,037	2,416	1,927
7	1,908	1,408	1,466
8	1,902	1,403	2,085
9	2,009	1,549	2,701
10	2,227	1,677	1,853
11	1,604	1,683	1,861
12	2,209	1,438	1,484
13	1,592	1,445	2,112
14	1,969	1,685	1,504
15	1,960	1,687	2,133
16	2,204	2,627	2,864
17	2,261	1,724	1,522
18	1,622	1,726	2,160
19	2,051	1,044	1,942
20	1,793	1,483	1,700
21	2,309	0,371	2,191
22	1,979	1,508	1,514
23	1,829	1,277	1,891
24	2,235	1,896	0,000
25	2,144	1,227	1,694
26	1,745	1,407	1,812
27	2,672	1,268	1,907
28	2,436	1,615	1,480
29	1,620	1,730	2,154
30	2,569	2,487	2,526

Bibliography

[1] Alinejad F., Botto D., "Innovative design of attachment for turbine blade rotating at high speed", in *Proceedings of ASME Turbo Expo 2017: Turbomachinery Technical Conference and Exposition GT2017*, 2017

[2] Moneta G., Jachimowicz J., "Impact of manufactory tolerances on stress in a turbine blade fir-tree root", in *Fatigue of aircraft structures*, 2020

[3] Xu Y., *Analysis of Barreling and Tolerance Effects of Blade Attachments*, 2018.

[4] Khot A., Bharatish A., Srihari P.V., "Effect of fretting fatigue parameters on fir-tree joint of aero-engine blade disc interface", in *International Journal of Novel Research and Development*, 2017

[5] Alinejad F., Botto D., Gola M., Bessone A., "Design Space reduction for the optimization of the blade fir-tree attachment", in *Proceedings of ASME Turbo Expo 2018*, 2018

[6] Acar E., Gündüz M., "Structural optimization of blade-disc firtree attachment of an aeroengine", in *The 16th International Conference on Machine Design and Production*, 2014

[7] Song W., Keane A.J., "An efficient evolutionary optimisation framework applied to turbine blade firtree root local profiles", in *Structural and Multidisciplinary Optimization*, Vol. 29, n. 5, pp. 382-390, 2004

[8] Rao J.S., Kumar B., "3D blade root shape optimization", in *10th International Conference on Vibrations in Rotating Machinery*, 2012

[9] Alinejad F., Botto D., "Innovative adaptive penalty in surrogate-assisted robust optimization of blade attachments", in *Acta Mech*, Vol. 230, n. 4, pp. 2735-2750, 2019

[10] Botto D., Lavella M., "Fretting Fatigue Analysis of Additively Manufacture Blade Root Made of Intermetallic Ti-48Al-2Cr-2Nb Alloy at High Temperature", in *Materials*, Vol. 11, n. 7, p. 1052, 2018

[11] Soares C. M., *Gas Turbines in simple cycle and combined cycle applications*, 1 ed., Butterworth Heinemann, US DOE, Office of Fossil Energy, 2006

[12] Ansaldo Energia SpA, *GT36 – The superior value*. URL: https://www.ansaldoenergia.com/fileadmin/_processed_/3/f/csm_GT36_render_9bffcbccfa.png

[13] Marsilio R., "Appunti del corso di Fondamenti di macchine e propulsione", Corso di Laurea in Ingegneria Aerospaziale, Politecnico di Torino

[14] Wikipedia, *Bryton Cycle*. URL: https://en.wikipedia.org/wiki/Brayton_cycle

[15] Orenes Moreno B., *Linear Elastic Fracture Mechanics Assessment of a gas turbine vane*, 2022

[16] Ansaldo Energia training materials

[17] Ferlauto M., "Appunti del corso di Fluidodinamica delle turbomacchine", Laurea Magistrale in Ingegneria Aerospaziale, Politecnico di Torino, 2023

[18] Can Gülen S., *Gas Turbines for Electric Power Generation*, 1 ed., New York, Cambridge University Press, 2019

[19] Han J.C., Dutta S., Ekkad S., *Gas Turbine heat transfer and cooling technology*, 2 ed., New York, CRC Press, 2012

[20] Barwinska I., Kopec M., Kukla D., Senderowsky C., Kowalewsky Z.L., "Thermal Berrier Coatings for High-Temperature Performance of Nickel-Based Superalloys: A Synthetic Review", in *Coatings*, Vol. 13, n. 4, pp. 769-790, 2023

[21] Chen W.R., Wu X., Marple B.R., Nagy D.R., Patnaik P.C., "TGO growth behavior in TBCs with APS and HVOF bond coats", in *Surface and Coatings Technology*, Vol. 202, n. 12, pp. 2677-2683, 2008

[22] Sankar V., "Thermal Barrier Coatings Material Selection, Method of Preparation and Applications – Review", in *International Journal of Mechanical Engineering and Robotics Research*, Vol. 3, n. 2, 2014

[23] The Open University, *Creep feed grinding*. URL: https://www.open.edu/openlearn/science-maths-technology/engineering-technology/manupedia/creep-feed-grinding

[24] ELE Advanced Technology Ltd., *Creep feed grinding*. URL: https://eleat.co.uk/technology/creep-feed-grinding/

[25] S.K. Saha, *Experimental Investigation of the Dry Electric Discharge Machining (Dry EDM) Process*, 2008

[26] Mahajan R., Krishna H., Singh A.K., Ghadai R.K., "A Review on Copper and its alloys used as electrode in EDM", in *IOP Conference Series: Materials Science and Engineering*, 2018

[27] Beijing Dimon CNC Technology Co., Ltd., *Application of EDM Forming Machine in Mold And Die Industry*. URL: https://www.dmncedm.com/automatic-cnc-machine-for-mold-and-die.html

[28] Suresh S., *Fatigue of Materials*, 2 ed., New York, Cambridge University Press, 1998

[29] Schüt W., "A History of fatigue", *Engineering Fracture Mechanics*, Vol. 54, n. 2, pp. 263-300, 1996

[30] Fatemi A., Shamsaei N., "Multiaxial fatigue: An overview and some approximation models for life estimation", in *International Journal of Fatigue*, Vol. 33, n. 8, pp. 948-958, 2011.

[31] Vergani L., *Meccanica dei materiali*, 1 ed., Milano, McGraw-Hill, 2001

[32] NPTEL, *General Introduction – Continuum Damage Mechanics (CDM)*. URL: https://nptel.ac.in/courses/105108072

[33] Chaboche J.L., "Continuum damage mechanics: Present state and future trends", in *Nuclear Engineering and Design*, Vol. 105, n. 1, pp. 19-33, 1987

[34] Ambroziak A., Kłosowsky P., "Survey of modern trends in analysis of continuum damage mechanics", in *Task Quarterly*, Vol. 10, n. 4, pp. 437-454, 2006

[35] European Aviation Safety Agency, *Certification Specifications and Acceptable Means of Compliance for Large Aeroplanes CS-25*, Amendment 28, 2023.

[36] Reddick Jr H.K., "Safe-life and damage-tolerant design approaches for helicopter structures", in *Langley Research Center Failure Anal. and Mech. of Failure of Fibrous Composite Struct., NASA*, 1983

[37] Botto D., Firrone C.M., "Appunti del corso di Costruzione di motori per aeromobili", Laurea Magistrale in Ingegneria Aerospaziale, Politecnico di Torino, 2023

[38] Madhukar S., Reddy B.R.H., Kumar G.A., Naik R.P., "Study on Improvement of Fatigue Life of materials by Surface Coatings", in *International Journal of Current Engineering and Technology*, Vol. 8, n. 1, 2018

[39] Landgraf R.W., "The resistance of metals to cyclic deformation", in *Achievement of high fatigue resistance in metals and alloys, ASTM International*, Vol. 467, pp. 3-36, 1970

[40] Dowling N.E., *Mechanical Behavior of Materials, Methods for Deformation, Fracture, and Fatigue*, 4 ed., Boston, Pearson Education, 2013

[41] Zhu S., Ye W., Correia J.A.F.O., Jesus A.M.P., Wang Q., "Stress gradient effect in metal fatigue: Review and solutions", *Theoretical and Applied Fracture Mechanics*, 2022

[42] Mei J., Xing S., Vasu A., Chung J., Desai R., Dong P., "The fatigue limit prediction of notched components – A critical review and modified stress gradient based approach", *International Journal of Fatigue*, 2020

[43] Ansys® Mechanical APDL, Release 18.2, help system, Element Library, ANSYS, Inc.

[44] Manfredi E., "Dispense di Elementi costruttivi delle macchine", corso di Laurea in Ingegneria Meccanica, Università degli Studi di Pisa, 2003

[45] Champaigne J., "Shot peening overview", *Metal Improvement Company*, 2001